I. ION-SOLID INTERACTIONS WITH MARKERS
II. OXIDATION PHENOMENA IN SILICIDES AND ALUMINIDES

Thesis by

Sung Joon Kim

In Partial Fulfillment of the Requirements

for the Degree of

Doctor of Philosophy

California Institute of Technology

Pasadena, California

1988

(Submitted May 2, 1988)

Acknowledgements

I would like to express my sincere gratitude to my thesis advisor Prof. Marc-Aurele Nicolet for making my stay in his research group an unforgettable experience. His invaluable guidance and incessant advice since my undergraduate years as a sophomore is truly appreciated. I would also like to thank Prof. Robert S. Averback of the University of Illinois at Urbana for giving me insight into the field of ion-solid interactions. I am truly privileged to have known him.

I am grateful to Dr. Tom C. Banwell for many interesting and helpful discussions. I also wish to thank Drs. Bruce Paine, Rindge Shima, David Jamieson, Meir Bartur, Yang-Tze Cheng, and Xin-An Zhao for their interest and collaborations.

Part of the work reported here was carried out using the facilities at Argonne National Laboratories (ANL). I am grateful to all the members of ANL who have helped me to perform successfully all the experiments. I would like to especially acknowledge Messrs. Peter Baldo, Loren J. Thompson, and Jack Wallace for keeping the "G-wing accelerator" happy and alive and also for putting up with me during my visit to ANL.

Special thanks go to Messrs. Rob Gorris, Ali Ghaffari, and David Groseth for their superb technical assistance and patience in dealing with me. I am extremely grateful to Mses. Michell Parks, Rosie Pieters-Emerick and Arlene Collinwood for their outstanding secretarial work and friendship.

Many thanks go to Drs. Frank So, Elzbieta Kolawa, Kenneth Kung, Marc Thuillard, Andreas J. Brunner, Simon Nieh, and Jyrki Molarius for their inspirations and encouragements. I am indebted to fellow students En Ma, Gang Bai, Eric Pan, Tom Workman, Liem Tran, and Bill Flick for their generous help in times of need and creating a stimulating and pleasant research environment.

I am indebted to the Office of Naval Research and the International Business Machines Corporation for their financial assistances.

Finally, I wish to express my deepest respect and gratitude to my parents. Without their unfailing support, encouragements, and sacrifice, I would not be where I am today. It is to them that I dedicate this thesis.

Preface

This thesis consists of two main topics: a) study of ion-solid interactions, or "ion mixing", by markers and b) oxidation phenomena of metal silicides and gold aluminides.

There are many well-developed theories describing atomic collisions in solids. However, the basic aspects of ion mixing, such as the magnitude of atomic relocation and the formation of certain compounds, have proven elusive to theoretical understanding. We have conducted experiments that provide a data base for an understanding of atomic motion during ion irradiation. In these experiments the so-called "marker" sample configuration was used, where a layer of about 10 Å of an impurity is buried in an otherwise homogeneous medium. When the sample is irradiated, the layer is dispersed. This irradiation-induced spreading of marker layer is measured by backscattering spectrometry. The different amount of spreading in different samples under various experimental conditions yields insight into the atomic displacement mechanisms.

Three major mechanisms are known to contribute to the atomic displacements during ion irradiation on solids: a) collisional displacements, b) intermixing by a thermal spike and c) radiation-enhanced diffusion (see chap. 1 for definitions). At low temperatures only the first two mechanisms play role in the atomic displacements; at high temperatures radiation-enhanced diffusion is significant. The irradiations were conducted at temperatures ranging from 7 to 500 K using Kr and Xe ions of energies from 0.3 to 1.0 MeV. The matrix atoms studied range in mass from C to Au. The marker impurities used go from Al to Bi.

At low temperatures, the effects of material properties and parameters such as

mass and cohesive energy of the target, damage energy density in the material, thermal diffusivity, and heat of mixing are investigated. At high temperatures, the effects of the defect creation rate in the material by irradiation and the diffusion mechanisms are studied.

The second part of the thesis deals with oxidation phenomena. The oxidation of Co and Ni disilicides on SiO_2 substrates is investigated. The motivation of this work is the desire to produce an elemental metal film encapsuled by a protective insulating SiO_2 layer for low resistivity interconnection in VLSI circuits. Electrical, chemical, and morphological properties of the oxidized films were investigated as a function of oxidation duration under various oxidation conditions and Si content in the silicide films.

The oxidation of Au aluminides was also investigated. Gold bonds on aluminum metallization for semiconductor devices are under constant physical and chemical changes due to joule heating, electromigration and outgassing of packaging materials. Water and oxygen are some of the main undesirable components in the outgassing of packaging material. We investigate the effects of 50, 70, and 100° C water and wet oxidation at 773 K on thin films of Al and of all five existing binary Au-Al compounds ($AuAl_2$, AuAl, Au_2Al, Au_5Al_2, and Au_4Al) on SiO_2 substrates.

Most of the work presented in this thesis is published or accepted for publication. The publication list is included at the end of the thesis. Details not described in this thesis are found in the published work.

Contents

List of Tables

List of Figures

Chapter 1

ION MIXING

1.1 Introduction

Irradiation of solids with energetic ions modifies the material in several ways: a) atoms in the material are displaced due to collisions with each other and with irradiated ions; b) atoms on the surface layer of the material are sputtered off; and c) the properties of the target material are changed due to other atomic relocations and to implanted ions. Over the past years all these three interrelated phenomena have attracted a great amount of research interest in both the scientific and industrial community. The first part of this thesis mainly concerns the first of the items mentioned above or, specifically, a branch of the ion-solid interaction field that is commonly known as "Ion Mixing" or "Ion Beam Mixing". Ion Mixing can generally be defined as "....all changes in spatial distribution of elemental species brought about by ion irradiation of a solid" [1].

From the above description of ion mixing, the spatial redistribution of elemental species comes mainly from (1) displacements, (2) replacement sequences and (3) migration and recombination of defects within the irradiated region. The consequences of such processes are chiefly the transport of material and the changes in the microstructural order under conditions of non-equilibrium kinetics and thermodynamics. For example, a non-thermal equilibrium concentration of defects created by irradiation can induce point defect clusters, voids, dislocation loops and networks; and the metastable thermodynamic state results in changes in composition, phase distribution, crystal structure and defect microstructure of the irradiated material.

All these effects were of interest in early days because they bear on the design of fission and fusion reactor where the reactors walls are irradiated by energetic particles (i.e., protons, neutrons). In recent years, ion mixing has gained new visibility

as it was recognized that ion mixing is relevant in the processing of thin film devices, and that it can also improve surface properties of materials such as hardness, friction, wear, corrosion, catalysis, adhesion, and reflectance. To fully capitalize on the potentials of ion mixing, it is essential to understand the mechanisms involved in the spatial redistribution of elemental species. We next describe the basic mechanisms of ion mixing that are investigated in this thesis.

1.2 Mechanisms

The recent progress in the understanding of ion mixing mechanisms builds on the fundamental studies of displacement processes in irradiated material that date from early 1950's. The concept of displacement cascades was considered first by Brinkman [2]. Seitz and Koehler [3] were first to look at the thermal spike aspect of cascades, and the concept of radiation-enhanced diffusion was discussed first by Lomer [4]. The basic features of these mechanisms were brought to light from (a) the these early works, as summarized in [5, 6], (b) studies of the binary collisions [7, 8], and (c) molecular dynamics computer simulations [9, 10]. The processes contributing to ion mixing can be characterized either by the typical energies involved or by the time scale of the events [11]. We use both of these viewpoints to describe the processes. The terms we shall use to describe the processes are clarified below. Ion mixing is an evolving field where the meaning of technical terms has not yet converged on to accepted norms. The definitions given here may not always coincide with those of other authors.

a) Linear collisional cascade

When an irradiated ion in the 100 keV range penetrates in solid, the particle slows down by colliding with nuclei of host atoms and by interacting with electrons. Except in dielectric materials, this last process usually generates no atomic

displacements; most displacements of target atoms result from atomic collisions. Initially, an incident high energy ion displaces a small number of target atoms by energetic primary collisions. These recoiling atoms can move far from their initial lattice site, and are displaced in the direction of the incident ion. Each of these primary recoiling atoms in turn makes lower-energy secondary recoils, thus creating subcascades. This process goes on until the recoils have insufficient energy to leave their lattice sites. The typical displacement threshold energy, E_d, for elastic collisions of individual atoms in the solid is between 10 to 40 eV [12]. In the process, the primary knock-on atoms' initial kinetic energy is distributed over an extended volume with the creation of a very high density of defects. In this scenario, the binary collision model is used to describe the displacement of atoms that are viewed as moving with respect to surroundings that are all stationary. This process is commonly referred to as a linear cascade. Molecular dynamics calculations show that when the binary collision process remains dominant, most of the defects created during the initial high-energy part of a collisional cascade spontaneously recombine and the second part of the cascade sets in after 10^{-12} sec. From molecular dynamics simulation and experiments, most atomic displacements during the collisional cascade are produced during the final low-energy part of the cascade. By end of this stage, the average kinetic and potential energies per atom are roughly equal.

b) Thermal spike

It is also possible that as the recoiling atom's energy falls below a few hundred eV's, the approximation of binary collisions in a stationary medium begins to break down and many neighboring atoms are set in motion. This leads to the phenomenon referred to as a thermal spike. This phenomenon, when it occurs, terminates the collisional phase. The reactions in this phase are characterized by energies per atom on the order of 1 eV and a duration of 10^{-12} to 10^{-11} seconds. Its detailed representation is a matter of conjecture. One view represents it as a core of initially highly excited

atoms whose energy is equipartitioned and subsequently dissipates by thermal conduction into an expanding volume as it cools. This is the "thermal spike" model. Another description still retains the idea of a crystalline lattice and assumes that after the average kinetic energy of the atoms falls below a few eV, no further point defects are created. Strain and disorder are very large due to the high concentration of defects, and much energy of the recoils is contained in lattice vibrations. The high agitation of the lattice stimulates the migration of point defects and the diffusion of atomic species in the solid. This process goes on until most of the point defects that contribute to diffusion have recombined. Computer models are the most promising approach with which to clarify these details of a spike and its evolution. Experimental techniques with the required resolution in time and space do not exist at this time.

c) Prompt processes; cascade

To investigate linear cascades and thermal spike phenomena, the experiments must be carried out at temperatures low enough to avoid the thermally aided diffusion of atoms at the specimen's temperature. The sum of all phenomena that occur in time and space during the linear cascade and the spike regimes shall be called here the "prompt processes" and a "cascade". Their functional definition is that these processes are independent of the irradiation temperature.

d) Radiation-enhanced diffusion

The distribution process that takes place as a result of irradiation after the lattice is again equilibrated in the impacted region while a residual excess concentration of point defects still survive will be called here "delayed processes" in a regime called "radiation-enhanced diffusion".

There are basically two parts to radiation-enhanced diffusion. One increases the normal thermal diffusivities locally by increasing the number of defects; the other consists of new kinetic pathways that are absent in equilibrium (e.g., mixed dumbbells and vacancy-solute interstitial pairs, thus inducing diffusion mechanisms other than the

normal thermal diffusion mechanisms for atomic diffusion). These effects are strongly dependent on thermodynamic driving forces, defect mobilities, point defect concentrations, the instantaneous defect structure of the sample (i.e., types and density of defect sinks), the specimen's temperature, and the point defect creation rate during collisional phase. Thermally activated redistribution processes that are effective over the whole volume (the classical case of radiation-enhanced diffusion) of a body are well described by usual chemical rate theory [4, 13].

To investigate radiation-enhanced diffusion, one conducts experiments at elevated temperatures. There is no agreement at this time whether ion mixing in the thermally activated regime results mainly from redistributions within the volume of a cascade and its vicinity, or from rearrangements induced by defect migrating far beyond this volume, or possibly both.

1.3 Types of sample configurations

There are three basic types of sample configurations that are used to study ion mixing: (1) marker or tracer configuration*, where a very thin layer of trace material (typically ~10 to 30 Å) is embedded in a homogeneous matrix; (2) bilayer configuration consisting of two different layers of a few hundred Å of thickness; and (3) multilayer configuration consisting of a multiple sequence of thin (~100 Å) alternating layers of distinct materials.

We have used marker and bilayer configurations to study ion mixing. Thin marker samples are best suited to investigate basic redistribution mechanisms of ion mixing because the configuration is simple. As the marker layer is dispersed by the irradiation, the sample is homogenized, which much simplifies the interpretation. In the bilayer configuration, the supply of both materials to the intermixed region is unconstrained, so that the system can seek its preferred compositions for given

irradiation conditions. The bilayer configuration is useful to study the formation mechanisms of phases by ion mixing and to compare ion mixing with the thermal annealing methods. But the sample changes during the experiment, which can complicate the interpretation.

**The terms marker and tracer have both been used interchangeably in the literature. We also use both words interchangeably here .*

1.4 References

[1] S. Matteson, and M-A. Nicolet, Mat. Res. Soc. Symp. Proc. V.7, Eds. S. Thomas Picraux & W.J. Choyke, (1981) p.3.

[2] J.A. Brinkman, J. Appl. Phys., 25 (1954) 961.

[3] F. Seitz and J. Koehler, Solid State Physics, Vol. 2, Eds. F.Seitz and D. Turnbull (Academic Press, New York, 1956).

[4] W.M. Lomer, AERE Report T/R 1540 (1954)

[5] Radiation Damage in Metals, Eds. N.L. Peterson, and S.D. Harkness, 1976, (American Society of Metals, Metals Park, Ohio).

[6] Properties of Atomic Defects in Metals, Eds. N.L. Peterson, and R.W. Siegel, 1978 (North Holland, Amsterdam); and J. Nucl. Mater., 69-70 1978.

[7] S. Yoshida, J. Phys. Soc. Jap., 16 (1961) 44

[8] J. R. Beeler, Jr., Phys. Rev., 150 (1966) 470.

[9] J.B. Gibson, A.N. Goland, M. Milgram, and G.H. Vineyard, Phys. Rev. 120 (1960) 1229.

[10] W.E. King and R. Benedeck, J. Nucl. Mater. 117 (1983) 26.

[11] P. Sigmund, Appl. Phys. Lett., 25 (1974) 169; and Appl. Phys. Lett., 27 (1975) 52.

[12] H.H. Andersen, Appl. Phys. 18 (1979) 131.

[13] See i.e., R. Sizman in ref. 6, 386.

Chapter 2

COLLISIONAL MIXING; KINEMATICS

2.1 Binary collision theory

There are several ways to calculate the contribution of linear collisional cascade mixing processes to ion mixing. These include analytical transport theory [1,2] and computer simulations [3]. The underlying assumptions in collisional mixing theory are: a) the collisions are governed by two body interactions; b) moving atoms collide only with stationary atoms ("linear" cascade); c) the target is amorphous; and d) the displacement process ends when the atom energies fall below $\approx$ 5 eV. The principal results of this binary collision theory applied to marker experiments are:

1) The spreading of a marker layer has a Gaussian distribution in depth.

2) The variance, σ^2, of the depth distribution increases proportionally to the ion fluence, $\emptyset$, and to the damage energy deposited per ion and per unit depth, F_D (F_D is the energy dE_D per depth dx and per irradiated ion which goes into elastic nuclear collisions. The damage energy E_D excludes the energy deposited in electronic excitations).

3) The magnitude of ion mixing is proportional to the kinematic factor $\gamma_{21}=[4\ m_1m_2/(m_1+m_2)^2]^{1/2}$, where m_1 and m_2 are the masses of the atoms involved in the collision and inversely proportional to the average displacement energy of an atom, E_d.

2.2 Experiments with markers in Ge, Cu, Mo, and Ru matrices.

To investigate the relevance of collisional mixing to ion mixing we have carried out experiments and compared the results with the analytical transport theory of Matteson et al. [2]. This theory of collisional mixing is based on a model of random

flight in which the marker atoms are impacted by a recoiling matrix atom and thereby knocked from their initial sites. The basic equation for this collisional diffusion model is

$$Dt=(1/6)N\langle r^2\rangle, \tag{1}$$

where N is the number of times a marker atom is relocated, and $\langle r^2\rangle$ is the average of the squared relocation distance. Since a whole spectrum of recoil energies is possible, Eq.(1) must be integrated over all possible energies, i.e.,

$$Dt=1/6 \int dE\, dN/dE\, \langle r^2(E)\rangle. \tag{2}$$

Expressions for dN/dE and $\langle r^2(E)\rangle$ based on linear transport theory can be found in ref. 2. The lower limit of integration, E_d, is the minimum energy necessary to displace an atom from its initial site. The upper limit, E_{max}, is the product of kinematic factor, γ_{21}, and the energy of the irradiated ion. Fig. 2.1 illustrates the calculated results for several different markers in Ge. The important feature of the model is that the mixing should increase rapidly with the decreasing atomic number of the marker. A simple test of the theory can therefore be effected by measuring Dt for a heavy and a light marker atom in a given matrix.

To test this particular theory we conducted an experiment with 750 keV Xe beams. A Ge matrix was chosen because both heavy and light markers can be readily analyzed by 1.9 MeV He backscattering spectrometry. The specimens were prepared by vapor deposition onto oxidized Si substrates. The Pt and Si markers had average thicknesses of ~15 Å, and were located at a depth of 400 Å below the Ge surface. The specimen temperature during both the mixing and analyzing irradiations, and the time in

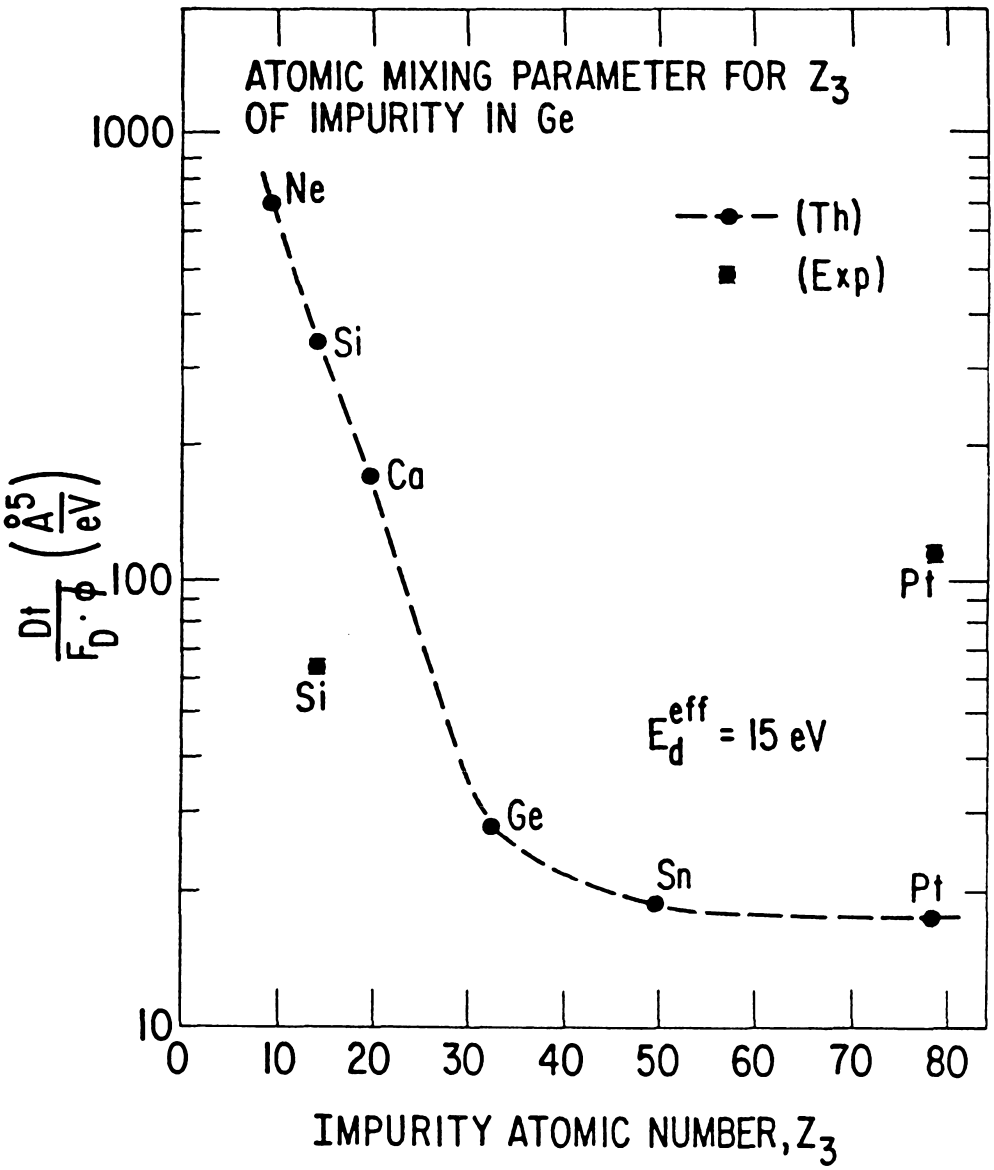

Fig. 2.1. Calculated values for the mixing efficiency in Ge as a function of the atomic number of the marker atom according to Eq. (2). Experimental values for Si and Pt markers are also indicated. Irradiation and analyses were both performed at 6 K.

between, was held near 6 K in order to minimize radiation-enhanced diffusion. The specimens were cooled by clamping them to an aluminum plate which was in contact with a liquid helium bath. Indium strips were placed between the specimens and clamps to prevent the Si wafers from cracking. The beam power was kept below 0.05 W to avoid beam heating; the estimated temperature rise in our specimens was 0.1 K. Dose measurements were performed with a Faraday cage which could monitor the beam flux during irradiation. Its calibration was checked prior to each irradiation by slipping a Faraday cup between it and the specimen. The accuracy is ~ 5%.

We have also tested how the mixing depends on the mass of the marker in Cu, Mo, and Ru matrices with markers of widely ranging mass. For Cu matrix, the samples were irradiated with 750 keV Kr at 77, not 7 K, and analyzed in situ using backscattering of 1.9 MeV He. The samples with Pt or Au markers in Cu were also irradiated at 6 K and analyzed in situ at 7 K. Their ion mixing efficiencies were equal to those found at 77 K within experimental uncertainty. For the Mo and Ru matrices, another set of irradiation and backscattering conditions were employed. The Kr ion energy was 300 keV and the irradiations were performed at 77 K, not at 6 K. These samples were then warmed to room temperature and transferred to a separate system for backscattering analysis with 2 MeV He. To verify that there was insignificant difference from in situ 6 K experimental conditions, samples with a Au marker in Ru and with Ti and Pt markers in Mo were irradiated and measured both ways. For Ru, the two results were within experimental uncertainty; for Mo, ion mixing was about ~50 % higher at 77 K than at 6 K. This difference leaves the conclusion of the experiment unaltered.

All markers had Gaussian backscattering signals before and after irradiation. The increase in the variances of the marker signals due to ion mixing were calculated from the expression

$$\Omega^2 = \Omega^2_{irr} - \Omega^2_{unirr}, \quad (3)$$

where Ω^2_{irr} and Ω^2_{unirr} are the measured variances of the marker signals of the irradiated and unirradiated samples, respectively. The standard deviation for the broadening of the marker profile, σ, in units of depth, was calculated with the formula

$$\sigma = \Omega / N[\varepsilon]^{\text{in matrix}}_{K_M \text{ marker}}, \quad (4)$$

where N and $[\varepsilon]$ are the atomic number density of matrix atoms and the stopping cross section factor for scattering from the marker in the matrix, respectively. The effective diffusion coefficient for ion mixing is then

$$Dt = \sigma^2/2. \quad (5)$$

Typical backscattering spectra acquired at 77 K with 1.9 MeV He before and after Kr irradiation at 77 K are included in Fig. 2.2. The spectra here are for an Ag marker in Cu. The values of Dt derived from these data were found to be linearly proportional to the ion fluence, Ø. A linear relationship between Dt and Ø for all fluences is a common feature for ion mixing in metal marker systems at low temperatures [4], which is indicative of a stochastic diffusional processes. We have used this relationship between Dt and Ø as a criterion for the validity of our data. All samples were irradiated to two or more fluences.

To compare the data for different samples and irradiation energies requires a normalization. The natural procedure for irradiation phenomena is to divide the data by the damage energy per unit volume. (This is sometimes expressed in the equivalent units of displacements per atom.) To determine the damage energy per unit length and ions, F_D, at the marker depth for the various irradiations, the computer simulation

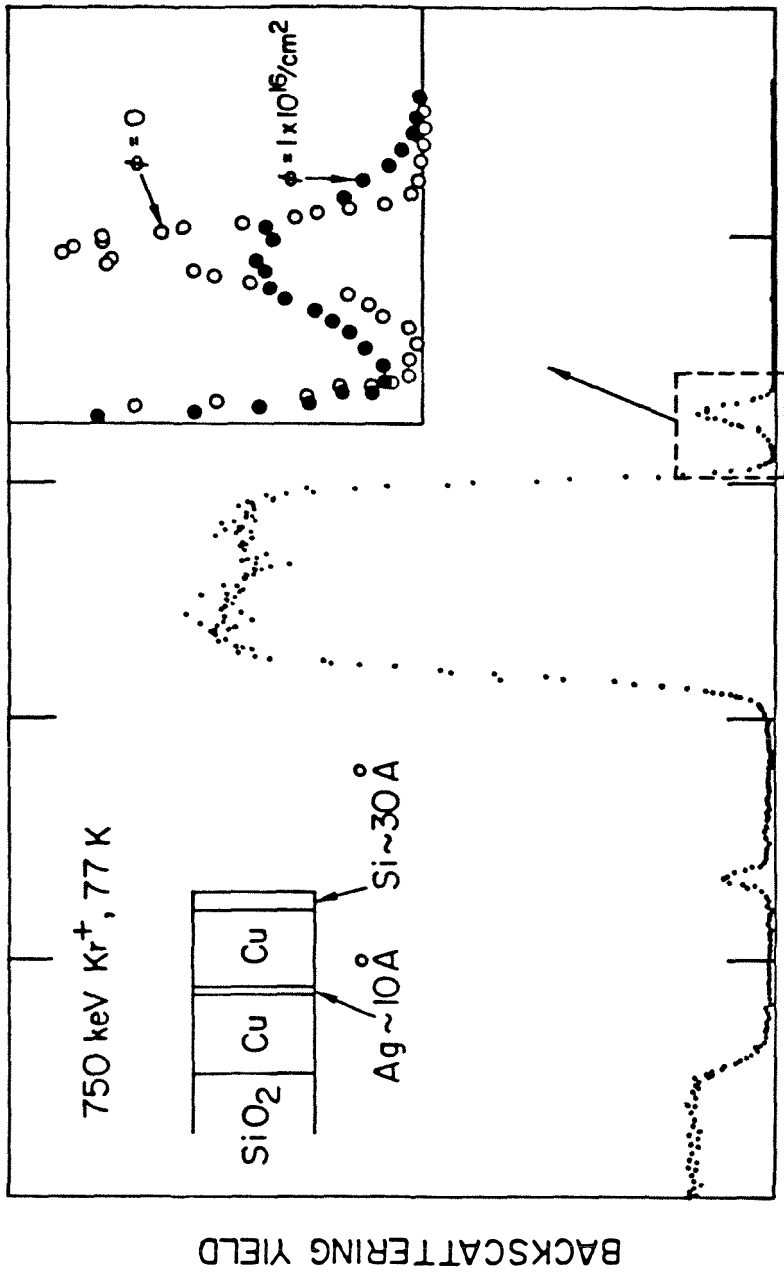

Fig. 2.2. Typical backscattering spectra showing the spreading of a thin marker upon ion irradiation. Here, the spectra illustrate Ag spreading in a Cu matrix for 500 keV irradiation at 77 K.

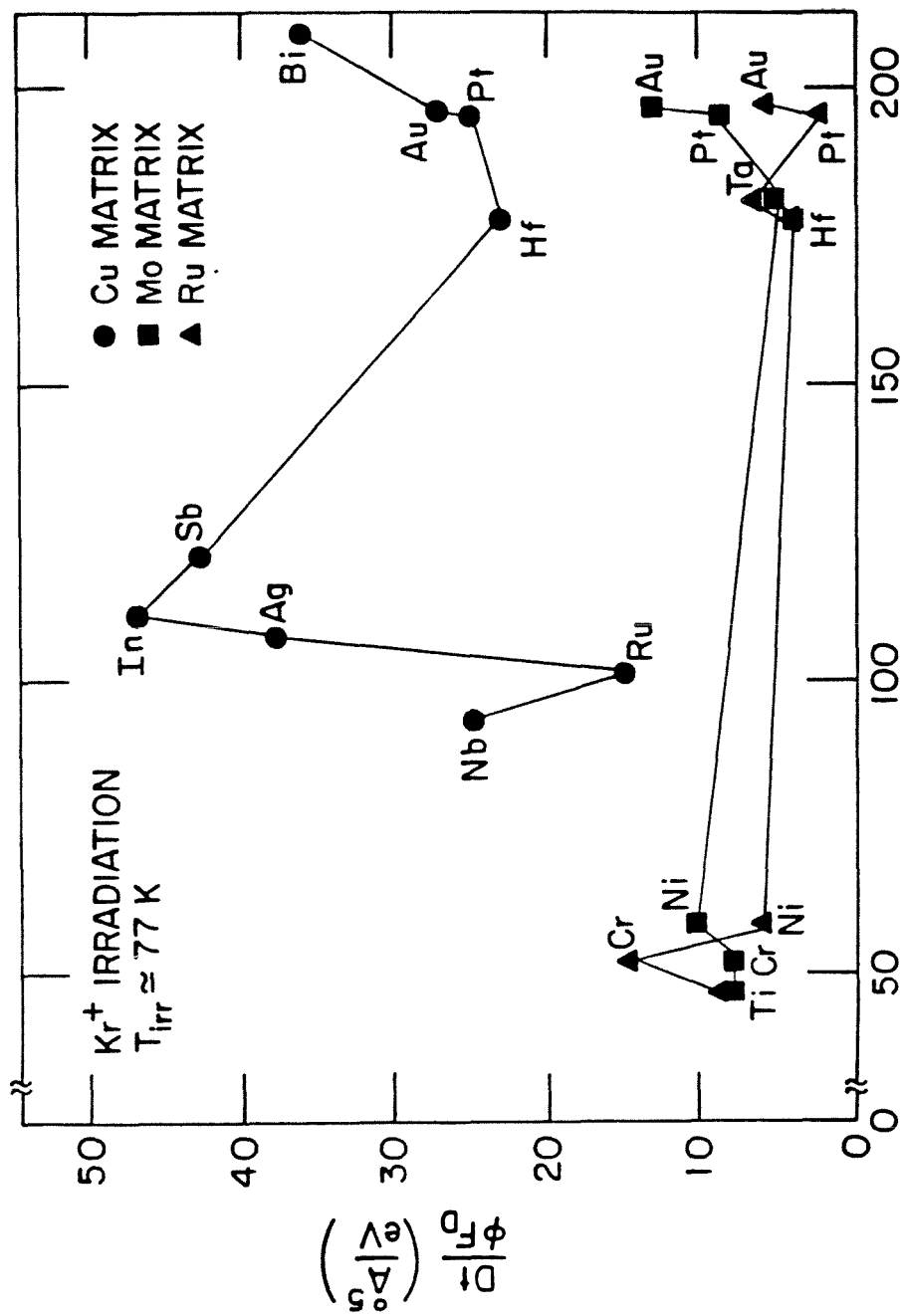

Fig. 2.3. Plot of the mixing efficiency as a function of their atomic mass of the marker for various markers in Cu, Mo and Ru matrices.

program, TRIM, was employed [5]. The data plotted are the values of the normalized mixing efficiency $\xi = Dt/\emptyset F_D$.

Fig. 2.1 shows the experimental mixing efficiencies of Si and Pt markers in Ge and that of predicted ones from theory. Note that the Pt marker mixes approximately 50 % easier than the Si marker. This is contradicts the prediction of the collisional theory, according to which Si should mix 20 times more than that Pt. The prediction is also off numerically by about factor of ten for both Si and Pt. The collisional model clearly fails to describe ion mixing correctly.

Fig. 2.3 shows values of $Dt/\emptyset F_D$ in Mo, Ru and Cu for various marker elements plotted in sequence of increasing atomic mass of the marker. The uncertainty in the mixing efficiencies is in the range of +/- 10 %. For markers in Mo and Ru matrices, the variation in the results is small; however, for the markers in Cu, the variation in the mixing is large and significant. There is no systematic dependence of mixing efficiency on the atomic mass of the marker. Variations of the mixing efficiency with the atomic mass of the marker are therefore small, in contrast with the collisional model.

In summary, this set of experiments illustrates that other mechanisms besides collisional effects dominate in ion mixing in these samples. The variation of mixing from marker to marker in the same matrix also indicates that the chemical identity of the marker plays a role in the mixing, so that properties such as the chemical affinity of the markers and the host, or transport phenomenon such as diffusivity, may be important to the mixing processes. To try to answer these questions we have conducted systematic experiments with a large number of systems. The results of these experiments are given in the following chapters.

2.3 References

[1] P. Sigmund, and A. Gras-Marti, Nucl. Instr. and Meth. 168 (1980) 339; and 182/183 (1981) 25.

[2] S. Matteson, B.M. Paine, and M-A. Nicolet, Nucl. Instr. and Meth. 182/183 (1981).

[3] W. Moeller and W. Eckstein, Nucl. Instr. and Meth. B7/8 (1985) 645.

[4] B. M. Paine and R.S. Averback, Nucl. Instr. and Meth. B7/8 (1985) 666.

[5] J. P. Biersack and L.G. Haggmark, Nucl. Instr. and Meth. 174 (1980) 257.

Chapter 3

THERMAL SPIKE; DEPOSITED DAMAGE ENERGY IN A CASCADE AND COHESIVE ENERGY OF THE MATRIX

3.1 Thermodynamical approach to ion mixing

As described in section 1.2 of chapter 1, at the end of the collisional phase of the cascade, there there can be an intense agitation of the atoms in the form of a thermal spike. A particularly instructive model for the diffusion induced by a thermal spike is that of Vineyard [1]. This model assumes that an initial energy per unit length, λ, is distributed along a straight line to represent the track of the incident ion, and that this energy is dissipated in the form of heat. The resulting temperature distribution evolves in time according to classical heat flow theory. The model further assumes that a thermally activated diffusional jumping process occurs in the hot region with a jump rate (number of jumps per unit volume per unit time),

$$\psi = A \exp(-Q/kT). \tag{1}$$

The total number of jumps in the cascade per unit length of the spike calculated under these conditions is

$$\eta = A \lambda^2 k^2 / 8\pi\kappa C Q^2, \tag{2}$$

where κ is the thermal lattice conductivity for heat conduction, and C is the heat capacity per unit volume of the target. Johnson et al. [2] have suggested that the activation enthalpy for the jumping process, Q in eqs. (1) and (2), is related to the

cohesive energy of the target. Van Rossum et al. [3] have in fact shown that for metallic bilayers, ion mixing does correlate with the cohesive energy.

Molecular dynamics computer simulations provide a very detailed picture of the dynamics of cascade processes which includes both the production of Frenkel pairs (i.e., vacancies and interstitial atoms) and the excitation of the lattice [4, 5]. These simulations indicate that point defects are produced during the collisional phase of the cascade and that they subsequently undergo stimulated motion during the thermal spike phase of the cascade. Unfortunately, these simulations have been performed for cascade energies of only a few keV, and mostly for potentials describing W. It is uncertain whether diffusion in higher energy cascades, or in cascades in less refractory metals, involves yet other diffusion mechanisms.

A simple point defect model for thermal spike diffusion has been developed [6] based on the results of these simulations. The model assumes that diffusion in cascades consists of normal radiation-enhanced diffusion, but that it is limited to very short times, $\approx 10^{-11}$ seconds, and to very high temperatures. The effective diffusion coefficient during the thermal spike is given by

$$D(t) = D_i c_i + D_v c_v, \tag{3}$$

where c_i and c_v are the instantaneous interstitial atom and vacancy concentrations within the thermal spike, respectively, and

$$D_i = D_{oi} \exp(-\Delta H^m_{1i}/\tau); \tag{4}$$

$$D_v = D_{ov} \exp(-\Delta H^m_{1v}/\tau). \tag{5}$$

ΔH^m_{1i} and ΔH^m_{1v} are the enthalpies of migration for single interstitial atoms and mono-vacancies, respectively, and τ is the product of Boltzmann's constant and spike

temperature. The initial point defect concentration is obtained using the Kinchin-Pease expression [7] for the number of point defects produced in a cascade and the tables of Winterbon [8] for the volume of the cascade at the end of the collision phase, $V_d(t=0)$. The initial temperature of the cascade is deduced from the expression,

$$3\tau = E_D/NV_d(t=0). \tag{6}$$

E_D is the total damage energy in the cascade; it too is obtained using the Winterbon tables [8]. The evolution of the temperature and point defect distributions are calculated by standard heat flow and reaction rate equations. The spreading of a thin marker is then calculated within this model using the expression [6]

$$\langle \Delta x^2 \rangle = 2\emptyset \int dT \, (d\sigma'/dT) \int NV_d(t)D(t)dt, \tag{7}$$

where $d\sigma'/dT$ is the cross section for producing a recoil of energy T, and $V_d(t)$ and $D(t)$ are the time dependent volumes and diffusion coefficients for cascades of energy T. Although this thermal spike model is in the spirit of Vineyard's, it specifies a diffusion mechanism, and semi-quantitative calculations can be performed. The physical parameters such as the energy density in the thermal spike and the cohesive energy are contained implicitly in this model through the diffusion coefficient and point defect concentrations. The energy density determines the temperature of the thermal spike. The point defect mobilities and the concentration of point defects produced in the thermal spike is related to the cohesive energy. In this chapter we test the predictions of this model by varying the target so as to affect the migration enthalpies, point defect concentrations, and spike temperature.

3.2 Experiments with matrices ranging from C to Au

To study how ion mixing depends on matrix properties, the use of isotopes to trace self diffusion would be ideal, but impractical and unwarranted. Tracer isotopes have been used in one study of ion mixing, Cu [9], and it was found that the results were close to those of suitably chosen marker impurities. Another approach, and the one employed here, is to measure the mixing for several markers in a matrix and to define an average mixing efficiency for the matrix from these measurements. Thus, the mixing efficiency for each matrix in this study represents an average over at least two markers. This minimum does not give a good average value, but it does prevent an extreme value of mixing from playing too dominant a role.

For this study, the experimental procedures were similar to those described in chapter 2. The marker samples were prepared by vapor deposition onto Si wafers with thick ($\approx$ 1 μm) SiO_2 surface layers. The substrates were cleaned organically, using Trichloroethylene, Acetone, and Methanol and immediately loaded into an electron gun evaporation system. The pressure was less than $\approx 10^{-7}$ Torr during evaporation. The matrix elements were C, Al, Ti, Fe, Ni, Cu, Mo, Ru, Ag, Hf, Ta, W, Pt, and Au, and marker elements were Al, Ti, Cr, Fe, Mn, Ni, Cu, Y, Nb, Mo, Ru, Ag, In, Sb, Hf, Ta, W, Pt, Au, and Bi. The markers were $\approx$5 ~15 Å thick, and were located at the mid-planes of the specimens which were $\approx$ 800 Å in total thickness. All of the matrix and marker elements, except C, were evaporated sequentially using e-beam heating in the same vacuum system without breaking vacuum. Carbon samples were prepared in another chamber by RF sputtering. A carbon layer was deposited first, followed by the deposition of the marker layer, and finally covered by the top C layer. A cover of Si, $\approx$30 Å thick, was deposited on the tops of most samples to minimize reactions with air after removing the samples from the vacuum system. The samples were irradiated at 6 K with Kr ions, in the range 500 and 1000 keV. The specific irradiation energy for

each matrix was selected so that the projected range of the Kr ions was approximately three times the initial marker layer depth. This condition yields damage distributions that are similar for all irradiations and that are not rapidly varying at the marker position. The average value of F_D within a 200 Å region centered at the initial marker depth was employed for normalization. The amount of ion mixing was measured by in situ backscattering spectrometry at 6 K with 1.9 MeV He ions. All the backscattering signals from the marker elements had Gaussian distributions both before and after the irradiations. The mixing efficiency for each system was obtained as described in chapter 2, page 13.

The results for the average mixing efficiencies in the various matrices are plotted in Fig. 3.1. The figure was constructed to explicitly illustrate how ion mixing is influenced by two physical properties of the target, i.e., the energy density of the cascade and the cohesive energy, as suggested by eq. (2). The ordinate in this plot is a measure of the square of the energy density in the cascades (λ^2 in eq.(2)), and the abscissa is a measure of the square of the inverse cohesive energy (the cohesive energy is related to Q in eq. (2)). The circles in the plot are located according to the energy density and cohesive energy of the matrix (indicated by the symbol in the circle). The average value of the mixing efficiency for all the different markers measured in that matrix at 6 K is indicated in the circle. The essential features of the figure are: (i) For a given value of the cohesive energy of the target, the mixing efficiency increases with increasing energy density. That increase is quite slow. (Note the logarithmic ordinate.) (ii) For a given value of the energy density, the mixing efficiency rises with decreasing values of the cohesive energy. That influence is much stronger than that of the damage energy.

Two choices were possible to represent the energy density in the plot, the linear energy density along the path of the projectile (λ), or the volume energy density associated with a thermal spike. For the relatively high energy ions employed in this

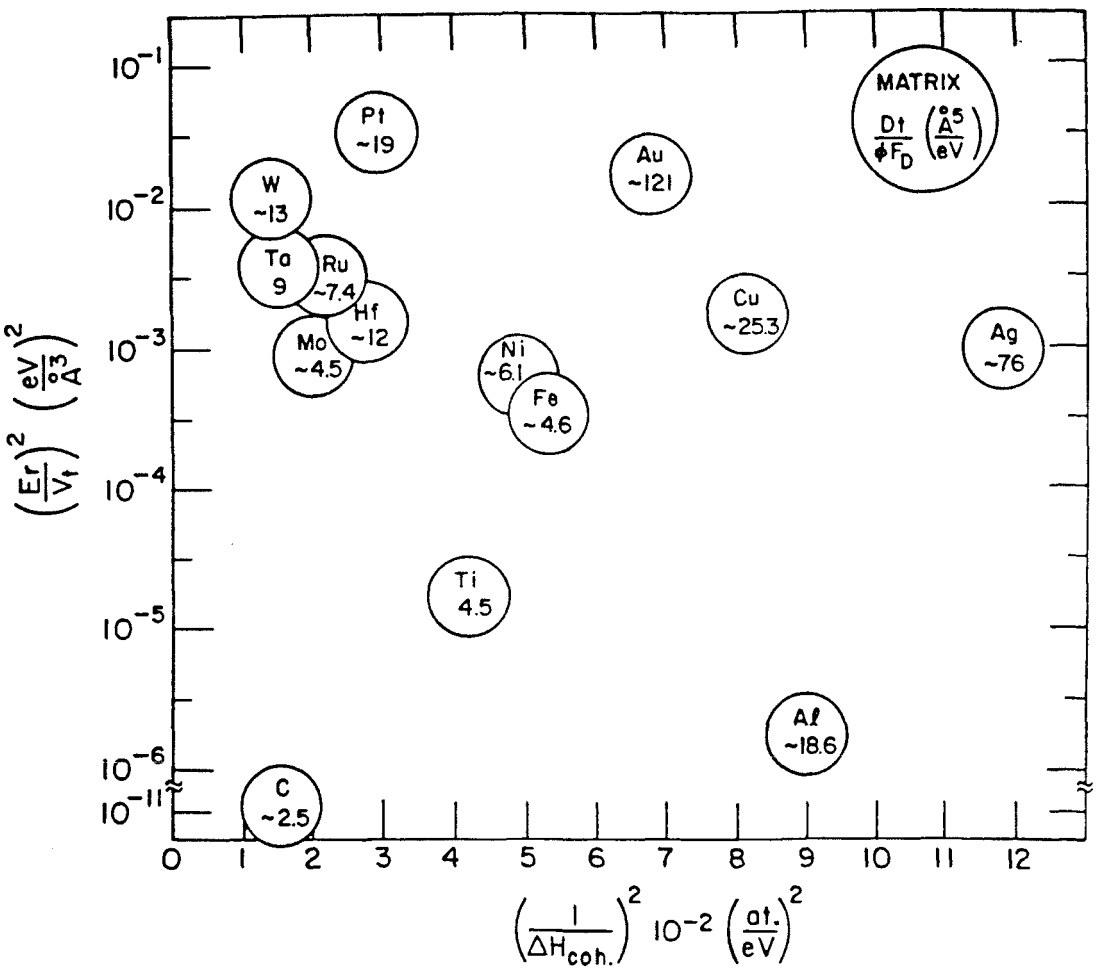

Fig. 3.1. Plot of the measured average mixing efficiency as function of the square of the energy density, the ordinate, and as a function of inverse square of the cohesive energy, the abscissa. The matrix element and its efficiency are identified in the circle.

study, the second choice was preferred. High energy ions have a long mean free path between high energy collisions and produce several isolated subcascades along their tracks [10, 11, 12]. This process is not well described by a smooth deposition of energy along the projectile track. The energy density for each target was therefore obtained from the damage energy within a "typical" subcascade, E_V, and the volume of these subcascades, V_t. The energy in the typical subcascade, $T_{1/2}$, was determined from the equation [13],

$$0.5 = 1/E_D \int_0^{T_{1/2}} dT\ (d\sigma'(E, T)/dT)\ E_D(T), \tag{8}$$

where $E_D(T)$ is the damage energy associated with a recoil of energy T, E_D is the total damage energy. Half of the damage energy, therefore, is deposited in subcascades with recoil energies greater than $T_{1/2}$, and half the damage energy is deposited in recoils below $T_{1/2}$. In this sense, $T_{1/2}$ is a typical recoil energy. The volume of the subcascade is determined from the expression [14],

$$V_t = 4/3\ \pi\ \{\beta\ (<\Delta x>^2+2<y>^2)\}^{3/2}, \tag{9}$$

where Δx and y are the longitudinal and transverse straggling of an atom with energy $T_{1/2}$, respectively, and β is a contraction factor relating individual cascades to distribution averages. Values for the straggling were obtained from Winterbon's tables [8].

As seen in Fig. 3.1, as the mixing increases the cohesive energy of the matrix decreases. The cohesive energy of the target is reflected through both the migration enthalpies and concentration of the point defects in the spikes. The former is derived from the Van Liemp or other similar relations [15] , and the latter from the Kinchin-

Table 3.1. Calculated values of the mixing efficiency using the radiation-enhanced diffusion model for thermal spike diffusion.

HOST	ΔH^m_{1v} (eV)	D_o(Å^{2}s^{-1})	$\langle\Delta x^2\rangle/2\Phi F_D$ (Å^5 eV^{-1})	
			Predicted	Measured
Ag	0.65	1.6×10^{15}	56	60-90
Al	0.61	8×10^{14}	24	20-40
Au	0.82	1.4×10^{14}	70	80-140
Cu	0.69	6×10^{14}	19	20-26
Fe	1.17	3×10^{14}	3	6-7
Mo	1.30	2×10^{15}	16	6
Ni	1.39	8×10^{14}	6	8-10
Pt	1.39	1×10^{14}	24	16-24
W	1.69	7×10^{13}	11	6-15

Pease expression noting that the displacement energy tends to correlate with cohesive energy. Cohesive energy especially tends to scale with the migration enthalpy of vacancies; for self-interstitial atoms this does not seem to be the case [16]. Thus, when interpreting the experimental results within the context radiation-enhanced diffusion process during the thermal spike, as described in section 3.1, it seems more appropriate to conclude that vacancy motion, and not interstitial motion, is the predominant mechanism of mixing. We also observe in Fig. 3.1 that the mixing efficiency increases as the energy densities in the cascades increase, which supports the hypothesis of thermal spike diffusion in cascades. The energy density in the cascades is important as it determines the spike temperature, eq (6).

We have compared an experimental value with that of calculated values from eq. (7) [17]. In this calculation, only vacancies were assumed to contribute to the diffusion process. To obtain best agreement, the vacancy migration enthalpies were taken to be one third of their reported values. The migration enthalpies are known to decrease for large concentration of point defects as during a thermal spike phase, [18]. The results of these calculations are listed in Table 3.1. Experimental and calculated values of the mixing efficiencies are within a factor of ≈ 2 of the experimental values. They also show the correct dependencies on cohesive energy and energy density.

From these results we conclude that the thermal spike mechanism plays a dominant role during ion mixing at low temperature and that a vacancy-like mechanism can account for the amount and trend of the observed mixing efficiencies.

3.3 References

[1] G.H. Vineyard, Radiat. Effects 29 (1976) 245.

[2] W.L. Johnson, Y.T. Cheng, M. Van Rossum, and M-A. Nicolet, Nucl. Instr. and Meth. B7/8 (1985) 657.

[3] M. Van Rossum, Y.T. Cheng, W.L. Johnson, and M-A. Nicolet, Appl. Phys. Lett. 46 (1985) 610.

[4] M.W. Guinan and J.J. Kinney, J. Nucl. Mater. 103/104 (1981) 1319.

[5] W.E. King and R. Benedeck, J. Nucl. Mater. 117 (1983) 26.

[6] D. Peak and R.S. Averback, Nucl. Instr. and Meth. B7/8 (1985) 561.

[7] G.H. Kinchin and R.S. Pease, Rep. Prog. Phys. 18 (1955) 1.

[8] K.B. Winterbon, Ion Implantation Range and Energy Deposition Distribution, Vol.2 (Plenum, New York, 1975).

[9] R.S. Averback, D. Peak, and L.J. Thompson, Appl. Phys. A39 (1986) 59.

[10] K.L. Merkle, in Radiation Damage in Metals, Eds. N.L. Peterson and S.D. Harkness (American Society of Metals, Metals Park, Ohio, 1976) p.58.

[11] R.S. Averback and M.A. Kirk, in Surface Alloying by Ion, Electron and Laser Beams, Eds. L.E. Rehn, S.T. Picraux, and H. Wiedersich (American Society of Metals, Metals Park, Ohio, 1986) p.91.

[12] Y.-T. Cheng, M-A. Nicolet, and W.L. Johnson, Phys. Rev. Lett. 58 (1987) 2083.

[13] R.S. Averback, R. Benedeck, and K.L. Merkle, Phys. Rev. B18 (1978) 4156. and R.S. Averback, J. Nucl. Mater. 108/109 (1982) 33.

[14] P. Sigmund, G.P. Scheidler, and G. Roth, BNL Rep. 50083 (C-52) (1968) 374.

[15] See i.e., J.L. Bouquet, G. Brèbec, Y. Limoge, in Physical Metallurgy, Eds. R.W. Cahn and P. Haasen, (North Holland, Amsterdam, 1983) p.386.

[16] See i.e., Vacancies and Interstitials in Metals, A. Seeger, D. Schumacher, J. Diehl, and W. Schilling, Eds. (North Holland, Amsterdam, 1970).

[17] D. Peak, 2nd Workshop on Ion Beam Mixing, Pasadena, Calif., 1985; and D. Peak and R.S. Averback, unpublished.

[18] M.W. Finnis, unpublished. Quoted by A.D. Brailsford and R. Bullough in J. Nucl. Mater. 69/70 (1978) 434.

Chapter 4

THERMAL SPIKE; KINETICS

4.1 Diffusion mechanisms during thermal spike

In the present chapter we investigate the importance of the thermochemical properties of the marker atoms in a given matrix during the thermal spike phase of ion mixing.

In chapter 2, from Fig. 2.3, we observe that the mixing efficiency varies from marker to marker. In that figure no correlation is observed between the atomic mass of a marker and the mixing efficiency, but the results of chapter 3 suggest that such properties as the chemical nature of the tracer impurity might be significant during the thermal spike phase of ion mixing. We thus studied such effects by investigating the correlation of tracer impurity diffusion with ion mixing efficiencies.

Marker species that influence ion mixing efficiency have been noted previously for the semiconductor matrices, Si [1] and for the metallic matrix, Hf [2]. These studies, however, were limited to a few markers. Only in Al has ion mixing been measured at low temperatures for a large number of markers, and no significant variation was observed [3]. We have investigated further the possibility of such a correlation, and have considered its significance from an atomistic point of view of diffusion.

In attempting to correlate the ion mixing efficiency with the diffusivity of the impurity, an ambiguity arises, since impurity diffusion is temperature dependent, i.e.,

$$D_{imp}=D_o\exp(-Q/kT). \qquad (1)$$

D_{imp} is the impurity tracer diffusivity, D_0 is a prefactor, and Q is the activation enthalpy for diffusion. To correlate mixing efficiency with impurity diffusivities, a "comparison temperature" must be selected. An alternative is to correlate ion mixing with D_0 or Q separately. For the present, we correlate the mixing efficiency with impurity diffusivity (obtained by extrapolation) at the melting temperature of the matrix. At this temperature, D_{imp} is far more sensitive to changes in Q than in D_0, so this correlation is effectively a correlation between ion mixing and Q.

We also tried to identify the type of diffusion mechanism that contributes to ion mixing by correlating the markers' thermochemical properties and the ion mixing efficiencies. Vacancy and interstitial mechanisms for diffusion of tracers have been theoretically well developed in Cu, Ag, and Au solvents [4, 5] on the basis of an electrostatic interaction between impurity atoms and point defects. The potential created at a distance, r, from an impurity atom due to the change of electron density is expressed by a screened Thomas-Fermi potential; $(Ze/r)\cdot\exp(-qr)$, where q is the screening constant and Z is the excess valence of an impurity atom from monovalent Cu or Ag (i.e., Z=1 for Zn and Z=-1 for Ni). Representing a vacancy in monovalent Cu or Ag as an effective charge, -e, at the vacant site, corresponding to the removal of an ion of charge +e, and similarly assigning +e for the interstitial, interaction energies and parameters for impurity diffusion due to vacancies or interstitials can be calculated. For the vacancy mechanism, the activation energy of impurity diffusion in Cu or Ag becomes smaller than that of self-diffusion as Z becomes positive, and it becomes larger as Z becomes negative. For the interstitial case, the effect is opposite. This theory agrees well with the experimental data of impurities for thermal diffusion in Cu, Ag, and Au. This agreement suggests that one could try to correlate ion mixing efficiencies with the excess valency Z of markers in the mixing results to get clues on the diffusion mechanism during ion mixing.

We also investigated the diffusion mechanism by correlating the interatomic interactions between the solvent and impurity atoms and the mixing results. More specifically, we compared the difference of binding enthalpies between the solvent and impurity atoms (H_{AB}) and solvent atoms (H_{AA}), H_{AB}-H_{AA}, and the mixing results. The quantity, H_{AB}-H_{AA}, would qualitatively relate to the potential well depth of atomic diffusion. When this quantity is positive, the energy required to surmount the activation barrier is lowered and when it is negative the energy is increased. Such a quantity has been used to relate the binding energy of a vacancy to an impurity atom [6]. The difference, H_{AB}-H_{AA}, however, is not easily available for the systems in our experiment. It can be expressed [6] in terms of more accessible parameters such as the cohesive energies of solvent and solute atoms and the heat of mixing. The basic steps in that derivation [6] are as follows: The energy change induced by transferring an A atom from its surrounding A atoms to infinity is $-zH_{AA}$, where z is the coordination number. When a B atom is placed on the site vacated by the A atom, the energy change is zH_{AB}. The total energy produced by the system in these steps is $z(H_{AB}-H_{AA})$. One can reach the same state by another path. As we add a B atom from infinity to a B crystal, the cohesive energy H_B is gained. The energy gained by transferring that B atom from the B crystal to a dilute AB solid solution is the heat of mixing, δ. No energy is involved when an A atom that is surrounded by A atoms in the dilute AB crystal, is removed to a A crystal. The cohesive energy H_A is lost when an A atom is removed from a crystal to infinity. The total energy change in these steps is $H_A-H_B-\delta$.

Since above two processes are the same, we can equate the energy changes involved in these two processes,

$$z(H_{AB}-H_{AA}) = H_A-H_B-\delta \qquad (2)$$

or

$$H_{AB}-H_{AA} = (H_A-H_B-\delta)/z$$

The cohesive energies H_A and H_B are those of the solvent and solute atoms (taken from [7]) and δ is the heat of mixing (taken from [8]). If the ion mixing mechanism is indeed related to the thermal diffusion mechanism, then we should observe a correlation between H_{AB}-H_{AA} and the mixing results.

4.2 Experiments with Cu, Ag, and Zr matrices

For this experiment we have used Cu, Ag, and Zr as matrices. We chose Cu and Ag for several reasons. Both Cu and Ag have low cohesive energies (meaning high point defect concentration with high defect mobilities [9]), and cascades with high energy density (high cascade temperature [9]) both of which favor thermal spike diffusion. In addition, the properties of point defects and impurities in these materials have been extensively studied. In Zr, various impurities diffuse thermally by either an intestitial or a vacancy mechanism. So, we used the Zr matrix also to compare the ion mixing of markers that diffuse interstitially with that of markers that diffuse by a vacancy mechanism during thermal impurity diffusion. It has been suggested [10, 11] that at low temperature, the interstitial mixing mechanism dominates the atomic transport process. If that suggestion is correct, the markers that diffuse interstitially in Zr would mix more than the markers that diffuse by a vacancy mechanism.

The samples were prepared in a similar way as other samples for experiments in the previous chapters. The marker layers for the Cu matrix were Nb, Ru, Ag, In, Sb, Hf, Pt, Au, and Bi. For Ag matrix, the marker layers were Al, Ni, Cu, Ta, W, Pt, Pb, and Bi. These markers have a wide range of thermochemical properties in Cu and Ag matrices. The markers for the Zr matrix were Ti, Cr, Fe, Co, Ni, Cu, Hf, W, and Au. Cr, Fe, Co, Ni, and Cu are known as fast diffusers in Zr; Ti, Hf, W, and Au have diffusivity values similar to that of Zr self-diffusion.

For the Cu and Zr matrices the experiments were performed using the same accelerator both to induce mixing and to analyze the specimens by He backscattering spectrometry. The irradiations were carried out at 77 K with 750 keV Kr ions for doses from 0.5 to $2x10^{16}$Kr/cm^2. For most of the Ag matrices the irradiations were conducted at 77 K with 330 keV Kr ions at doses from 3 to $7x10^{15}$ Kr/cm^2 and analyzed at room temperature by He backscattering spectrometry. Ag samples with Al and Pt were irradiated with 650 keV Kr at 7 K with in situ backscattering analysis and the sample with the Cu marker was irradiated with 750 keV Kr at 77 K with in-situ analysis. All the backscattering signals from the marker elements had Gaussian distributions both before and after the irradiations. Mixing efficiency for each system was obtained as described in chapter 2, page 13.

To illustrate the correlation of impurity diffusivity of various markers in Cu with ion mixing results, Fig. 4.1 plots the thermal diffusivity D_{th} of an impurity versus its mixing efficiency. The impurity diffusion data are from [12, 13]. The diffusivity values indicated in the figure were obtained by extrapolating the literature data to the melting point of Cu (T_0=1357 K). We include in this figure, and also in Fig. 4.2, experimental mixing efficiencies from other references [14, 15]. These other mixing efficiencies fit well with ours. Fig. 4.1 reveals a systematic relationship between the thermal diffusion and the marker mixing efficiency of an impurity in Cu: as the thermal diffusivity increases, the mixing efficiency also increases. This result suggests that the two phenomena are related, and it provides strong support for the hypothesis that thermally-enhanced diffusion during the lifetime of the cascade is the main contribution to ion mixing. We observed a similar correlation for ion mixing data of markers in the Ag matrix.

In Fig. 4.2 and 4.3, we plot the measured mixing efficiencies and the quantity, H_{AB}-H_{AA}. Both figures show that H_{AB}-H_{AA} does correlate with the measured mixing efficiencies. If the ion mixing mechanism is related to that of the

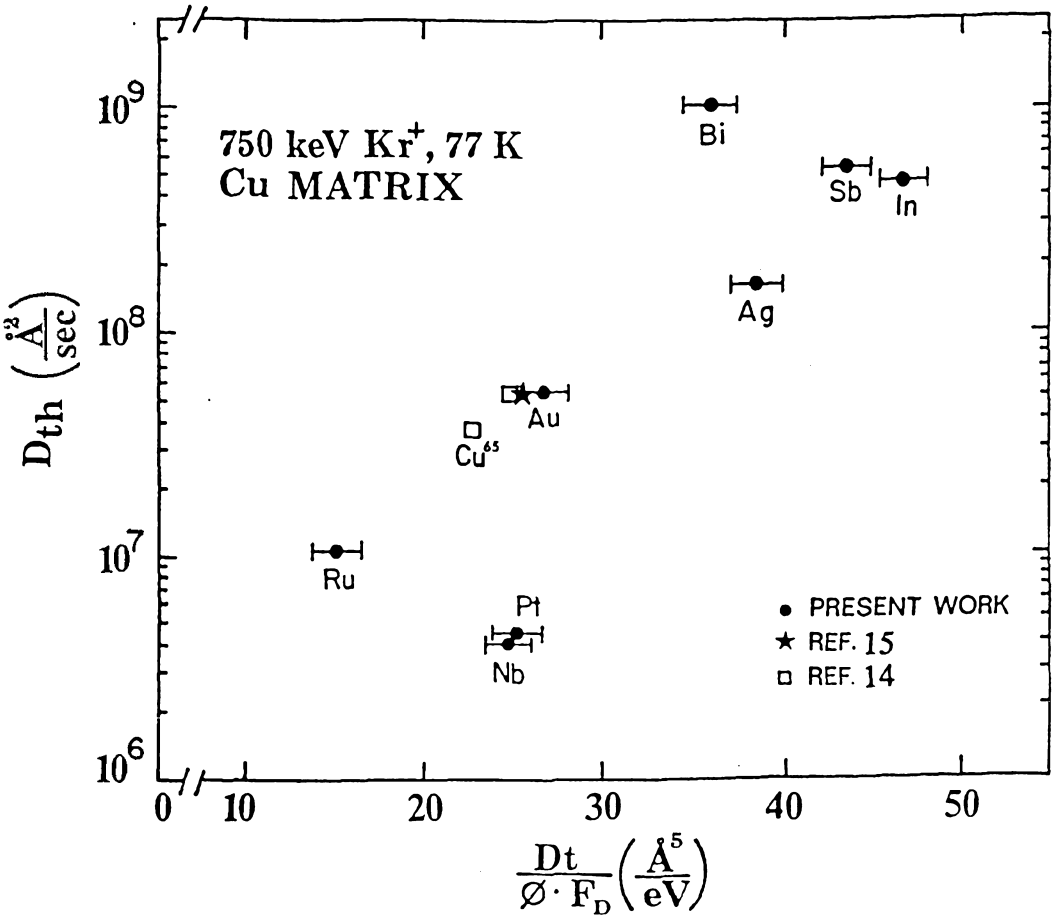

Fig. 4.1. The values of experimental mixing efficiencies $Dt/\emptyset F_D$, as a function of the thermal diffusivities of markers in a Cu matrix. The mixing results from refs. [14] for a Cu^{65} and Au marker and [15] for a Au are obtained with 500 keV and 460 keV Xe respectively at 10 K.

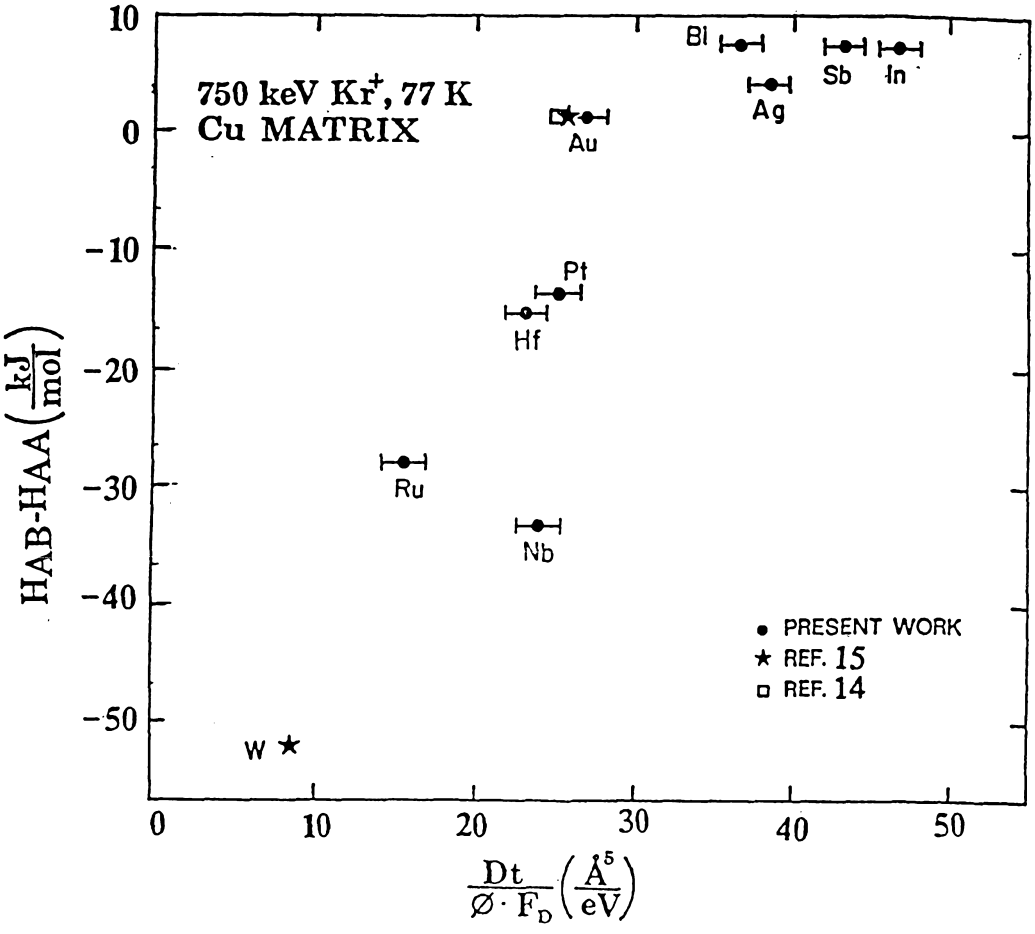

Fig. 4.2. The values of experimental mixing efficiencies, $Dt/\O F_D$, as a function of the H_{AB}-H_{AA} with the markers in Cu. The mixing results from refs. [14] for a Cu^{65} marker and [15] for a Au and W are obtained with 500 keV and 460 keV Xe, respectively, at 10 K.

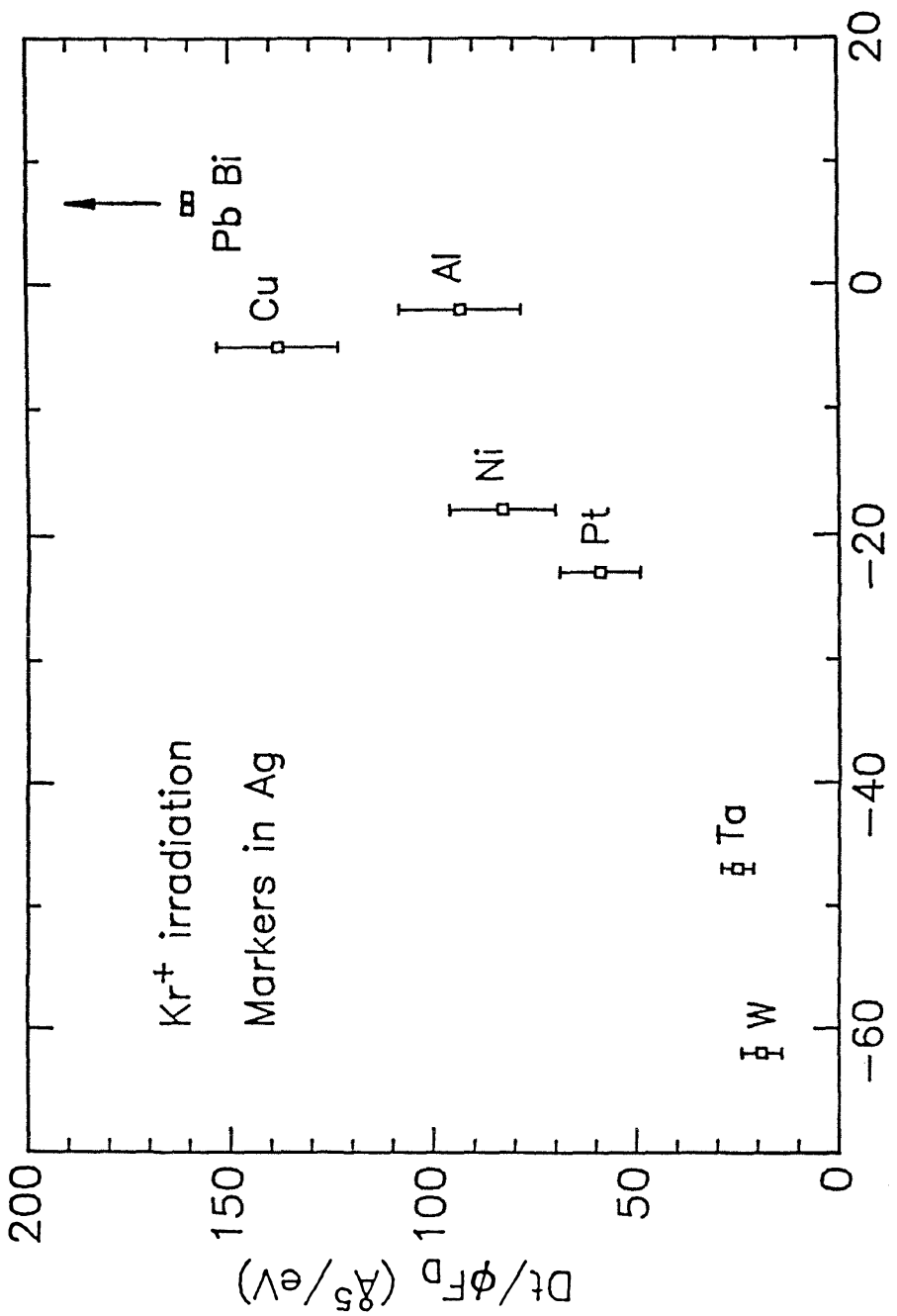

Fig. 4.3. H_{AB}-H_{AA} as a function of the mixing efficiencies.

thermal diffusion, then the mixing efficiencies should also correlate with the point defect properties that are germane to the thermal diffusion of the impurities. It is known [5] that the vacancy mechanism is dominant for thermal impurity diffusion in both Cu and Ag. We note that the impurities with positive excess valency in Cu (In, Sb, and Bi) and also that in Ag (Al, Pb and Bi) all have higher mixing efficiencies than impurities with negative Z in Cu (Nb, Ru, and Pt) and in Ag (Ni, Ta, W, and Pt). Hence, it seems that the transport of marker atoms during ion mixing could be by the vacancy mechanism as from the electrostatic diffusion theory [4, 5]. These results agree with the conclusions of chapter 3, where we have seen some evidence that the vacancy mechanism could be dominant during thermal spike diffusion.

The experimental results of markers in the ß-Zr matrix are listed in Table 4.1. In Fig. 4.4 we plot some of the data versus H_{AB}-H_{AA}. In polyvalent Zr , which also has a large atomic size, Cr, Fe, Co, Ni and Cu, which have small ion size and low valence, are likely to dissolve interstitially, while Ti, Hf, W, and Au, which have high valence and large ion size, are likely to dissolve substitutionally [16]. Except for Cr, the atoms of the first group have diffusivities that are higher by an order of magnitude than the self-diffusivity of Zr, and Cr diffuses 3 to 6 times faster than self-diffusion of Zr [16]. In Table 4.1, the mixing efficiencies of the various markers differ by at most 100% (Cu $\approx$ 8.1 and Au $\approx$ 16 $Å^5$/eV). As a group, the mixing efficiencies are greater for markers that have low thermal diffusion (vacancy-like solutes) than the markers that have high thermal diffusion (interstitial-like solutes). This pattern seems to indicate again that vacancies could play a role for atomic transport in ion mixing. In Fig. 4.4, where the measured mixing efficiency is plotted against the H_{AB}-H_{AA}, a correlation exists. The correlation is weak because of a small range of mixing efficiencies for different markers in Zr. The markers believed to thermally diffuse interstitially is not plotted since the correlation does not exist. The correlation suggests that the vacancy mechanism could

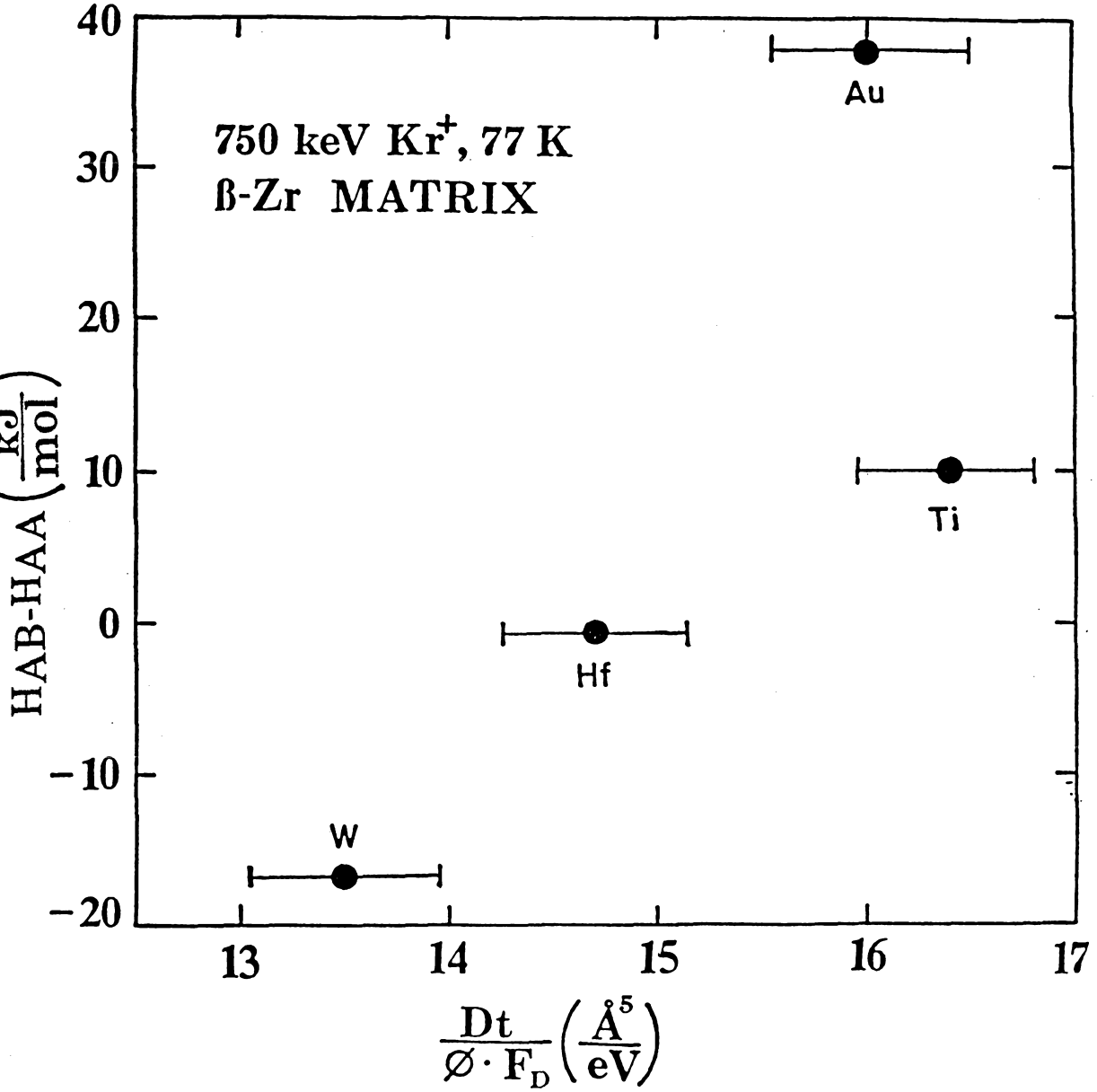

Fig. 4.4. The values of experimental mixing efficiencies, $Dt/\O F_D$, as a function of H_{AB}-H_{AA} with the markers in Zr.

Table 4.1. Compilation of ion mixing results for markers in the Zr matrix.

Substituional-like markers	$Dt/\emptyset F_D$ ($Å^5/eV$)
Ti	16
Hf	15
W	13
Au	16
Interstitial-like markers	**$Dt/\emptyset F_D$ ($Å^5/eV$)**
Cr	15
Fe	12
Co	13
Ni	12
Cu	8

play an important role in the atomic transport during ion mixing (at least for those solutes that diffuse thermally by lattice diffusion).

The results of this chapter and their correlation with thermal diffusion parameters indicate that the thermally activated atomic transport processes are indeed effective during a thermal spike in ion mixing, as was to be expected from the discussion in chapter 3.

4.3 References

[1] A.J. Barcz, B.M. Paine, and M-A. Nicolet, Appl. Phys. Lett. 44 (1984) 45.

[2] R.S. Averback and D. Peak, Appl. Phys. A38 (1985) 139.

[3] A. Barcz and M-A. Nicolet, Appl. Phys. A33 (1984) 167.

[4] D. Lazarus, Phys. Rev. 93 (1954) 973.

[5] A.D. Le Claire, Philos. Mag. 7 (1962) 141; and also 10 (1964) 641.

[6] A. Seeger, Lattice Defects and Their Interaction, Ed. by R.R. Hasiguti (Gordon and Breach, New York 1962) p. 181.

[7] C. Kittel, Introduction to Solid State Physics, 5th ed. (Wiley, New York 1976) p.74.

[8] A.K. Niessen, F.R. de Boer, R. Boom, P.F. de Chatel, W.C.M. Mattens: Calphad 7 (1983) 51.

[9] D. Peak, R.S. Averback, Nucl. Instr. Meth. B7/8 (1985) 561.

[10] P. Sigmund, Appl. Phys. A30 (1983) 43.

[11] J. Bøttiger, S.K. Nielsen and P.T. Thorsen, Nucl. Instr. and Meth. B7/8 (1985) 707.

[12] C.J. Smithells (Ed.), Metals Reference Book, 5 th ed. (Butterworths, London 1976) pp. 13-14.

[13] R.C. Weast, Handbook of Chemistry and Physics, 58th ed. (CRC Press, Cleveland 1978) p. F-63.

[14] R.S. Averback and L.J. Thompson, unpublished (1984).

[15] J.F.M. Westendorp, Ph.D. Thesis, FOM-Institute for Atomic and Molecular Physics (1986) p. 87.

[16] R. Tendler, E. Santos, J. Abriata and C.F. Varotto, Thermodynamics of Nuclear Materials, Vol. 2 (IAEA, Vienna, 1975) p. 71.

Chapter 5

THERMAL SPIKE; HEAT OF MIXING

5.1 Chemical effects in thin marker layer systems

Among many important factors that influence ion mixing, it has been observed that the chemical properties of the target atoms can be quite important [1, 2]. In particular, the heat of mixing, ΔH_{mix}, is known to significantly influence the ion mixing of bilayer systems [3]. Similarly, the difference in electronegativity between the atoms seemed to have a strong influence in the amount of mixing in bilayers [4]. In the present chapter, we report a systematic study on the effect of the heat of mixing in ion mixing of thin marker layers embedded in a homogeneous matrix.

In chapter 3, equation 3 shows a general diffusion coefficient during the thermal spike, under which the defects migrate during the high transient spike temperature. The random walk of atoms during diffusion can be biased by chemical effects. This biasing can be included in that diffusion coefficient by including the Darken factor [5]. The diffusion coefficient is then given by

$$D^*=D(t)x(1-2\Delta H_{mix}/kT). \quad (1)$$

Here, ΔH_{mix} is the heat of mixing per atom which can be expressed as

$$\Delta H_{mix}=2\delta C_A C_B, \quad (2)$$

where δ is the nearest neighbor bond energy difference of Miedema [6] and C_A and C_B are the local concentrations of atoms A and B. Thus the magnitude of ΔH_{mix} depends

on the atomic concentration of marker and matrix atoms in the marker region. If the marker atoms are atomically dispersed during irradiation, their concentration becomes dilute and the ΔH_{mix} value becomes negligibly small. Thus, we should not observe effects of the heat of mixing if our markers are indeed dilute enough that their atoms diffuse independently. If we observe such chemical effects, then the mixing results that we have reported so far could have been influenced by chemical effects and would require different interpretations. It has nonetheless been claimed that in Cu the ion mixing results of markers, such as W and Au, correlate with the heat of mixing [7]. In that study the nominal thickness of markers was 4 to 6 Å, which is a little thinner than the usual markers in our samples. A cross-sectional TEM micrograph of an irradiated W marker established that the marker was dispersed [7]. The heat of mixing should thus play a negligible part under those conditions. To confirm the validity of our dilute marker systems for investigating the basic mechanisms of ion mixing, we have therefore investigated the effects of heat of mixing in a systematic way with markers in Cu, Mo, and Ru matrices.

5.2 Experiments with Cu, Mo, and Ru matrices

Mo and Ru are chosen as matrix atoms and Ti, Cr, Mn, Ni, Hf, Ta, Pt, and Au are used as thin markers in each of the two matrices. Mo and Ru have similar mass, density, cohesive energy, and thermal conductivity. Collisional or thermal spike effect will be similar too. However, for a given marker, the heat of mixing with Mo and Ru is very different. By comparing the mixing results for a marker in Mo and Ru, one can thus recognize the presence of major chemical effects in the mixing. The Cu matrix was included as well because of the claim mentioned earlier [7].

The marker samples for Mo and Ru matrices were prepared similarly to other samples for experiments in previous chapters and the experimental conditions are the

same as described in chapter 2. For Cu marker samples, we used the same set of samples and experimental conditions as in chapter 4. All the backscattering signals from the marker elements had Gaussian distributions both before and after the irradiations. The mixing efficiency for each system was obtained as described in chapter 2, page 13.

The results are shown in Fig. 5.1, where the mixing efficiency, $Dt/\emptyset F_D$, is plotted as a function of the heat of mixing parameter δ. Although there are variations in mixing efficiencies for the different markers in each matrix, and the same markers in the two matrices, as large as a factor of ≈ 5, there is no obvious trend between the mixing efficiency and the heat of mixing.

We, thus conclude that within the precision of our experiment the chemical interaction between dilute marker atoms and the matrix plays a negligible role in determining the ion mixing results. A similar conclusion has been drawn before using the solid solubility of markers and matrix atoms as the parameter to test for a chemical interaction between marker and matrix [8].

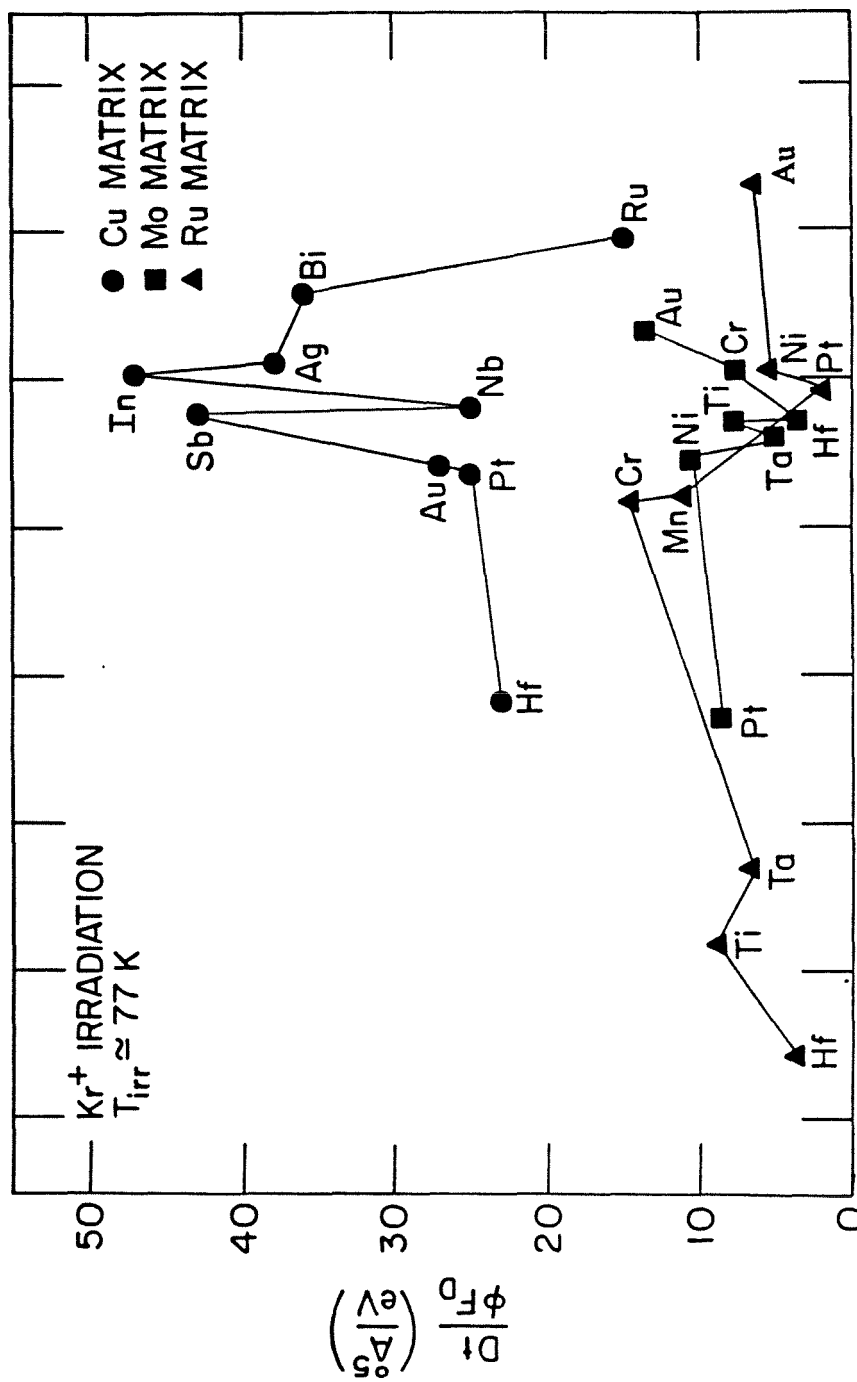

Fig. 5.1 Plot of mixing efficiency as a function of the heat of mixing parameter, δ, between various marker elements with Cu, Mo, and Ru matrices.

5.3 References

[1] Z.L. Wang, J.F.M. Westendorp, S. Doorn, F.W. Saris, Materials Research Society Proceedings, Vol. 7, Eds. S.T. Picraux, and W.J. Choyke, (1981) p. 59.

[2] T. Banwell, B.X. Liu, I. Golecki, and M-A. Nicolet, Nucl. Instrum. Methods, 209/210, (1983) 125.

[3] Y.-T. Cheng, M. Van Rossum, M-A. Nicolet, and W.L. Johnson, Appl. Phys. Lett., 45 (1984) 185.

[4] F. d'Heurle, J.E.E. Baglin, and G.J. Clark, J. Appl. Phys., 57 (1985) 1426.

[5] P.G. Shewmon, Diffusion in Solids (McGraw-Hill, New York, 1963) p. 126.

[6] A.R. Miedema, Phillips Tech. Rev., 36 (1976) 217.

[7] J.F.M. Westendorp. Ph.D. Thesis, FOM-Institute for Atomic and Molecular Physics (1986). p.87.

[8] S. Matteson, B.M. Paine, M.G. Grimaldi, G. Mezey and M-A. Nicolet, Nucl. Instrum. and Methods, 182/183 (1981) 43.

Chapter 6

RADIATION-ENHANCED DIFFUSION; ACTIVATION ENERGY AND DIFFUSION MECHANISM

6.1 Theory of radiation-enhanced diffusion

We have shown in the previous chapters that during ion mixing in heavy matrices with heavy ions in the low temperature regime, the total amount of the atomic displacements is mainly controlled by the thermal spike mechanism, where diffusion by a vacancy-like mechanism plays a dominant role. In the high temperature regime, where radiation-enhanced diffusion is dominant, diffusion by an interstitial-like mechanism is believed to contribute during ion mixing [1]. In this section, we will review the basics of radiation-enhanced diffusion to facilitate the discussion of our results within the frame of radiation-enhanced diffusion. The theory assumes that the volume under consideration is uniformly irradiated by traversing particles.

During ion irradiation at high ambient temperature, the defects created are mobile, and the diffusion coefficient, D_{irr}, can be expressed as

$$D_{irr}=K_v(V+V_o)\nu_v a^2+K_i(I+I_o)\,\nu_i a^2, \qquad (1)$$

where K_v and K_i are the vacancy and interstitial correlation factors, V and I are the excess vacancy and interstitial concentrations created by irradiation, V_o and I_o are the thermal equilibrium vacancy and interstitial concentrations, ν_v and ν_i are the jumping frequencies and a^2 is the square of interatomic distance. Equation 1 can be rewritten in the form of an excess diffusion coefficient that exceeds that for thermal diffusion,

$$D_{irr}=(K_vV\nu_va^2+K_iI\nu_ia^2)+D_{th}=D_{ex}+D_{th}, \quad (2)$$

where the excess diffusion coefficient, D_{ex}, is directly proportional to the excess vacancy (V) and interstitial (I) concentrations.

It is assumed in the radiation-enhanced diffusion theory that the Frenkel pairs are the main defects created by irradiation and the rate of vacancy creation (G_v) and interstitial creation (G_i) is the same ($G=G_v=G_i$). Annihilation of the radiation-produced point defects is also induced and assumed to take place in two ways: (1) by vacancies and interstitials migrating to homogeneously distributed fixed sinks such as dislocations, and (2) by direct recombination of vacancies and interstitials.

With the above principles, we can write the equations that give the concentrations of point defects in the form

$$\begin{aligned} dC_v/dt&=G-ND_vV-(V+V_O)(I+I_O)(\nu_i+\nu_v)Z, \quad D_v=(a^2\nu_v),\\ dC_i/dt&=G-ND_iI-(V+V_O)(I+I_O)(\nu_i+\nu_v)Z, \quad D_i=(a^2\nu_i), \end{aligned} \quad (3)$$

where C_v and C_i are total vacancy and interstitial concentrations in the irradiated volume in a given time, N is the density of fixed sinks and Z is the recombination volume of vacancies and interstitials.

When the steady state is reached, $dC_v/dt=dC_i/dt=0$, and $D_vV=D_iI$, or $\nu_vV=\nu_iI$. In the temperature range where we examined the radiation-enhanced diffusion, $I>>I_O$ and $\nu_i>>\nu_v$, so we can approximate $I+I_O=I$ and also $\nu_i+\nu_v=\nu_i$. Thus, by solving the steady state equation, we can obtain the excess vacancy and interstitial concentration as follows:

$$V=-(ZV_O+Na^2)/2Z+[(ZV_O+Na^2)^2+4GZ/\nu_v]^{1/2}/2Z. \quad (4)$$

The general solution for the radiation-enhanced diffusion coefficient would be $D_{irr}=(K_v+K_i)D_vV+D_{th}$. In a usual radiation-enhanced diffusion experiment the irradiation temperature is not high enough to allow any thermal diffusion and have any significant thermally created point defect concentration, $4GA/v_v>>(ZV_o+Na^2)^2$ [1]. Thus, we can approximate the radiation-enhanced diffusion coefficient as

$$D_{irr}=(K_v+K_i)(GD_va^2/Z)^{1/2}. \quad (5)$$

The activation energy of diffusion by the interstitial or the vacancy mechanism can be seen from this equation to be 1/2 of the vacancy migration enthalpy, $1/2H_v^m$, as was shown previously by Dienes and Damask [2]. Such a dependence of $1/2H_v^m$ on radiation-enhanced diffusion also has been established earlier for ion mixing [1, 3, 4]. The activation energy during radiation-enhanced diffusion is essentially the migration enthalpy of whatever defects that contribute to diffusion. Since these defects have been already created during collisional phase, the formation energy is assumed not to be incorporated in the activation energy observed in the radiation-enhanced diffusion experiment data. One cannot conclude that diffusion during radiation-enhanced diffusion is due to the vacancy mechanism, since the activation energy for the interstitial mechanism during radiation-enhanced diffusion is also $1/2H_v^m$ [2].

6.2 Various diffusion mechanisms under non-thermal equilibrium concentration of point defects

From eq. (5) the activation energy of atomic transport during radiation-enhanced diffusion is 1/2 of the vacancy migration enthalpy. In the present section of this chapter, we discuss some of the possible atomic transport mechanisms that could

have led to such low activation energy during radiation-enhanced diffusion. In the next section we discuss the experimental results.

There are many ways or mechanisms by which the impurity solutes migrate in any given host material. The observed diffusivity depends on the relative dominance of each mechanism. Generally, the total impurity diffusivity can be written as the sum

$$D_t=\Sigma_i C_i D_i, \tag{6}$$

where C_i is the average fraction of time that the impurity spends in the ith mechanism, and D_i is the diffusivity of that mechanism.

Among many, there are basically three mechanisms by which the impurity atoms can diffuse with a migration enthalpy that is a fraction of the vacancy migration enthalpy[5]. We consider that these three types of D_i's are likely to contribute to mixing during radiation-enhanced diffusion: conventional interstitial, interstitial-vacancy pair, and mixed-dumbbell or self-interstitial-solute-atom complex.

1) Conventional interstitial mechanism

In the conventional interstitial mechanism, an atom would sit at the center of an interstitial site surrounded by substitutional atoms as indicated in Fig.6.1. Diffusion by conventional interstitial mechanism is possible for some impurities with very small atomic size, like hydrogen or carbon, in a solvent with large atomic size. During ion irradiation, conventional interstitials can be created and may contribute to the diffusion. This mechanism involves only a single jump frequencies, w_i, of interstitials. No other defects are required for the jumps which are uncorrelated. Thus the correlation factor K_i is 1 and

$$D_i=(Z/6)a^2 w_i, \tag{7}$$

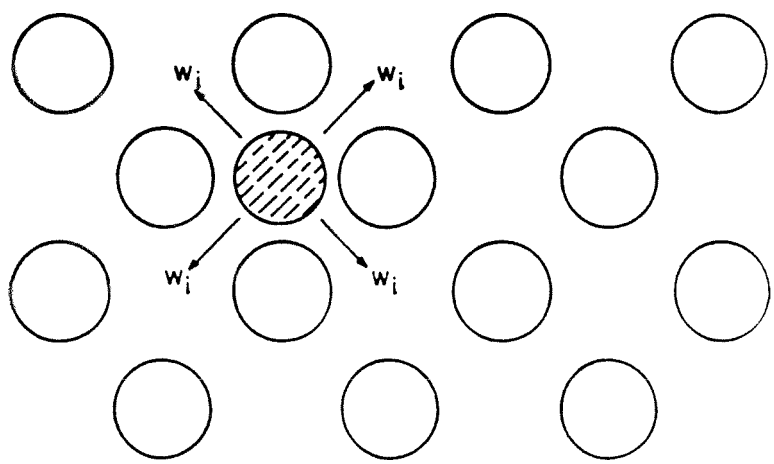

Fig. 6.1. Model of the conventional interstitial mechanism of diffusion. The dashed sphere is the solute with w_i jump frequency among solvent atoms.

where Z is the number of accessible interstitial sites and a is the separation between them. For the markers that we used for our experiments, diffusion by such mechanism would exert a large amount of strain energy in the lattice. The markers with smaller atomic size would have lower activation energy and higher diffusivity than the large markers.

2) Interstitial-vacancy pair mechanism

A less strainful mechanism than the conventional interstitial is the diffusion by interstitial-vacancy pair. In this mechanism [6] an impurity sits at an interstitial site surrounded by substitutional solvent atoms and a vacancy as shown in Fig.6.2. This case is favored when a conventional interstitial formation is energetically demanding, so that the jump frequencies for the dissociation of an interstitial-vacancy pair is small. Stated differently, the binding energy between an interstitial and a vacancy in this case is large. Similarly, the jump frequency for the annihilation of the vacancy by a solvent atom that is not the closest neighbor to the interstitial should be very small also, or else the vacancy-interstitial pair would be separated again. However, the jump frequency for the interstitial to hop around the vacancy or for the vacancy to hop around the interstitial atom must be large. In this way vacancy sites are changed without breaking the interstitial-vacancy bond. Between these two types of jumps, the frequency of the interstitial atom's jumps around the vacancy is much larger than that of the vacancy's jumps around the interstitial atom. The limiting and controlling jumps for effective diffusion by interstitial-vacancy pair is then the exchange rate of vacancy and solvent atom that is the closest neighbor to the interstitial atom. In this diffusion process, thus, the diffusivity would be almost independent of the impurity atom's jumps; but it would depend on the solvent atom's jumps. Thus, for ion mixing by this mechanism during radiation-enhanced diffusion, the activation energy would be almost independent of the types of solute atoms for markers. Rather, it would depend almost only on the types of solvent atoms, i.e., the matrix.

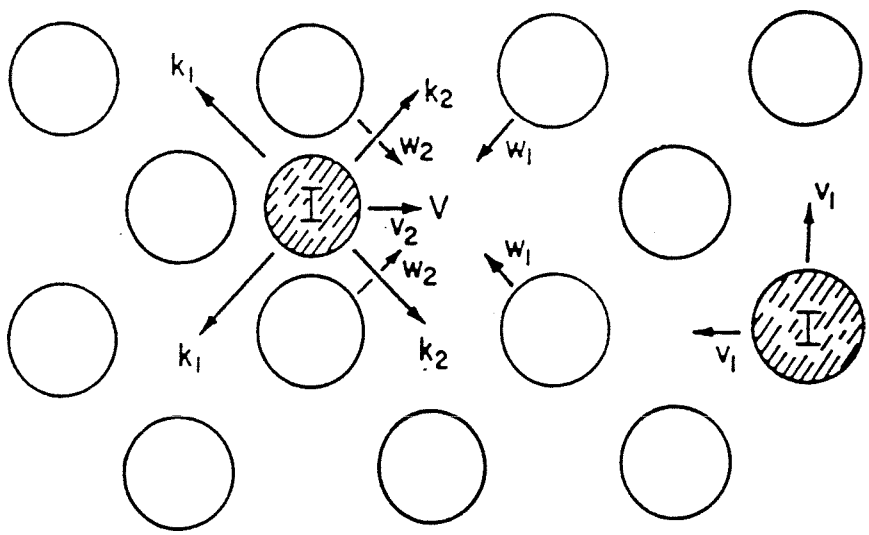

Fig. 6.2. Model of diffusion by interstitial-vacancy pairs. The i-v pairs are created with frequentcy v_i, annihilated with frequency v_2, dissociated by interstitial jumps k_1 and by solvent jumps w_1, and maintained in association by interstitial jumps k_2 and by solvent jumps w_2.

3) Self-interstitial-solute-atom complex or mixed-dumbbell mechanism

The self-interstitial-solute-atom complex, or commonly known also as the mixed-dumbbell, is much more widely studied than the interstitial-vacancy pair [7, 8, 9]. In fcc metals, the most stable self-interstitial configuration is known to be the <100> dumbbell [7, 8]. In bcc metals the <110> dumbbell configuration is stable [9]. These two configurations and their elementary jump mechanisms are shown in Fig. 6.3 and 6.4. In any self-interstitial configuration, a large amount of strain energy is involved since an extra atom is placed into the lattice. If there is a way to decrease such a compressed arrangement, then a defect-complex configuration is likely to form. One such configuration is a self-interstitial-solute-atom-complex, where the solute atom has a smaller atomic size than the host atom. For an oversized solute atom a mixed-dumbbell configration is not likely to form, since it expands the lattice even more.

6.3 Experiments with markers in Zr matrix

We have conducted high temperature ion mixing experiments with markers in a β-Zr matrix. The markers were Ti, Ni, Cu, and Au. These markers can be classified in two different types of solutes in Zr according to their thermal diffusivities. Ni and Cu are known to be the fast diffusers in Zr, i.e., their diffusivities are 6 to 7 orders of magnitude larger than that of Zr self-diffusion at ~1100 K [10]; Ti and Au have diffusivities similar to that of Zr self-diffusion. Under the thermal equilibrium conditions, the markers with small atomic sizes and low valences like Ni and Cu are very likely to diffuse by an interstitial-like mechanism and the markers with large atomic sizes like Ti and Au are likely to diffuse by vacancy mechanism, as described in the previous section. From the investigation of activation energy of mixing under the high temperature irradiation, the likely diffusion mechanisms of these marker systems

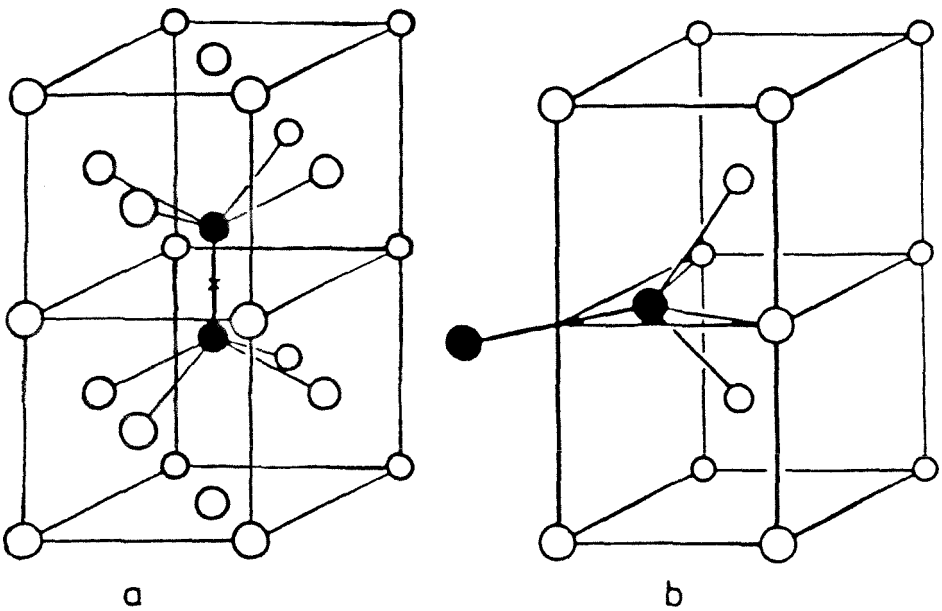

Fig. 6.3. (a) 100-dumbbell in fcc-lattice; (b) 110-dumbbell in bcc-lattice.

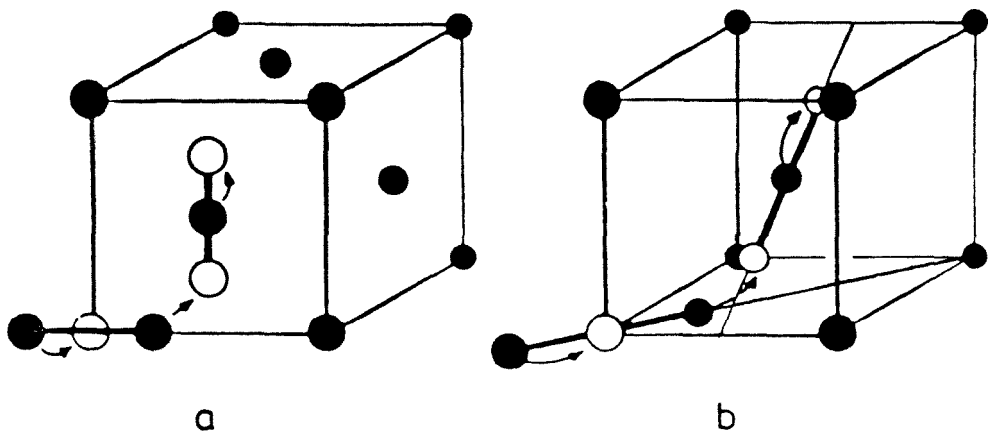

Fig. 6.4. Elementary jumps of (a) 100-dumbbell (fcc); (b) 110-dumbbell (bcc). •: positions before jump; o: positions after jump.

during radiation-enhanced diffusion could be elucidated.

The marker samples were prepared in the same way as for the experiments described in the previous chapters. The experiments were performed using the same accelerator both to induce mixing and to analyze the specimens by backscattering spectrometry. In this way, the specimens could be analyzed at the irradiation temperatures. The irradiations were carried out at 294, 398, 438, 473, 523, 573, and 623 K. Dummy samples were also mounted next to every sample that was irradiated, for all temperatures, to determine the spreading of a marker due to thermal diffusion alone. The fluctuation of the temperature during irradiation was +/- 2 K, as measured by a Pt resistance thermometer that was clamped to the sample holder. The irradiations were conducted with 750 keV Kr^+ ions for a fixed dose of $1X10^{16}/cm^2$. All the irradiated and unirradiated samples, except the ones with Cu marker, were analyzed by in situ 1.8 MeV He^+ Rutherford backscattering spectrometry (RBS) at the temperatures of irradiations. The samples with Cu marker were analyzed with secondary ion mass spectroscopy (SIMS). Within experimental uncertainty all of the marker signals were Gaussian in form before and after the irradiations. Therefore, the signal widths were found by fitting a Gaussian curve to the data by a least-squares routine. The mixing efficiency, $Dt/\emptyset F_D$, for each sample is obtained as described in chapter 2, page 13.

All the samples showed a change of the RBS signal above a certain irradiation temperature that is typically of grain boundary diffusion, i.e., there is a long and flat tail from the marker signal. The markers with small atomic sizes like Ni and Cu showed this effect near 473 K and the ones with large atomic sizes like Ti and Au, at higher temperatures around 573 K. The analysis of the marker signals in the RBS spectra becomes questionable when grain boundary diffusion and ion mixing are superposed. We were, thus, limited to few results for the Ni and Ti samples. Especially for the Ni marker, the effect of grain boundary diffusion was so pronounced that hardly any reliable results were obtained. The most trustworthy results are those of the samples

with Au and Cu markers. Even though the Cu marker showed a significant amount of grain boundary diffusion, the SIMS technique used for the analysis of this sample system facilitated the distinction between the diffusion due to mixing and the grain boundary diffusion.

The ion mixing of these samples clearly depends on irradiation temperatures. The results are shown in Fig.6.5. We only show the results for Cu and Au markers in Zr since they are most reliable. These results are tabulated in Table 6.1 with some other related data that are used to discuss the effects of radiation-enhanced diffusion in ion mixing. The values of the mixing efficiency are very similar for both markers over the whole range of irradiation temperatures. The common activation energy is near 0.5 eV. This activation energy is close to the value of 1/2 vacancy migration enthalpy, H_v^m ,that is predicted by radiation-enhanced diffusion theory. In Zr, H_v^m is observed to be near 0.7 eV from various experiments and 1.4 to 1.6 eV from physical parameter correlations [11]. Thus, we can safely assume that the vacancy migration enthalpy is around 1.1 eV +/- 0.4 eV. Then the activation energy observed in the present experiment is thus in the range of 0.3 to 0.7 of vacancy migration enthalpy of Zr. Since the activation energy is essentially the migration enthalpy of diffusing species and the experimental value observed here is the fraction of vacancy migration enthalpy, some of the fast diffusion mechanisms described in the previous section are considered as the possible mechanisms that could have contributed to such low activation energy values during radiation-enhanced diffusion. Even though we have not considered grain-boundary diffusion mechanism, we cannot completely ignore such mechanism in more detailed analysis.

The migration enthalpy of a conventional interstitial mechanism is significantly lower than the vacancy migration enthalpy, and the solutes that diffuse by this mechanism are typically smaller than the solvent atoms. Even though the migration enthalpy observed in the present radiation-enhanced diffusion experiment is only a

fraction of the vacancy migration enthalpy, the atomic sizes of the markers are too large for this mechanism (See Table 6.1). If this mechanism contributes to diffusion in our experiment, then the activation energy for the Cu marker should be smaller than that of the Au marker, since Cu has a smaller atomic size than Au and should thus diffuse faster by this mechanism than Au. However, we observe the same activation energy for both markers. We thus conclude from these observations that the conventional interstitial mechanism is unlikely to contribute dominantly to diffusion in the present experiment.

Diffusion by the interstitial-vacancy pair mechanism is mainly controlled by the vacancy migration, as described in the previous section. Thus, the migration enthalpy is mainly that of the vacancy, regardless of the solute types. If this interstitial-vacancy pair mechanism controls the diffusion in our experiment, the observed activation energy should be similar for Cu and Au. This is indeed so. The migration enthalpy for thermal diffusion by this mechanism should be only little less than that of the thermal vacancy migration enthalpy [12]. The experiment yields an activation energy that is indeed only a fraction of the thermal vacancy migration enthalpy. We can thus conclude that the interstitial-vacancy pair mechanism could be important in our experiment.

Lastly we consider the mixed-dumbbell mechanism. This mechanism is believed to contribute to solute segregation in metals under irradiation at high temperatures [13, 14]. There are formulae by which the migration enthalpy of this mechanism, H_{md}^{m}, [13, 15] can be estimated for fcc metals. Even though Zr target that is investigated in the present experiment is of bcc phase, the magnitude of migration enthalpies of mixed-dumbbells in fcc and bcc metals are similar [14]. Thus the following simple equation of zeroth order that estimates <100> dumbbell migration enthapy in fcc metal [15],

Table 6.1. Compilation of data on solutes in Zr. Q_{red} is the activation energy of radiation-enhanced diffusion that is observed in the present experiment, H_v^m is the vacancy migration enthalpy, r is the Pauling's radii, and H_i^m is the self-dumbbell migration enthalpy.

	Cu	Au	Zr	References
Q_{red}	~0.5 eV	~0.5 eV	-	present experiment
H_v^m	-	-	0.7 or 1.4 - 1.6 eV	[11]
H_i^m	-	-	0.26 - 0.3 eV	[16, 17]
r	1.28 Å	1.44 Å	1.58 Å	[20]

$$H^{m}_{md'} \approx H^{m}_{i} + 3/5\, H^{b}_{md}, \qquad (8)$$

can also be used to approximate the migration enthalpies of mixed-dumbbells in bcc metals. In that equation, H^{m}_{i} is the migration enthalpy of solvent atoms by self-dumbbell mechanism and H^{b}_{md} is the binding energy of the solute and solvent interstitials in the mixed-dumbbell configuration. H^{m}_{i} of Zr is about 0.26 to 0.3 eV [16, 17]. H^{b}_{md} can be approximated from computer simulations based on interaction potentials [18]. The H^{b}_{md} values studied from various types of alloys so far are within 0.3 to 0.88 eV. Thus, using this range of values we can roughly estimate the range of H^{m}_{md} for solutes in Zr to be between 0.5 to 0.8 eV. These values are below the vacancy migration enthalpy and are agreeable with the present experimental data. The principal factor differentiating the migration enthalpy for different types of solutes would be the different binding energies of mixed-dumbbells. Since only a fraction of this difference enters in the migration enthalpy, different solutes should have similar migration enthalpies for a given solvent. All these arguments are consistent with our observed facts and make the mixed-dumbbell mechanism another possible candidate for diffusion in our experiment. It has also been reported previously that when Zr crystal with 0.2-0.3 at. % Au is irradiated by 2 MeV He, the resultant defect-solute atom configuration was mixed-dumbbells [18].

The similar mixing efficiencies we observe for both Cu and Au in β-Zr can thus be explained by two diffusion mechanisms: that of the mixed-dumbbell, and that of the interstitial-vacancy pair. This conclusion ignores complications that arise when sinks are present that can trap the migrating defect.

Let us consider specifically the mixed-dumbbell mechanism first. Mixed-dumbbells can condense and sublimate at interstitial sinks, such as dislocation loops or vacancies. When the mean free transport distance of the moving defects is larger than the mean sink separation, the solute transport can be limited by the sinks. That

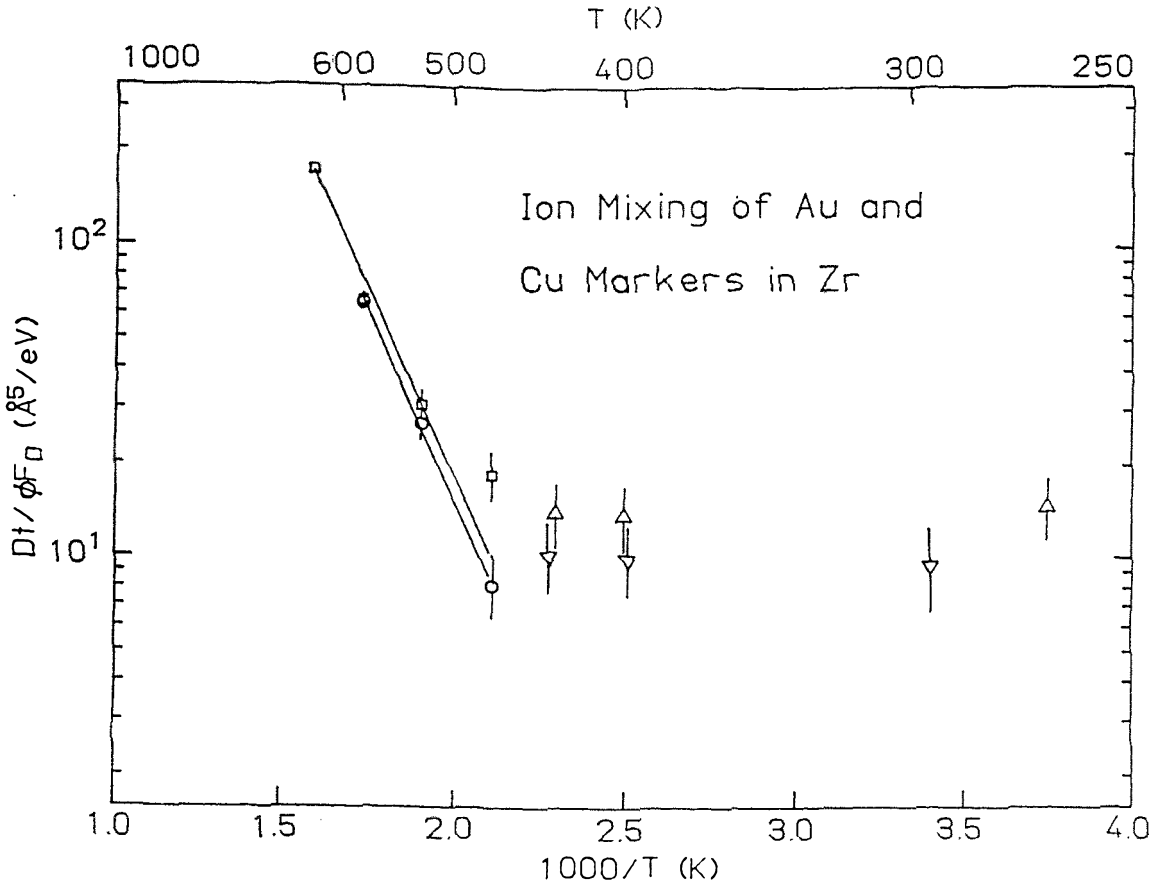

Fig. 6.5. Ion mixing efficiencies as a function of irradiation temperatures. "□" and "Δ" symbols represent the data points for ion mixing of Au marker in Zr. "O" and "∇" symbols are that of Cu markers in Zr. Data points with "□" and "O" symbols are least-square fitted by a straight line to obtain the activation energy of ion mixing during radiation-enhanced diffusion process. The data points with "Δ" and "∇" symbols are in the temperature independent regime of ion mixing.

condition typically prevails in radiation-enhanced diffusion experiments [19]. In that case, the measured diffusion coefficient, or the mixing efficiency in our present experiment, will be smaller than the actual diffusion coefficient, or the actual mixing efficiency. The measured mixing efficiency then is

$$Dt/\emptyset F_{D\ meas.} = Dt/\emptyset F_{D\ actual}\ C_m/C_t, \tag{7}$$

where C_m and C_t are the mobile (or untrapped) and total solute (untrapped and trapped solutes by sinks) concentration, respectively. We consider two cases: strong and weak coupling of the interstitial to the solute. For a mixed-dumbbell with strong coupling, most of the solutes are segregated at sinks along with the solvent interstitial and the $Dt/\emptyset F_{D\ meas.}$ is the actual mixing efficiency multiplied by the ratio of release rate of segregated atoms from the sinks to arriving rate of mobile solutes to the sinks and the sink concentration[19]. Thus, the measured mixing efficiency would basically represent the release rate of solutes from sinks and sink concentrations. For the case of weak coupling, only a fraction of the solutes are segregated, thus the measured mixing efficiency or diffusion coefficient is affected less by the ratio C_m/C_t than the strong coupling case. Therefore, the mixing efficiencies of markers in a radiation-enhanced diffusion experiment do not necessarily correspond to the actual diffusion coefficients of these markers. An analogous argument can be also applied to the diffusion mechanism by interstitial-vacancy pair. The types of sinks and their interaction with interstitial-vacancy pair would be, however, different from the mixed-dumbbell case. The similar mixing results observed here can be thus explained by the complex diffusion and interaction mechanisms of mixed-dumbbells with its sinks.

This chapter summarizes those aspects of radiation-enhanced diffusion that are relevant to the mixing experiments performed with Ni, Ti, Cu and Au in β-Zr. The three mechanisms that are responsible for fast thermal diffusion are considered in detail

and compared with the experimentally observed diffusion results of Cu and Au markers in Zr by ion mixing. The activation energy during radiation-enhanced diffusion for both marker systems was ~0.5 eV, which is the 1/2 of vacancy migration enthalpy of self-diffusion in Zr. This value agrees well with the prediction from radiation-enhanced diffusion theory. The magnitude of mixing efficiencies for Cu and Au markers in Zr were also similar. The observed experimental results seem to indicate that mixed-dumbbells or intertitial-vacancy pair diffusion mechanisms are contributing to atomic displacements and that the interactions of diffusing defects with their sinks should be considered for radiation-enhanced diffusion experiments.

6.4 References

[1] D. Acker, M. Beyer, G. Brebec, M. Bendazzoli, and J. Gilvert, J. Nucl. Mater., 50 (1974) 281.

[2] G.J. Dienes, and A.C. Damask, J. Appl. Phys., 29 (1958) 1713.

[3] Y.-T. Cheng, X.-A. Zhao, T. Banwell, T.W. Workman, M-A. Nicolet, and W.L. Johnson, J. Appl. Phys., 60 (1986) 2615.

[4] A. Antilla, and M. Hautala, Appl. Phys., 19 (1979) 199.

[5] W.K. Warburton and D. Turnbull, Diffusion in Solids, Eds. A.S. Nowick and J.J. Burton (Academic Press, New York, 1975), p. 171.

[6] J.W. Miller, Phys. Rev. 188 (1969) 1074.

[7] K.H. Robrock, Phase Stability and Solute Redistribution, Eds. F. Nolfi and J. Giottus (Appl. Sci. Publ., London) p.115.

[8] P.H. Dederichs, C. Lehmann, H.R. Schober, A. Scholz, and R. Zeller, J. Nucl. Mater. 69&70 (1978) 176.

[9] F.W. Young, Jr., J. Nucl. Mater. 69&70 (1978) 310.

[10] G.M. Hood and R.J. Schultz, Acta Metal. 22 (1974) 459.

[11] G.M. Hood, J. Nucl. Mater., 139 (1986) 179.

[12] R.A. Johnson, and N.Q. Lam, J. Nucl. Mater. 69&70 (1978) 424.

[13] R.A. Johnson, and N.Q. Lam, Phys. Rev. B, 13 (1976) 4364.

[14] W. Wagner, L.E. Rehn, H. Wiedersich, and V. Naundorf, Phys. Rev. B, 28 (1983) 6780.

[15] A. Bartels, F. Dworschak, H.P. Meurer, C. Abromeit, and H. Wollenberger, J. Nucl. Mater. 83 (1979) 24.

[16] H.H. Neely, Rad. Eff. 3 (1970) 189.

[17] R. Pichon, E. Bisogni, and P. Moser, Rad. Eff. 20 (1973) 159.

[18] L.M. Howe, M.L. Swanson, and A.F. Quenneville, J. Nucl. Mater. 69&70 (1978) 744.

[19] V. Naundorf, M.P. Nacht, H.J. Gudladt, and H. Wollenberger, Proceedings of Yamada Conference, (1981).

[20] G.M. Hood, J. Phys. F: Metal Phys., 8 (1978) 1677.

Chapter 7

RADIATION-ENHANCED DIFFUSION; DEFECT CREATION RATE AND KINETICS

7.1 Diffusion and interface limited process in compound formation

The phenomena of formation of metal silicides at a metal-silicon interface by furnace annealing and by heavy ion irradiation in the thermally activated regime show many similarities [1]. In both cases, the same silicide phases form, the moving species are often the same during the silicide formation. Also silicides whose thickness grows proportionally to the linear or square root of time upon thermal annealing form proportionally to the linear or square root of the ion irradiation dose. Evidently, the basic processes that control the formation of silicides by furnace annealing also control the formation of silicides by ion mixing. In the present chapter, we study the defect creation rate in the radiation-enhanced diffusion theory by investigating its effects in the growth of silicide by ion mixing.

There are three main mechanisms that control the compound growth [2] : (1) the release of moving species atoms from the surface; (2) diffusion of the moving species through the silicide layer; and (3) the interface reaction that forms new silicide. The rate of release of surface atoms is usually very large, thus the growth rate is mainly controlled by the remaining two mechanisms. Of the other two mechanisms, the one which controls the growth rate of the silicide can be determined from the dependence of the silicide thickness on the diffusivity, D, and the interfacial reaction rate, K. A characteristic changeover thickness, X*, [3] can be defined as:

$$X^* = D/K. \qquad (1)$$

For the growth thickness X<<X*, the growth rate is limited by the interface reaction rate, and when X>>X*, the growth is limited by the diffusion rate, which depends on the diffusion mechanism. Growth of most silicides is limited by the diffusion rate (small D/K), characterized by a thickness of the compound layer that increases as the square root of annealing time or irradiation dose. However, $CrSi_2$ has been reported [4, 5, 6] to grow linearly with ion dose or thermal annealing duration. Thus, the kinetics of $CrSi_2$ formation is limited by the interface reaction rate.

The question we address is: Is it possible to modify the growth rate of $CrSi_2$ by experimentally disturbing the diffusivity or the interface reaction rate during its growth?

The strategy we follow consists of irradiating the Cr/Si interface with a constant dose at various dose rates and damage energies. Thus, from radiation-enhanced diffusion theory, we would be modifying the diffusivity of the moving species during $CrSi_2$ formation or could be possibly modifying the growth mechanism.

7.2 Experiments in $CrSi_2$ formation

The $CrSi_2$ samples were prepared on thick SiO_2 layers grown on a Si wafer by thermal oxidation. 2530 Å Si, 350 Å Cr, and 50 Å Si were sequentially e-gun evaporated at a pressure better than $3X10^{-7}$ Torr. The 50 Å Si cap was used to inhibit oxidation of the Cr layer. Irradiations were performed with 265 and 530 keV Xe for doses from 5 to $23X10^{15}/cm^2$. The ion dose rate was varied from 3.1 to $124X10^{11}$ $Xe/cm^2 \cdot s$, giving a factor 40 difference in dose rate from the lowest to highest rate. The measured sample temperature was held at 500+/-3 K during irradiation. A dummy specimen was also loaded together with the samples to be irradiated to test for thermally induced growth of $CrSi_2$. Hardly any formation $CrSi_2$ was observed for up to 24 hours of annealing at this temperature. After the irradiations were completed, the

specimens were cooled to room temperature and analyzed by 1.9 and 2.0 MeV He backscattering spectrometry to measure the thicknesses and compositions of the films. An X-ray diffractometer was also used to confirm the presence of the $CrSi_2$ phase after irradiation.

Fig. 7.1a shows the backscattering spectrum of as-deposited sample. Fig. 7.1b shows the spectrum of a dummy sample that was kept next to the irradiated samples at 500 K. Even after 24 hours of annealing, the amount of $CrSi_2$ formed is negligible compared to the amount formed by ion mixing. Fig. 7.1c and d show the spectra of the samples after irradiation of 265 keV Xe for doses of 1.18 and $1.12 \times 10^{16}/cm^2$, respectively. The sample of Fig. 7.1c was irradiated at high dose rate (7.5×10^{12} $Xe/cm^2 \cdot s$) and that of Fig. 7.1d at 24 times lower dose rate (3.1×10^{11} $Xe/cm^2 \cdot s$). The unusual profile of the Xe signal in the spectra for the implanted samples results from Xe bubbles at the $Si/CrSi_2$ interface [7]. The area of the Xe signal in both spectra is almost the same, confirming that both samples received the same dose of Xe.

Comparing Fig. 7.1c and d, we see that a low dose rate produces a thicker $CrSi_2$ film than at high dose rate. A similar trend is observed for other samples irradiated with different doses. The results are plotted in Fig. 7.2 for 530 keV Xe^{++} and Fig. 7.3 for 265 keV Xe^{+} irradiation at 500 K. Clearly, thicker layers of $CrSi_2$ always form at lower dose rates. In Fig. 7.2, the dose rates differ by a factor of 8 and in Fig. 7.3 by a factor of 24. Hence, the difference in the thickness of $CrSi_2$ increases with the ratio of the dose rates. The average damage energy from a Monte Carlo computer simulation [8], F_D, deposited at the Si/Cr interface is larger for the 265 keV irradiation (490 eV/Å) than for the 530 keV irradiation (320 eV/Å). This difference is reflected in Fig. 7.2 and 7.3 in that for the same dose of 6×10^{15} Xe/cm^2 and for the same low dose rate, the 265 keV irradiation generates a thicker $CrSi_2$ layer (540 Å) than the 530 keV irradiation (450 Å).

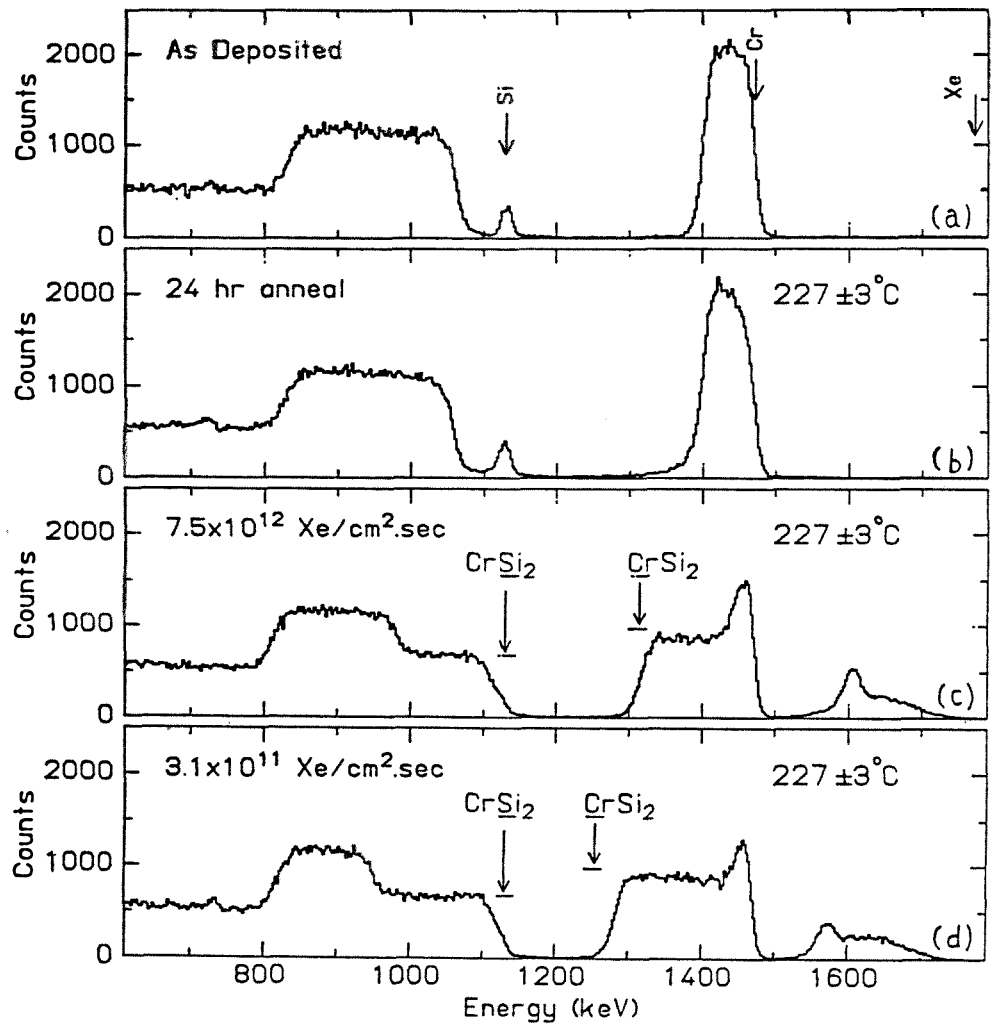

Fig. 7.1. Backscattering spectra showing the formation of $CrSi_2$ by 265 keV irradiation at 500 K.

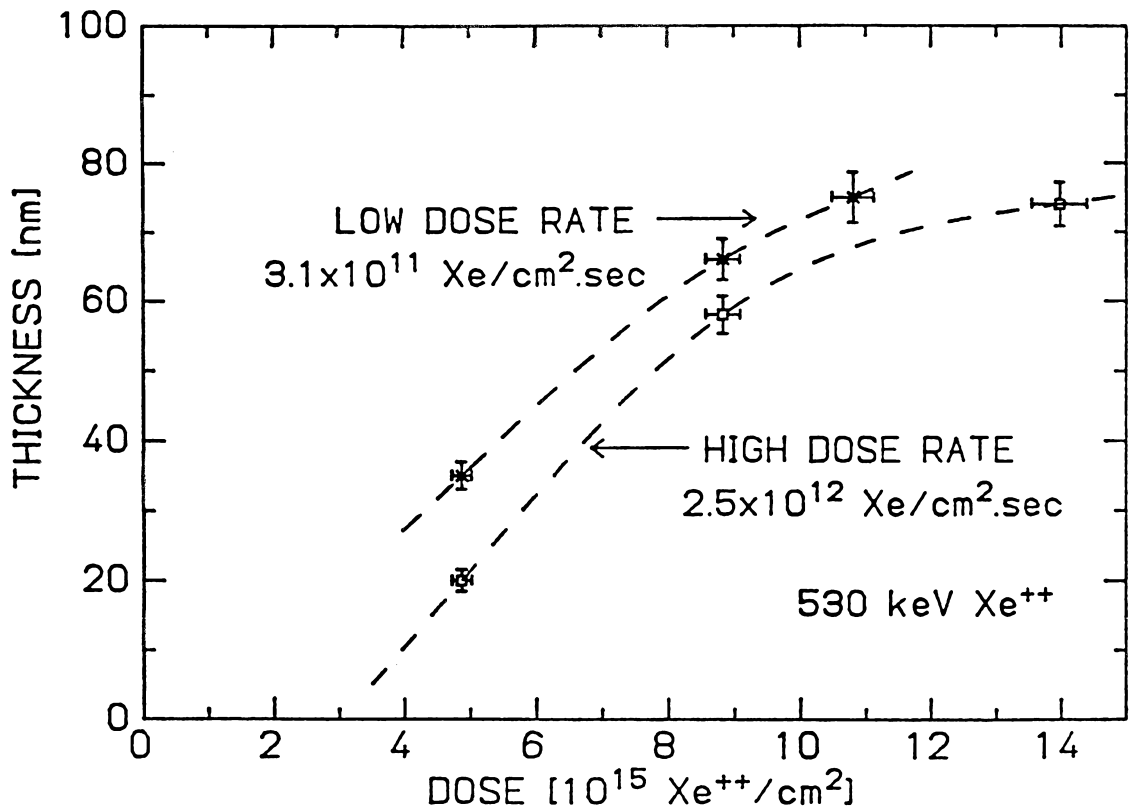

Fig. 7.2. Thickness of $CrSi_2$ as a function of 530 keV Xe^{++} irradiation dose at 500 K.

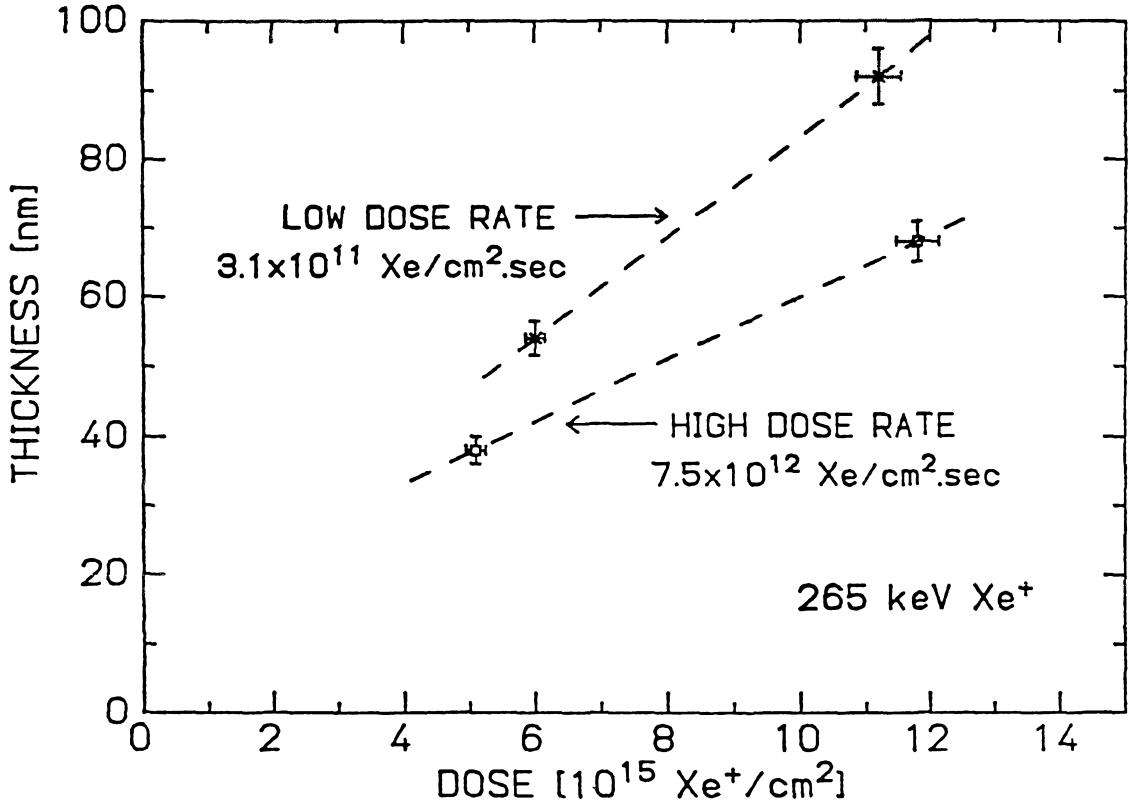

Fig. 7.3. Thickness of $CrSi_2$ as a function of 265 keV Xe^{++} irradiation dose at 500 K.

In Fig. 7.4 we show the thickness of $CrSi_2$ versus defect creation rate for 1842 seconds of irradiation for all the Xe irradiations conducted in the present experiment at 500 K. The defect creation rate, K, (dpa/sec, displacements per atom per second) is calculated from the Kinchin-Pease [9] formula;

$$K=\frac{0.4}{NE_d}\frac{d\Phi}{dt}F_D \qquad (2)$$

where N is the atomic density, E_d is the displacement energy, $d\Phi/dt$ is the flux of bombarding particles, and F_D is the average damage energy deposited into the target per unit path length of the projectile. The defect creation rate was calculated for a Cr film at a depth near the $Cr/CrSi_2$ interface. The parameters in equation 2 are for Cr, i.e., E_d is assumed 18 eV (which is displacement energy for Cr atoms) [10]. F_D is a (weak) function of the Cr layer thickness since the position of the interface changes during the irradiation. We therefore calculated the average F_D for each irradiation.

We observe that the amount of $CrSi_2$ that forms strongly depends on the rate at which defects are created up to $6.6X10^{-2}$ dpa/s. Beyond this point, the dependence is weak.

This experimental observation can be explained within the frame of radiation-enhanced diffusion theory. For the discussion, we will point out some of the salient features of the theory already discussed in chapter 6.

The changes induced in a system by ion irradiation depend on dose rate if there is an interaction between the effects of cascades created by individual incident ions. Cascades create defects. These defects are responsible for atomic diffusion in the radiation-enhanced diffusion regime. A dose rate arises when the defects interact with one another (recombination regime). However, if the defects are annihilated at a constant density of fixed sinks before interacting with each other, no correlation between these defects and dose rate effect can occur.

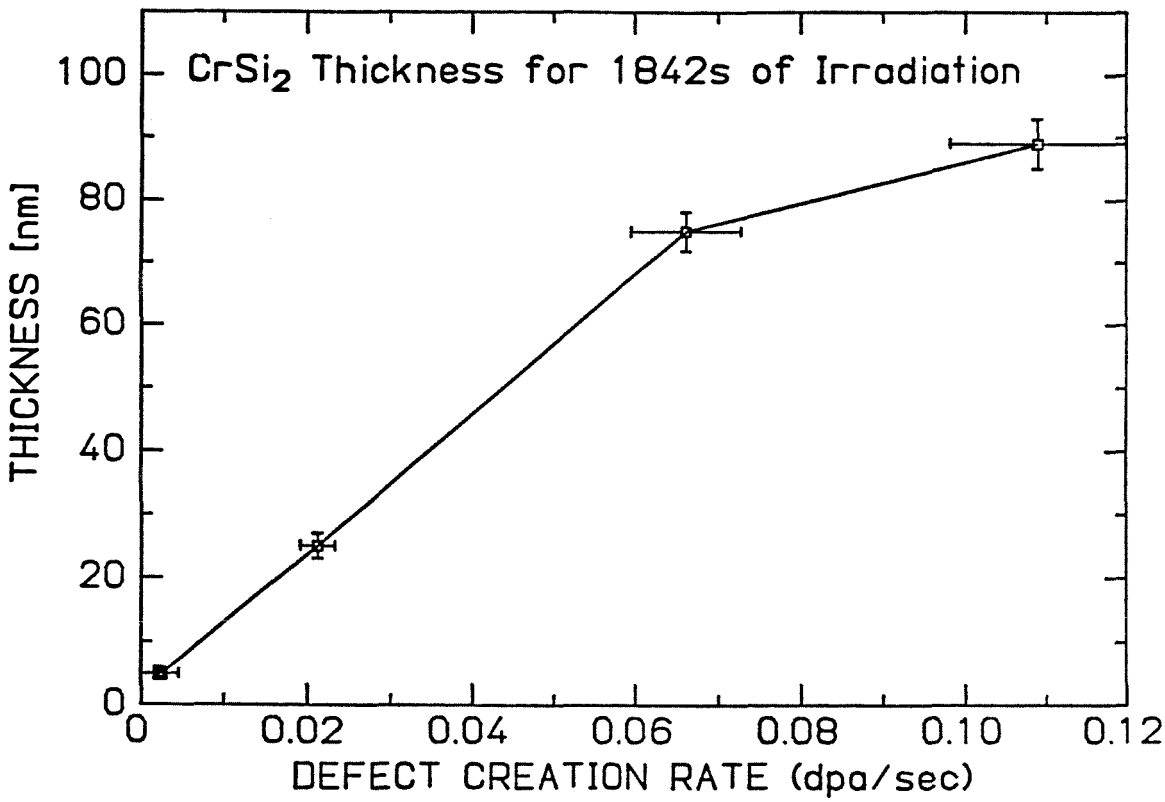

Fig. 7.4. Thickness of $CrSi_2$ as a function of defect creation rate for 1842 seconds of Xe irradiation.

The dependence of growth of a film on dose rate and induced by the mobility of defects that are created by ion irradiation can be approximated as [11]

$$X \sim \Phi^{1/2}/(d\Phi/dt)^{1/4}, \quad (3)$$

where X is the thickness of the film grown by irradiation, Φ is the dose given to the target and $d\Phi/dt$ is the dose rate.

Equation 3 is valid for a system that grows by a diffusion-limited process. It has been shown previously that equation 3 is qualitatively correct for a system where the compounds grow by a diffusion limited process [11]. In the case of $CrSi_2$ where the growth is interface-limited, we interpret the present experimental results as follows. Typical dose rates of previous ion mixing studies were on the order of 10^{13} Xe/cm^2·s. At this dose rate, the diffusivity in the mixed region is high enough for the growth process to be controlled by the interface reaction rate. As long as these conditions prevail, no dose rate effect is expected. If, however diffusive flux becomes smaller than the interface reaction rate, dose rate effects on the growth should be observed in a way described by equation 3, and evidenced by the experimental results of Fig. 7.4. The critical defect creation rate at 500 K is near 0.08 dpa/s. There are two other possible explanations for the present experimental observersation besides the above, where the dose rate is assumed to affect strongly on diffusivity rather than the interface reaction rate. Both diffusivity and the interface reaction rate are assumed to be affected similarly on dose rate, and the dose rate is assumed to affect more strongly on the interface reaction rate than the diffusivity. All these cases have been discussed in detail in ref. 12. From that, the explanation that is given here seems to best suit in interpreting the present experimental results.

From this experiment we have shown the effects of dose rate during radiation-enhanced diffusion. The results demonstrate that growth mechanism by ion mixing

can be modified by adjusting some of the irradiation parameters such as dose rate and damage energy. It is also expected that the growth of all compounds by ion mixing will be dose rate dependent as described by radiation-enhanced diffusion theory.

7.3 References

[1] M-A. Nicolet and S.S. Lau in N.G. Einspruch and G.B. Larrabee (Eds.), VLSI Electronics-Microstructure Science, Vol. 6, (Academic Press, New York, 1983).

[2] A.S. Grove, Physics and Technology of Semiconductor Devices (John Wiley & Sons, Inc., New York, 1967).

[3] U. Gosele and K.N. Tu, J. Appl. Phys. 53 (1982) 3252.

[4] U. Shreter, Frank C.T. So, and M-A. Nicolet, J. Appl. Phys. 55 (1984) 3500.

[5] J.O. Olowolafe, M-A. Nicolet, and J.W. Mayer, J. Appl. Phys. 47 (1976) 5182.

[6] M. Natan and S.W. Duncan, Thin Solid Films 123 (1985) 69.

[7] B.Y. Tsaur, Z.L. Liau, and J.W. Mayer, J. Appl. Phys. 47 (1976) 5182.

[8] J. Biersack and L.G. Haggmark, Nucl. Instr. and Meth. 174 (1980) 257.

[9] G.H. Kinchin and R.S. Pease, Rep. Prog. Phys. 18 (1955) 1.

[10] H.H. Andersen, Appl. Phys. 18 (1955) 131.

[11] T. Banwell, M-A. Nicolet, R.S. Averback, and L.J. Thompson, Appl. Phys. Lett. 48 (1986) 1519.

[12] S.-J. Kim, D.N. Jamieson, M-A. Nicolet, and R.S. Averback, Mat. Res. Soc. Symp. Proc. Vol. 93, (1987) p. 233.

Chapter 8

FINAL REMARKS OF PART I; ION-SOLID INTERACTIONS

8.1 Summary

A) Low temperature regime

How ion mixing mechanisms at low temperature, namely collisional mixing and thermal spike, influence atomic displacements depends on various target matrix properties. For the matrices with high cohesive energy and small damage energy, the collisional processes dominate. For matrices with high damage energy density and low cohesive energy, thermal spike processes dominate. The effect of collisional mixing was hard to observe with the energies, types of ions, and choices of targets used for the present investigations. The experimental results with markers in Ge were in discord with the predictions made from the collisional theory [ch. 2]. The test of the effects of the kinematic factor in ion mixing with various markers in Cu, Mo and Ru matrices showed that collisional mixing is a secondary effect in ion mixing [ch. 2]. On the other hand, we have seen that the mixing efficiencies of various matrices depend strongly on the damage energy in the cascade and (inversely) on the cohesive energy of the matrices, which is a manifestation of thermal spike mechanism in ion mixing [ch. 3].

The dependence of thermal spike mixing on markers' properties were also investigated. Thermal diffusivity of the markers correlates with the mixing efficiency, implying that the atoms are displaced by a thermally activated process [ch. 4]. We have also evidence that vacancy-related mechanisms predominate to diffusion during a thermal spike, and this is in agreement with the results obtained from the molecular dynamics calculations from the literature [ch. 3 , 4].

In an ideal dilute marker system, the heat of mixing should negligibly affect mixing efficiencies. We have systematically investigated this issue and found no correlation between the heat of mixing and the observed ion mixing efficiencies [ch. 5]. This result ascertains the validity of the marker systems that we have used in our experiment; it also rectifies a previous report that the effect is not negligible.

B) High temperature regime

In the radiation-enhanced diffusion regime during high temperature irradiations, there are three parameters that govern the way atoms are transported and the amount they diffuse. These parameters are the correlation factors, the activation energy, and the defect creation rate. The first parameter is examined in refs. 1 and 2. We have examined the last two paremeters. By doing experiments with various types of solutes in Al[1] and Zr[2], the correlation factors were investigated. It is found that in radiation-enhanced diffusion regime, mixing takes place by an interstitial-related mechanisms, unlike in thermal spike regime, where vacancy-related mechanisms mainly contribute to diffusion. The activation energy for the radiation-enhanced diffusion mechanism was found to be a fraction of thermal vacancy migration enthalpy, suggesting that the migration during radiation-enhanced diffusion occurs by some kind of fast diffusion process that is likely to involve interstitials [ch. 6].

The effect of defects creation rate on compound formation during radiation-enhanced diffusion regime was also studied [ch. 7]. The growth of an interfacial compound layer can be limited by diffusion or by interfacial reaction in conventional thermal annealing. The mechanisms that control the compound growth can be manipulated by irradiation. We have conducted such experiments and showed that the growth of a $CrSi_2$ layer at a Si/Cr interface induced by irradiation is a function of the dose rate. The result can be understood on the basis of radiation-enhanced diffusion theory and the known, particular, properties of the Cr/Si system.

8.2 Conclusions

The two principal conclusions that we deduce from our various investigations are that the thermal spike model of ion mixing is consistent with our low temperature results of marker spreading; and that at elevated temperature, the mechanisms of radiation-enhanced diffusion dominate and they, too, can offer adequate explanations of our results.

We have attempted to identify the mechanisms that are responsible for the mixing. Definitive statements cannot be made, because the experiments necessarily provide only indirect evidence for mechanisms. It can be stated nonetheless that in the thermal spike regime, vacancy-like mechanisms are dominant, while in the radiation-enhanced diffusion regime, interstitial mechanisms prevail.

These conclusions are derived from experiments in which the spreading of markers is studied while systematically varying specific properties of the systems. This approach has been applied also for bilayer experiments [3] and has proven to be a most effective way to investigate a phenomenon that is, by itself, too remote in time and microscopic in space to be seen and studied directly.

8.3 References

[1] D. Acker, M. Beyeler, G. Brebec, M. Bendazzoli, and J. Gilbert, J. Nucl. Mater. 50 (1974) 281.

[2] S.-J. Kim, M-A. Nicolet, and R.S. Averback, Mat. Res. Soc. Symp. Proc. Vol. 74 (1987) p.437.

[3] Y.-T. Cheng, T.W. Workman, M-A. Nicolet, and W.L. Johnson, Mat. Res. Soc. Symp. Proc. Vol. 74 (1987) p.419.

PART II. OXIDATION PHENOMENA IN SILICIDES AND ALUMINIDES

Chapter 9

OXIDATION OF $CoSi_2$

9.1 Silicides and metals as interconnects in VLSI

As the density of silicon integrated circuits increases, the width of interconnection lines shrinks, but their total length on a chip grows. As a result, the line resistance increases. It is thus very important to use low resistivity material for interconnection lines in integrated circuits. Metal silicides have been studied extensively as possible materials for interconnection lines, because their electrical resistivity is much lower than that of doped polycrystalline silicon and because they are compatible with present IC processing technology. However, their electrical resistivity is still about one order of magnitude greater than that of good elemental conductors. Metals are thus even more attractive interconnection lines than silicides.

In practice, interconnection lines have to be isolated. It has been shown [1, 2] that Ni and Co lines with an SiO_2 coating can be formed by thermally oxidizing $NiSi_2$ and $CoSi_2$ on SiO_2 substrates. During oxidation, the Si in the silicide film is converted to an outer insulating layer of SiO_2. Simultaneously, the silicide transforms into a metal layer surrounded by SiO_2. However, during this oxidation process the film becomes morphologically unstable as it turns increasingly metal-rich. In the end, the film becomes discontinuous and is incapable of transporting electrical current. In this chapter, we present the investigation on several aspects of the wet oxidation of $CoSi_2$ film. Our results apply to both wet and dry oxidation.

9.2 Experiments with $CoSi_2$

In this experiment, we have measured the resistance and Hall effects of the $CoSi_2$ layer taken at increasing intervals of time during the oxidation process. We next investigate the changes that are induced in a film as a result of heat treatment alone (i.e., in the absence of oxidation). In the subsequent study, we investigate changes that occur when oxidation takes place but without changing film composition. Finally, we examine whether ion irradiation can suppress the morphological instability of $CoSi_2$ film during oxidation.

For this study, the substrates with a thick SiO_2 layer (> 5000 Å) were prepared by 900° C steam oxidation of polished <111> Si wafers. Silicon and Cobalt layers were deposited by e-beam evaporation in a oil-free vacuum system at a pressure of $<10^{-7}$ torr. $CoSi_2$ was grown by vacuum thermal annealing at 650° C. 5 μ-wide $CoSi_2$ interconnection lines were also made on some SiO_2 samples using standard photolithographic techniques. Thermal annealing studies were conducted in a quartz tube vacuum furnace (pressure of $<7x10^{-7}$). Irradiations were performed at room temperature with 210 keV Kr^{++} at doses from $3\text{-}8x10^{15}$ Kr/cm^2 and a pressure of $<10^{-6}$ torr. Wet oxidation (O_2 bubbled through 95° C H_2O) were carried out at temperatures of 750° C and 1000° C. Analyses were performed with 2 MeV $^4He^+$ Rutherford Backscattering Spectrometry (RBS), optical microscopy, SEM with EDAX, TEM, and electrical measurements. For these latter measurements, the grown SiO_2 layer was etched off with a solution of $HF:H_2O$ (1:6). The electrical characterization was done at room temperature using a van der Pauw technique to determine the sheet resistance and Hall coefficient.

9.2a Chemical and electrical changes of $CoSi_2$ film on SiO_2 during oxidation

As Si from $CoSi_2$ on a SiO_2 substrate is depleted to a SiO_2 layer through thermal oxidation at 750° C, the $CoSi_2$ transfroms into CoSi, then Co_2Si, and finally to Co. In the binary phase diagram of the Co-Si system, CoSi and Co_2Si are the only stable compounds existing besides $CoSi_2$ below 1170° C[3]. We can see this change induced by oxidation of $CoSi_2$ from Fig. 9.1a, where we plot the sheet resistance of a film and the carrier type versus η (solid line), the ratio of Si atoms in the grown SiO_2 to the Si atoms originally present in $CoSi_2$. In this instance, the initial composition of the film was very near that of pure $CoSi_2$. Two calculated curves that correspond to two simple limiting cases are also plotted (heavy dashed and dotted lines) for comparison. Both models assume that the total amount of metal in the film is constant (i.e., Co does not oxidize). As Si is depleted from the silicides, one model assumes that they develop a bilayered structure of two adjacent silicides in the phase diagram ($CoSi_2$ and CoSi, CoSi and Co_2Si, Co_2Si and Co). A schematic representation of the cross section of the film during this assumed evolution is shown in Fig. 9.1b. To calculate the thicknesses of the sublayers that are plotted there, the atomic densities listed in Ref. 4 were used. By representing the two sublayers as parallel resistors whose resistivity values were taken from Ref. 5 for the silicides and for cobalt, the sheet resistance indicated by the heavy dashed line in Fig. 9.1a is obtained. The other model assumes that the sublayers are connected in series (heavy dotted line). Both models reproduce the overall trend of the measured sheet resistance fairly, but it is clearly not possible to conclude from these measurements what the morphological make-up of the film actually is. Both models predict the correct carrier type when a single phase is expected. That latter observation strongly supports the idea that the silicide layer undergoes chemical changes, because Co and CoSi are electron conductors and Co_2Si and $CoSi_2$ are hole conductors [5].

Fig. 9.1. (a) Sheet resistance, R_s, and the Si/Co atomic ratio in the Co-silicide as a function of η, the ratio of Si atoms in the SiO_2 to the Si atoms originally present in $CoSi_2$. The solid line connects experimental data results. The carrier type obtained from the Hall coefficient is indicated as 'e' for electrons and 'h' for holes. The heavy dashed and dotted lines are calculated from the model discussed in the text. The oxidation was performed in wet O_2 at 750° C and ambient pressure. The upper abscissa gives the measured amount of grown SiO_2. The light dashed lines indicate the correspondence between the abscissa of Figs 9.1b and 9.1a and the right-hand coordinate of Fig. 9.1a. The point e* was measured after the film broke up into islands. It does not measure the R_s of the film, but of the shorted substrate.

(b) A two dimensional cross-sectional model of the film (parallel resistors) of $CoSi_2$ as converted to Co during oxidation. The ordinate axis represents the thicknesses of the layers.

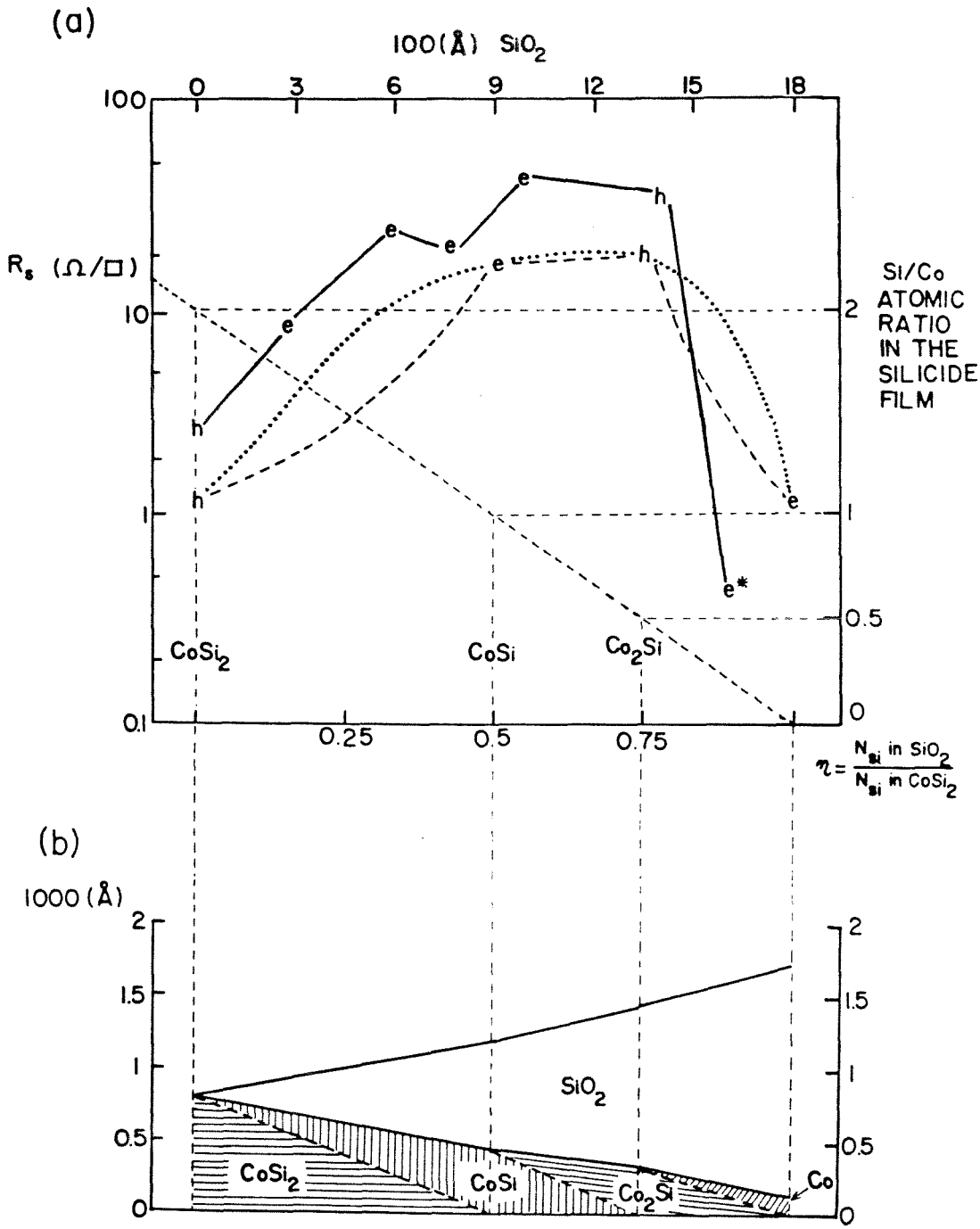
(a)
100(Å) SiO2
0
3
6
9
12
15
18
100
10
1
0.1
Rs (Ω/□)
e
h
e*
CoSi2
CoSi
Co2Si
0.25
0.5
0.75
2
1
0.5
0
Si/Co ATOMIC RATIO IN THE SILICIDE FILM
η = N_Si in SiO2 / N_Si in CoSi2
(b)
1000 (Å)
2
1.5
1
0.5
0
SiO2
CoSi2
CoSi
Co2Si
Co

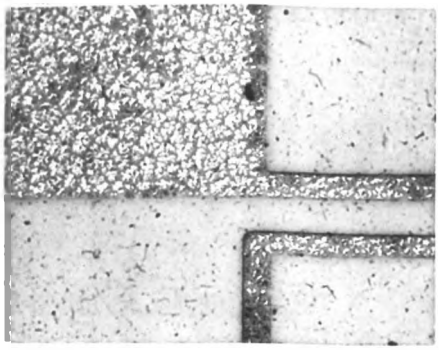

OXIDIZED ONLY

(4 hr., 750°C)

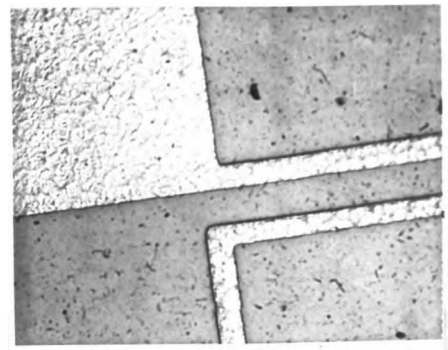

IRRADIATED WITH Kr

& OXIDIZED

(4 hr., 750°C)

Fig. 9.2. Optical micrograph of the film after 4 hours of oxidation at 750° C.

(a) The film is broken up into islands after oxidation only.

(b) The film continuity is preserved after it was irradiated and oxidized.

X-ray diffraction spectra of few samples at selected points in the evolution of a sample have confirmed the presence of Co and Co_2Si toward the end of the oxidation process at the expense of $CoSi_2$ in the beginning.

As the Co content of the film moves beyond that of Co_2Si, an observation with an optical microscope shows the onset of a morphological instability, as a result of which the film becomes discontinuous and ultimately non-conductive as can be seen from Fig. 9.2a. The dominant process(es) leading to this morphological instability are not understood at present. To examine this phenomenon further, we describe in the subsequent sections two experiments in which a simple aspect of this possibly complicated process is considered in detail. Specifically, section 9.2b considers the effect of Si on the morphological stability of the film upon simple thermal treatment in a vacuum (i.e., without oxidation). Section 9.2c considers the effect of a transport of Si across a film that consists of $CoSi_2$ throughout the oxidation process.

9.2b Dependence of the morphological stability of the film on its Co/Si ratio under vacuum annealing

We examine here the influence of added Si on the stability of a Co film on a SiO_2 substrate upon various vacuum annealing ranging from 650° C to 1050° C. A pure Co film of 370 Å and another such film deposited on 70 Å of Si were examined. The latter sample corresponds to a Si/Co atomic ratio of 0.11 which is in the solid solubility region of Si in Co according to the Co-Si binary phase diagram. The pure Co film was annealed consecutively at temperatures of 700, 750, 800, 825, 850, 875, and 900° C for 1 hour each. The Co film with the Si was annealed similarly at 650, 900, 960, 1000, and 1050° C for 1 hour also. After each annealing step the samples were examined under an optical microscope at 5000x. The pure Co film began to break up into small Co islands at 875° C thus becoming noncontinuous. This was confirmed by

the failure of the film to conduct electrically past this point. The Co film with Si showed no sign of island formation at any temperatures and remained electrically conductive up to 1050° C. Thus even a small amount of Si morphologically stabilizes the film on SiO_2. This outcome was found to be true for Si/Co atomic ratios as high as 2. On the other hand, we showed in previous section that when original $CoSi_2$ film turns into Co-rich silicide through 750° C wet oxidation, the film becomes morphologically unstable even though the film still contained one Si atom for 2 Co atoms. It is clear that other factors besides the content of Si contribute to the morphological instability in the oxidation of Co-silicide on a SiO_2 substrate.

9.2c Effect of Si transport in the Co-silicide film during the oxidation of $CoSi_2$

To study the contribution of Si transport through the silicide film to the film failure, we have used a sample with 1020 Å of $CoSi_2$ on a n-type Si <111> substrate of about 15-30 Ωcm. On this substrate, the oxidation will not alter the silicide composition, but will induce a flow of Si through the silicide film. The preservation of the stochiometric composition of the sample after oxidation was confirmed by RBS.

Nothing that would indicate a morphological instability could be detected under the optical microscope after 4300 Å of SiO_2 had been formed (~1hr. at 1000° C). About twice the amount of Si initially present in the $CoSi_2$ film is contained in that SiO_2 layer. From the RBS spectra, we know that the silicide layer remains fairly uniform during oxidation. The sheet resistance was measured to see if changes could be observed electrically. As shown in Fig. 9.3, the sheet resistance approximately doubles. The reasons for that increase remain to be determined, but evidently, the continuity of the film is not perturbed. We conclude from this experiment that the mere

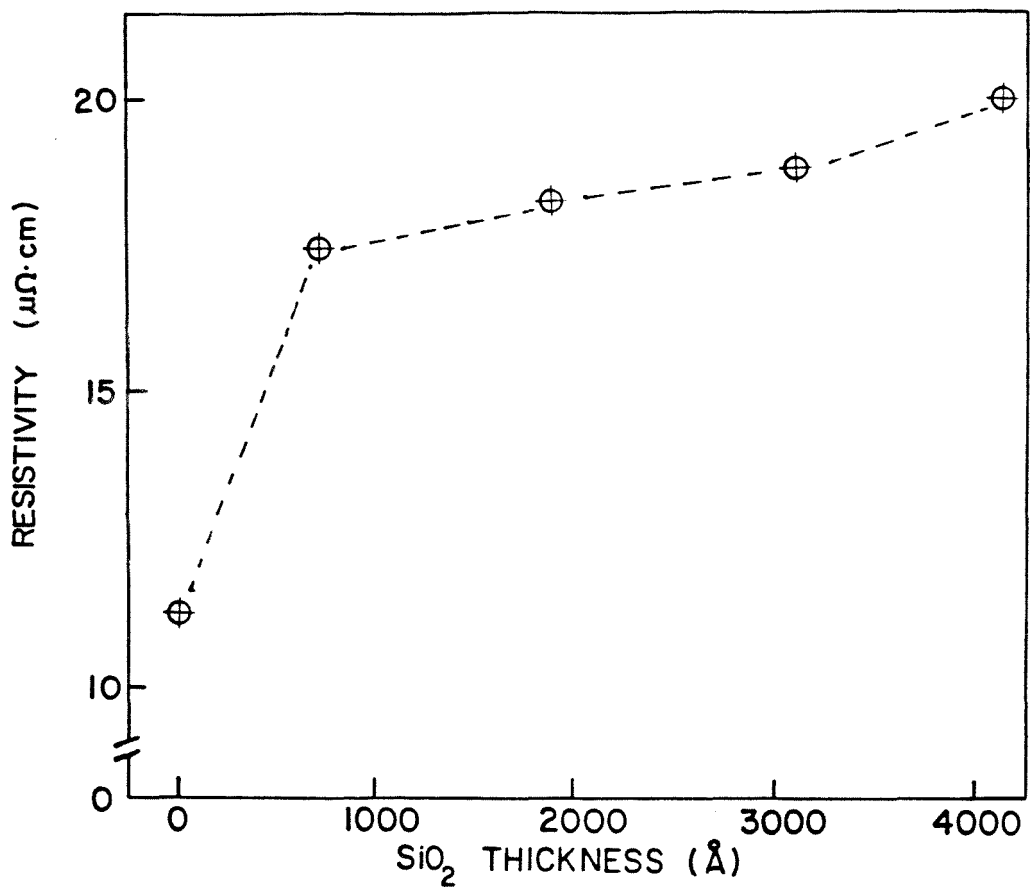

Fig. 9.3. Resistivity versus SiO_2 thickness of wet (1000° C) oxidized $CoSi_2$ film on Si <111> substrate.

existence of a relative transport of Si against and Co during oxidation is insufficient to cause a morphological instability.

9.2d Effects of Kr irradiation on $CoSi_2$ interconnect oxidation

It has been shown recently by Baglin [6], that there is enhancement of Cu film adhesion on SiO_2 through low energy (10^2 keV's) Ne ion irradiation. Tombrello et al. [7] have shown improved bonding of thin metal films on various substrates through irradiation of high energy ions (~10^1 MeV's). We have attempted to improve the stability of the films during oxidation with ion irradiation. Two types of bilayered samples were prepared in which either the Si or the Co layer was facing the SiO_2 substrate (SiO_2 substrate/Si (1500 Å)/Co(400Å) and SiO_2 substrate/Co(460 Å)/Si(1500 Å)). After the consecutive evaporations, some of the samples were pre-annealed in a vacuum furnace at 650° C for 30 minutes. This treatment produced a $CoSi_2$ film without fully consuming the Si layer. All four types of samples were then irradiated with 210 keV Kr^{++} (projected range of 160 nm; beyond the Co-silicide/SiO_2 substrate interface) at room temperature to fluences of 3-8x10^{15} Kr/cm^2.

Of the four cases considered, the irradiation produced a visible improvement of the film stability only for preannealed samples where the Si film was initially facing the SiO_2 substrate. Fig. 9.2 shows such a sample after oxidation at 750° C for 4 hours. Without irradiation (Fig. 9.2a), islands are formed; while with irradiation (Fig. 9.2b), the film is still continuous. To characterize its improvement, we quantify the morphological instability by measuring the percentage of the exposed substrate area on an optical micrograph when the film is broken up after oxidation. This percentage is plotted in Fig. 9.4 versus oxidation time for the irradiated and non-irradiated samples. We see that irradiation suppresses the failure up to a certain point only beyond which the film again fails.

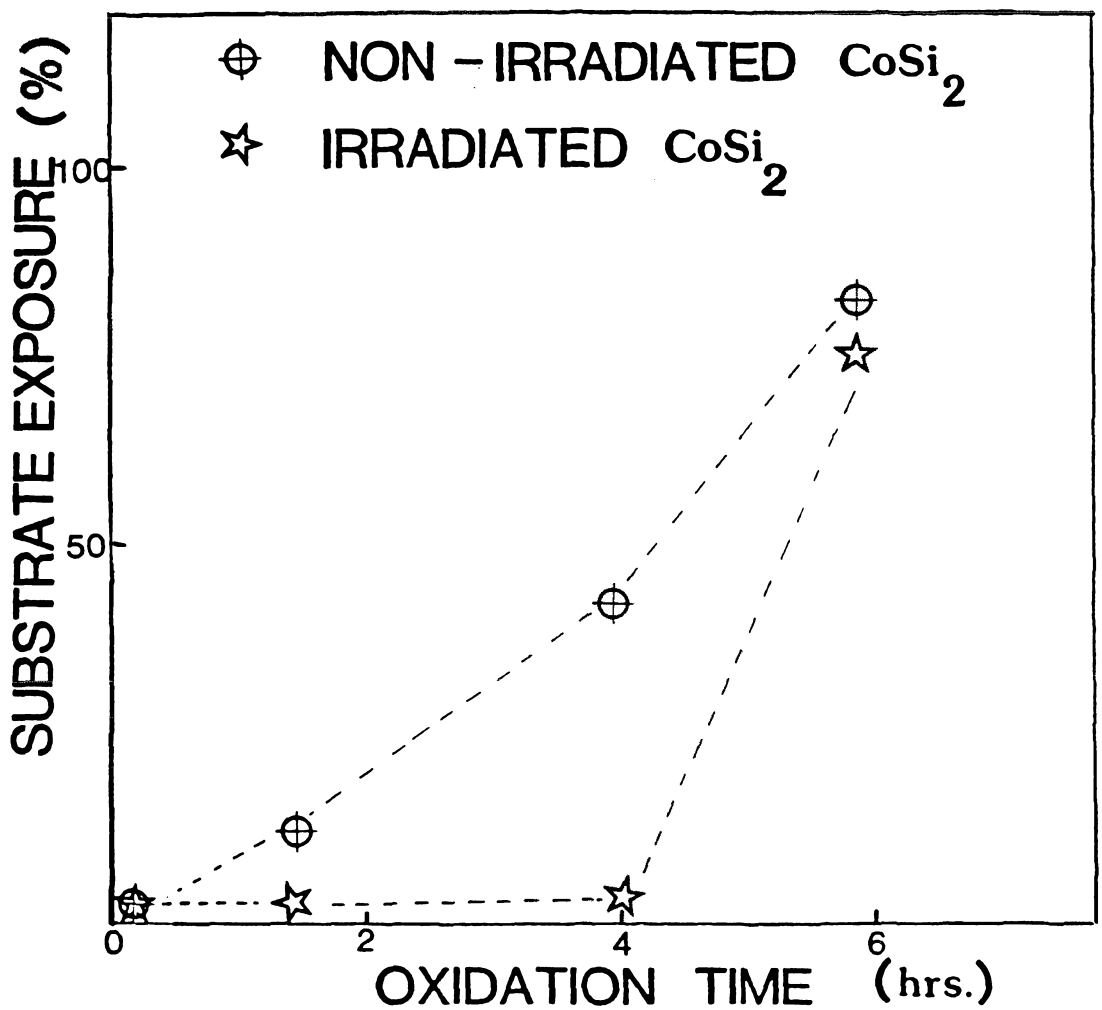

Fig. 9.4. SiO_2 substrate exposure due to the film instability during oxidation versus oxidation time of irradiated and non-irradiated $CoSi_2$ film.

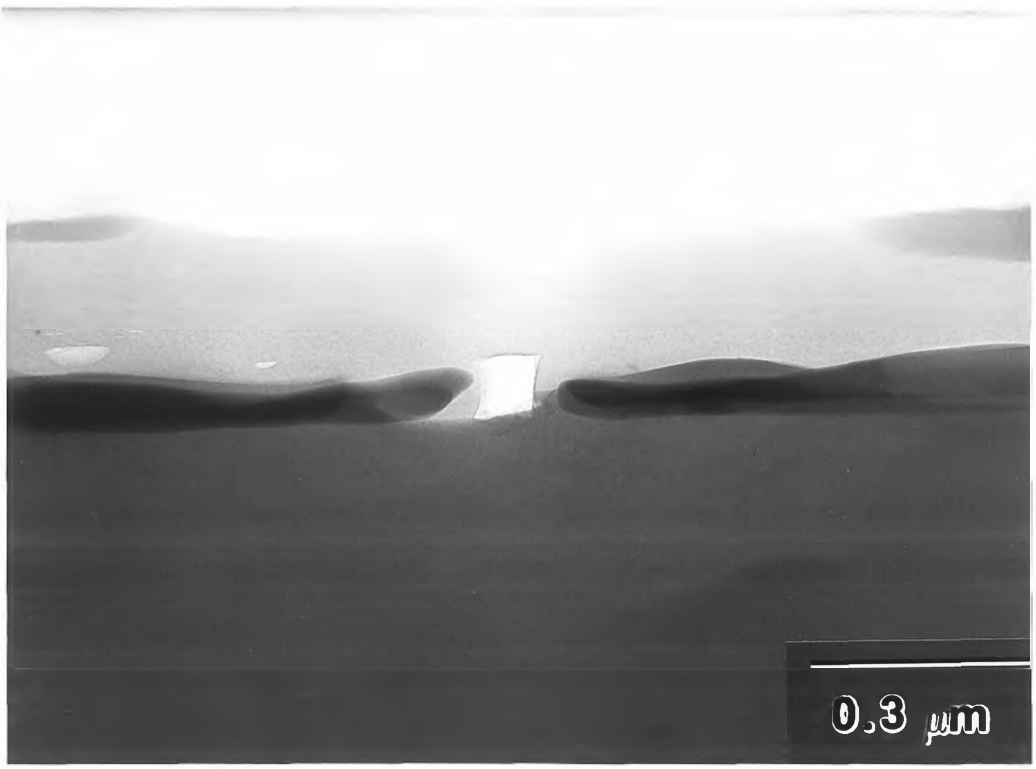

Fig. 9.5. Cross-sectional TEM of the $CoSi_2$ film after 1.5 hours of oxidation at 750° C. Voids formation were observed where the silicide film breaks.

This result raises questions; in particular, one wishes to know if this instability is a volume or interface effect. TEM and SEM were employed to investigate the interfacial structure of selected samples from which we observed little difference between in the volume of irradiated and non-irradiated silicide films and at the silicide/SiO_2 interface before oxidation. After oxidizing for 1.5 hours, void formation was observed in both irradiated and non-irradiated samples where the silicide film breaks. This is shown in the cross-sectional TEM picture of Fig. 9.5. The Co-silicide film is seen between the SiO_2 substrate and ~1500 Å of SiO_2 grown above it. The dimension of the void fitted between the film is comparable with that of gap, suggesting that the lateral shrinkage of the film is a consequence of the void formation or vice versa. Thus the morphological instability of the film is a consequence of a lateral displacement of the silicide during oxidation. Some samples were analyzed by RBS before and after irradiation with $8x10^{15}$ Kr/cm^2. A spreading of the Co signal into that of SiO_2 was observed which indicates intermixing. Baglin et al. [6] have shown improved adhesion through ion irradiation by promoting chemical or mechanical bonding. This enhanced adhesion could contribute to the observed delayed of failure in the irradiated films during oxidation in our samples. Why the irradiation affects differently prepared samples remains to be explained.

Electrical measurements were also made before and after Kr irradiation. The Hall mobility drops significantly from a value of 10 cm^2/Vs to 0.4 cm^2/Vs while the carrier concentration stays near $2x10^{22}$ /cm^3. A similar behavior has been reported previously for $NiSi_2$ and $CoSi_2$ [8]. Subsequent vacuum annealing at 750^o C restores the initial values. It is thus clear that irradiation also alters the volume of silicide; it is unclear if it is the volume effect that plays a role in the delay of the instability of the film during oxidation. We conclude that ion irradiation can stabilize the Co-silicide films on SiO_2 substrates during oxidation, but the procedure may be of limited practical use.

9.2e Conclusion

This investigation reveals some interesting facts concerning the oxidation of a $CoSi_2$ film on a SiO_2 substrate, i.e.,

1. As it is oxidized, the silicide film goes through composition changes, forming increasingly metal-rich silicide.

2. As it is oxidized, the film becomes morphologically unstable and eventually breaks up into discrete islands.

3. Upon annealing in vacuum a pure Co film is morphologically stable below about 875° C; above that temperature, the film breaks up into islands, as was shown previously by Pretorious et al. [9].

4. A presence of Si in the Co film stabilizes the film under annealing at all temperatures considered (up to 1050° C).

5. The presence of Si in the Co films by itself is insufficient to stabilize the film morphologically under oxidation.

6. Ion irradiation delays the film failure during oxidation.

7. Ion irradiation improves the film stability only for certain conditions of film preparation.

8. On a Si substrate, a $CoSi_2$ film remains morphologically stable upon oxidation; the displacement of Si atoms against Co atoms by itself is thus insufficient to destabilize the film morphologically under oxidation.

9.3 References

[1] M. Bartur, and M-A. Nicolet., Appl. Phys. Lett., 44 (1984) 263.

[2] S.-J. Kim, Senior Thesis, Calif. Inst. of Tech., (1983).

[3] M. Hansen, and K. Anderko, Constitution of Binary Alloys, (McGraw-Hill, New York, 1958) p.503.

[4] M-A. Nicolet, and S.S. Lau, in VLSI Electronics: Microstructure Science, Vol. 6, Eds. N.G. Einspruch and G.B. Larrabee, (Academic Press, New York, 1983) p. 402.

[5] C.-D. Lien, M. Finetti, M-A. Nicolet, and S.S. Lau, J. Electon. Mater., 13 (1984) 95.

[6] J.E.E. Baglin, G.J. Clark, and J. Bøttiger, Nucl. Instrum. and Meth., B7/8 (1985) 881.

[7] J.E. Griffith, Y. Qiu, and T. Tombrello, Nucl. Instrum. and Meth., 198 (1982) 607.

[8] J.C. Hensel, R.T. Tung, J.M. Poate, and F.C. Unterwald, Nucl. Instrum. and Meth., B7/8 (1985) 409.

[9] R. Pretorius, J.M. Harris, and M-A. Nicolet, Sol. State Electr., 21 (1978) 667.

Chapter 10

EFFECTS OF ADDED Si ON Co AND Ni FILMS

10.1 Almost elemental metals as interconnects in VLSI

In the last chapter we have shown that elemental metals are attractive alternatives to silicides for metallization in VLSI. It was also shown that [1, 2] that we could produce Co and Ni films with a protective SiO_2 overlayer by thermally oxidizing Co and Ni disilicides on a SiO_2 substrate. In that study as the disilicides become metal-rich through depletion of Si by oxidation, a morphological instability sets in which results in a break-up of the metal-rich film. The electrical and chemical characteristics of these metal-rich films remained unknown. For applications, the origin of the morphological instability must be clarified and procedures developed to circumvent it. Assuming that this were accomplished, the properties of the films, and specifically their electrical resistivity, need to be known as well in order to establish the usefulness of these films for interconnection lines. The removal by oxidation of Si from a metal-rich film has both theoretical and practical limits. To translate the resultant residual Si concentration into a resistivity of the film, one has to know how the resistivity of the metal varies with a residual Si concentration.

To answer this question, we investigate here the properties of Co and Ni films as a function of Si concentration in the range of Si solid solubility (i.e., <12 at.% for Co and <10-12 at.% for Ni) [3].

10.2 Chemical, physical and electrical changes in Co and Ni films by adding a small amount of Si

We have investigated the chemical phases, crystal structure, film morphology, and film resistivity of Co and Ni films with various amounts of Si.

The samples studied in this work were prepared on thick (~1μm) SiO_2 layers grown on <111> Si wafers by thermal oxidation. These inert substrates were used to minimize the interference of the substrate with the samples during thermal annealing. The substrates were cleaned organically and plasma oxidized for 10 minutes before loading into an electron-gun evaporation system. The Co (or Ni) and the Si layers were evaporated sequentially in one pumpdown at pressures between $5x10^{-8}$ and $2x10^{-7}$ Torr. The thicknesses of all the samples were kept near 230 nm, to eliminate a possible thickness dependence of the electrical resistivity and the chemical changes of different samples. The atomic composition of our samples were Co, $Co_{97.5}Si_{2.5}$, $Co_{94}Si_6$, $Co_{89}Si_{11}$, and Ni, $Ni_{97.7}Si_{2.3}$, $Ni_{94}Si_6$, $Ni_{88.5}Si_{11.5}$, $Ni_{78}Si_{22}$. The annealing were carried out in a quartz tube vacuum furnace at pressures between $3x10^{-7}$ to $7x10^{-7}$ Torr, depending on the temperature. The samples were annealed at 400, 500, 600, 700, 800, and 900° C for 1 hour. Thickness and composition of the samples were determined by 2 MeV $^4He^+$ Rutherford Backscattering Spectrometry (RBS) with the surface barrier detector of a resolution near 20 keV. The angle between the He beam and the sample normal was 10° to minimize channeling, and the scattering angle was 170°. Lattice constants and phases of the samples were investigated with an X-ray Read camera and Philips theta-two theta vertical diffractometer using Ni-filtered Cu-Kα radiation (λ =1.542 Å). The electrical resistivity of the films was measured at room temperature (24+/- 3° C) with a four point probe according to van der Pauw's method. The surface morphology of various samples after thermal annealing was examined using scanning electron and optical microscopy.

10.2a Phases and composition changes

The RBS spectra of a pure Co film 230 nm thick shows insignificant changes after annealing up to 700° C. However, for 800 and 900° C, the Co and substrate Si signals broaden. Such a spreading of signals could be due to either a laterally uniform interaction between Co and SiO_2, or to morphological changes of the Co film, such as an agglomeration of the film. In reference 2, it is reported that a Co film on a SiO_2 substrate breaks up into islands during vacuum annealing. We believe that the changes we see in the RBS spectra of a Co film annealed at 800 and 900° C are due to the agglomeration of the film. This point will be clarified in section 10.2c where we discuss the morphology of the film. In contrast, a pure 270 nm thick Ni film has an invariable RBS spectrum up to 900° C. This indicates that Ni is less likely to agglomerate than Co on a SiO_2 substrate upon vacuum annealing at high temperatures. According to references 2 and 3, Co and Ni film on SiO_2 behave similarly upon thermal vacuum annealing. The discrepancy in our results for Ni may be due to differences in film thickness.

For a $Co_{97.5}Si_{2.5}$ film (216 nm Co film with a 10 nm Si overlayer), the overlayer Si signal of RBS spectra shows spreading as the annealing temperature rises from 400° C to 600° C. At 700° C and above, the Si signal acquires the shape of a step, indicating that Si is uniformly distributed in the Co.

Similarly, a $Ni_{97.7}Si_{2.3}$ film (10 nm of Si on 226 nm of Ni), also starts to interdiffuse at 400° C. However, in this case the Si signal spreads more than in the Co-Si system after 400 and 500° C annealing. At 600° C and above, the Si signal is almost constant in amplitude. This indicates that Si diffuses faster in Ni than in Co for a given temperature of annealing, and that the temperature for uniform Si distribution is lower for Ni than for Co.

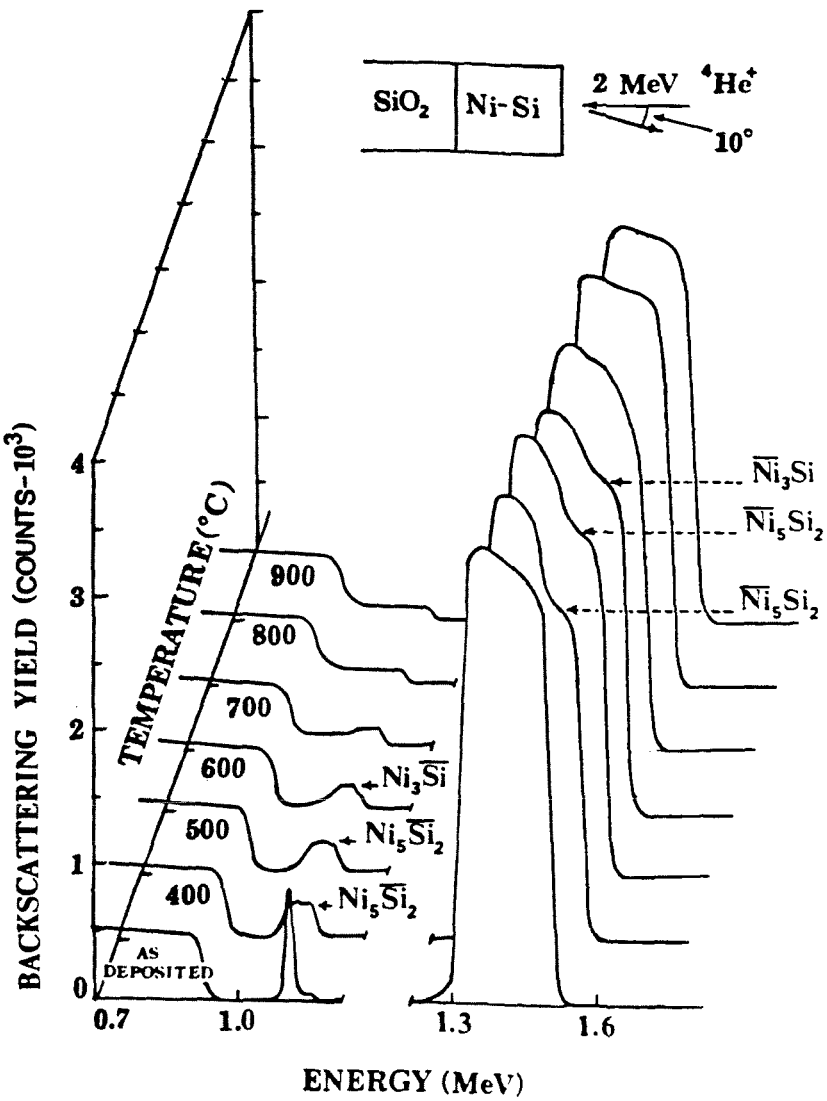

Fig. 10.1. 2.0 MeV He^+ backscattering spectra of a 37 nm Si film deposited on a 157 nm Ni film, as deposited and vacuum annealed for 1 hour at various temperatures ranging from 400 to 900° C. The spectra give a Ni to Si signal height ratio that suggests that Ni_5Si_2 and Ni_3Si are formed for the samples annealed at 400, 500, and 600° C. At 700° C, the Si and Ni steps for the compound formation start to disintegrate. At 800 and 900° C, Si has dissolved in the film, and x-ray diffraction data confirmed that no other phase but that of Ni is present in the film.

With a $Co_{94}Si_6$ film (23 nm of Si on 207 nm of Co), a compound layer is observed first. At 400° C, RBS spectra indicate the formation of 35 nm of Co_2Si with 184 nm of unreacted Co below. From the amount of Si available, one would expect a layer of 37.6 nm if all the Si formed Co_2Si. Thus, the RBS result indicates that most of the Si is bound in a Co_2Si layer at 400° C. At 500° C and 600° C, the RBS spectra change little. To confirm the presence of Co_2Si, we took an X-ray diffraction pattern with a Read camera for a film annealed at 600° C; it indeed contained lines of the Co_2Si phase and of Co. At 700° C and up, the Si and Co RBS signals for Co_2Si disintegrate, indicating that Si is uniformly distributed into Co.

With a $Ni_{94}Si_6$ film (206 nm of Ni and 23 nm Si), RBS spectra indicate the formation of 49 nm of Ni_5Si_2, with 180 nm of unreacted Ni upon 400° C and 500° C annealing. At 600° C the Ni_5Si_2 phase decomposes; the Ni and Si steps disappear from RBS spectra. However, Si was not completely dissolved at that temperature as one could still see a small peak in the surface Si signal. Only after annealing at 700° C and above does the Si signal become uniform in height. Thus, compared to $Ni_{97.7}Si_{2.3}$, the temperature for Si dissolution in Ni has risen from 600° C to 700° C for $Ni_{94}Si_6$, which may be due to the formation of Ni_5Si_2 in this system.

In the $Co_{89}Si_{11}$ film (189 nm of Co and 41 nm of Si), we infer from RBS spectra that 65 nm of Co_2Si form at 400, 500, and 600° C with 150 nm of Co remaining. X-ray Read camera diffraction data of a sample annealed at 500° C confirm the formation Co_2Si. Above 600° C, however, Co_2Si starts to disintegrate, as evidenced by the spreading of Si and the Co signals. For the sample annealed at 700° C, the step in the Co and Si signals for Co_2Si are not distinct anymore, and at 800° C and 900° C, the Si signal becomes uniform in height. The case of a $Ni_{88.5}Si_{11.5}$ film (156 nm of Ni and 37 nm of Si) is described in detail by the RBS spectra of Fig. 10.1. We infer the formation 71 nm of Ni_5Si_2 with 102 nm of Ni for 400 and 500° C thermal annealing, and at 600° C, 63 nm of Ni_3Si and Ni, but no Ni_5Si_2. X-ray diffraction

data for this sample reveal only the Ni_3Si and the Ni phases. As the temperature rises to 700° C, the step in the Ni signal starts to disappear and the Si signal begins to spread. At 800° C and 900° C, the signal of Si in the film is uniform, indicating that a solid solution of Si in Ni forms.

We have also investigated films outside of the solid solubility region, namely $Co_{79}Si_{21}$ and $Ni_{78}Si_{22}$. The $Co_{79}Si_{21}$ film had 137 nm of Co and 64 nm of Si, and the $Ni_{78}Si_{22}$ film had 133 nm of Ni and 67 nm of Si. According to the phase diagrams of the bulk systems, in equilibrium one expects to find Co_2Si and Co-Si solid solution for the Co-Si system, and Ni_3Si and Ni-Si solid solution for the Ni-Si system. Thermal annealing at 400, 500, and 600° C produced 86-89 nm of Co_2Si and 78-86 nm of Co (possibly containing Si) from RBS spectra. We verified these phases from X-ray Read camera diffraction patterns. The amount of Si deposited was sufficient to produce 105 nm of Co_2Si, but RBS data indicated that less Co_2Si formed. Thus, the remaining Si must have dissolved in the Co, as predicted from phase diagram. At 700° C, the RBS data show that Co_2Si starts to decompose, which decreases the Co_2Si thickness to 75 nm and increases the Co-Si solution to 90 nm. At 800 and 900° C, Co_2Si completely decomposes, and Si dissolves into the Co film. X-ray diffraction of a 900° C sample only contained Co lines.

For the Ni-Si system, we infer from RBS data that 152 nm of Ni_5Si_2 forms and that 52 nm of Ni (possibly with Si) remains at 400° C (120 nm of Ni_5Si_2 and 58 nm of Ni at 500° C). From the X-ray Read camera data, however, we also saw a Ni_3Si phase ring besides Ni_5Si_2 and Ni for the sample annealed at 500° C. As the temporature rises to 600° C and 700° C, the Ni_5Si_2 phase disappears and 122 nm of Ni_3Si and 48 nm of Ni forms, as was confirmed by both RBS data and X-ray diffraction from the Read camera. Thus, at 800° C, Ni_3Si starts to decompose. At 900° C we observe total dissolution of Si in Ni film from RBS and X-ray diffraction data. In the Ni-Si system, similar to the Co_2Si compound in Co-Si system, the compound Ni_3Si seemed to be

unstable at high temperature. Our data thus suggest that even for 22 at.% Si, the Si dissolves completely and uniformly in both Co and Ni upon vacuum annealing at 900° C. Whether the Si is incorporated in form of microcrystalline precipitates of a silicide, or as a metastable solid solution would have to be determined through further analyses. The existence of extended solid solution of si in Co and Ni has been reported [5, 8].

From thermal annealing experiments we observed that in all of our Co-Si and Ni-Si films, the Si dissolved completely in Co or Ni film at 800° C and 900° C thermal annealing. At 400, 500, and 600° C, we observed many metal-rich phases in equilibrium with metal solution for the system with 6 to 22 at.% Si atoms. In reference 4, the formation Ni-rich silicides have also been investigated. Ni_2Si, Ni_5Si_2, and Ni_3Si forms for 1 hour annealing 300, 400, and 450° C respectively. In our experiment, the lowest annealing temperature was 400° C and we do not observe the Ni_2Si phase, but we do observe Ni_5Si_2 at 400 and 500° C and Ni_3Si at 600° C. The phase sequences and temperatures are the same in both case, except for our elevated formation temperature of Ni_2Si. This discrepancy may be due to the different sample configuration used in the two experiments, coupled with impurity effects.

10.2b Changes in the lattice structure.

We have also investigated the changes in the lattice structure as a function of the amount of Si in solid solution. For this study we have taken samples up to 11 at.% Si annealed at 900° C. The RBS data of these samples show that Si is distributed evenly throughout the metal film and X-ray diffraction patterns of all the annealed samples did not reveal any compound phases, but only Co or Ni diffraction patterns.

In the Co-Si system, all the samples, including the as-deposited elemental Co film, were identified as fcc Co phase, which is the stable modification of Co above

450° C. Below 450° C, hcp is a stable phase for Co. Since the samples were annealed at 900° C, and the X-ray analysis was done at room temperature, we conjecture that as the samples were taken out of the annealing furnace, the cooling rate was sufficient to preserve the metastable fcc phase at room temperature. A similar phenomenon has been reported elsewhere [5], where bulk Co and its alloys were rapidly quenched from the liquid state to retain the high-temperature fcc phase at room temperature. We observed that the as-deposited Co sample also exhibited the high temperature fcc phase. Even though these samples were not annealed at high temperature, it is possible that during e-gun evaporation, the hot Co vapor is quenched on the cold SiO_2 substrate and retains its high temperature fcc phase. The fcc phase for as-deposited Co thin film has been previously reported [6, 7], and it has been suggested that the stacking faults are the nucleation sites for the transformation of the metastable fcc phase to the stable hcp phase at room temperature. However, in thin evaporated Co film, these stacking faults are not abundant enough to transform the metastable fcc phase to the stable hcp phase. Thus, the evaporated Co film, unlike bulk Co, has the fcc phase at room temperature.

For pure Ni samples, we observed the fcc phase for both the annealed samples and the as-deposited elemental Ni sample. Ni has only one stable phase, namely fcc [3], at all temperatures, and our experimental results on thin films conform with that.

In Fig. 10.2, we show the changes of the Co and Ni lattice parameter as a function of the amount of Si atoms in these films, within Si solid solubility limit in Co and Ni. For comparison, the figure also shows results published for bulk fcc Co-Si [5] and Ni-Si samples. The lattice parameter we report here for the films is that measured perpendicularly to the film plane. For the as-deposited Co or Ni film, this lattice parameter is less than that of bulk Co or Ni. We believe that this decrease is due to intrinsic tensile stress developed in the film during e-gun evaporation. This intrinsic

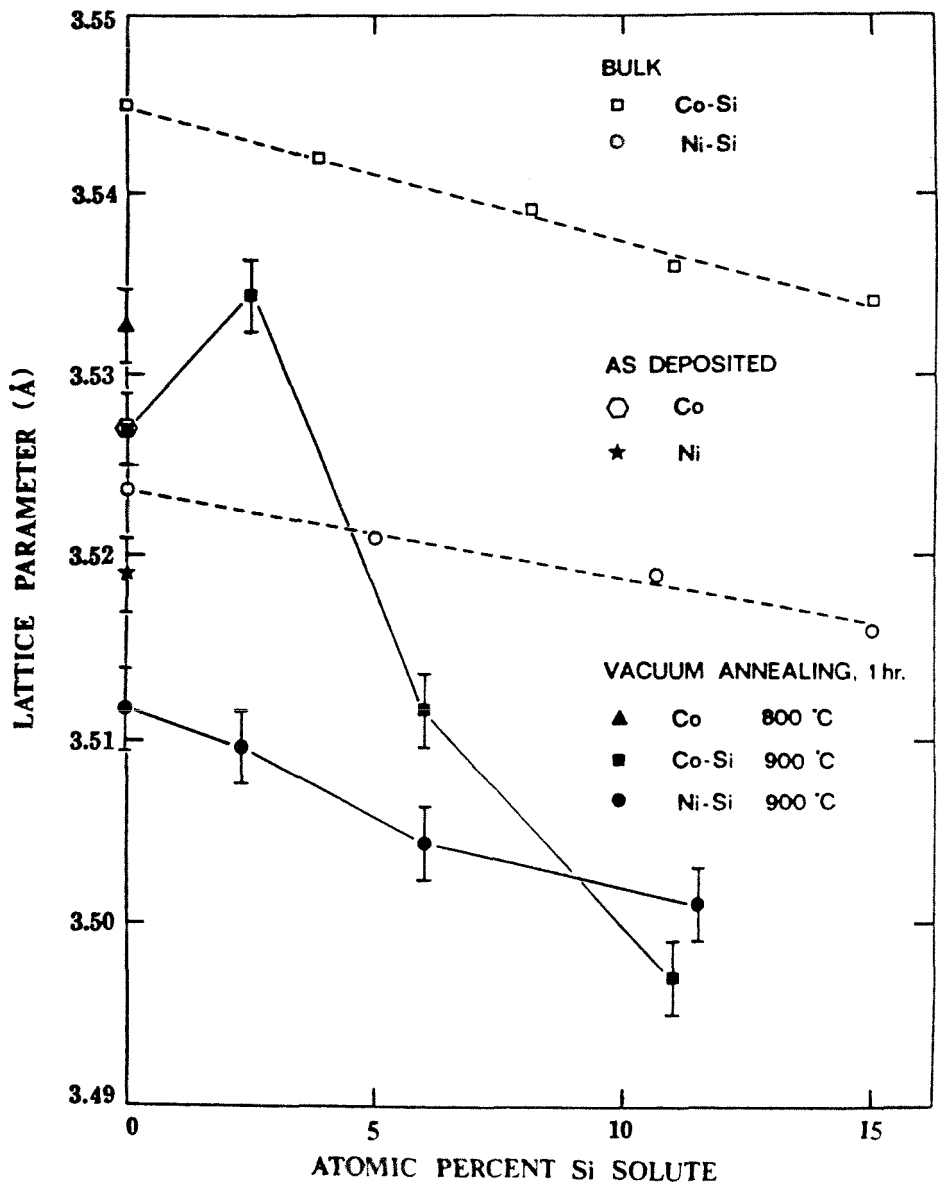

Fig. 10.2. Perpendicular lattice constant measured at room temperature for Co-rich and Ni-rich films vacuum annealed at 900° C for 1 hour, plotted against Si concentration.

stress is caused by structural defects created during the deposition and depends on the condensation rate, deposition temperature, ambient pressure, and type of substrate used [9].

When the samples are annealed, the defects presumably anneal out and the intrinsic stress decreases with increasing annealing temperature [10]. For sufficiently high temperatures, it is also reported [10] that the morphology of the film changes, which alters resulting increased stress. We see such a phenomenon in Fig. 10.2 where the tensile stress of the Co film annealed at 800° C decreases, that is, the Co lattice parameter increases and approaches the bulk value. However, when the sample is annealed at 900° C, the lattice constant decreases, i.e., the tensile stress increases again. At such high temperatures, the difference in thermal expansion of the film and the substrate can contribute significantly to the stress of the film.

To verify such a possibility, we have compared the stress value calculated for the thermal stress with the stress value obtained by measuring the changes in the perpendicular lattice parameter of our annealed samples. To calculate the thermal stress, S_{th}, we have used the following equation [11]:

$$S_{th} = (a_F - a_S)\, \Delta T E_f / (1-\gamma_F). \qquad (1)$$

Here, α_F and α_S represent the thermal coefficient of expansion of the film and the substrate, respectively, ΔT is the difference in annealing temperature and the room temperature, and E_f is the Young's modulus of the film. For stress obtained from lattice change, S_x, we have used the equation

$$S_x = \frac{E_f}{2\gamma_F} \cdot \frac{a_o - a}{a_o}, \qquad (2)$$

where γ_F is Poisson's ratio, and 'a_o' and 'a' are the lattice constants of the bulk material and the strained film, respectively. In equation 2, stress is assumed to be isotropic in the plane of the film and 'a' is the lattice constant perpendicular to the film plane, as was measured in our X-ray diffractometer. The values of the parameters used in equations 1 and 2 are listed in Table 10.1.

If we assume that the substrate is Si, the calculated $S_{th,\ Si}$ of Co on a Si substrate is 2.4 x 10^{10} dyne/cm^2, and if we assume that SiO_2 is the substrate, then $S_{th,SiO2}$ = 3.19 x 10^{10} dyne/cm^2. Since Co is on a SiO_2 layer (~ 1 μm) grown on Si wafer, the correct thermal stress of Co should be between $S_{th.\ Si}$ and $S_{th.SiO2}$. The X-ray stress, S_x, calculated for the pure Co film is 1.85 x 10^{10} dyne/cm^2, which is near the values of $S_{th.SiO2}$ and $Si_{th.Si}$ just calculated, and shows that the model of thermally induced stress for 900° C annealing is consistent with the data. For the pure Ni, $S_{th.Si}$ is 2.62 x 10^{10} dyne/cm^2, $S_{th.SiO2}$ is 3.49 x 10^{10} dyne/cm^2 and S_x is 1.6 x 10^{10} dyne/cm^2. We conclude that for both pure Co and pure Ni, the thermal stress can contribute a major amount of the total stress observed in the Co and Ni films annealed at 900° C.

For the Co and Ni films with Si in solid solution, Fig. 10.2 reveals the general trend that, as the amount of Si increases, the perpendicular lattice constant decreases. In these solid solutions, Si could be substitutional, interstitial, or both. When solutes are interstitial, the lattice of the solution always increases [16]; when the solute atoms are substitutional, the lattice can either increase or decrease, depending on the size of solute atom. The Si Goldschmidt atomic radius is 1.17 Å, while the Co and Ni's radii are 1.26 and 1.25 Å [17], respectively. We believe that in our case we have a substitutional solid solution of Si in Co and Ni, since Si atoms are smaller than Co and Ni atoms and the lattices of Co and Ni solutions decrease as the amount of dissolved Si increases.

Table 10.1. Parameters used for the calculation of thermal stress and stress from the lattice parameter change for Co and Ni films on SiO_2 and Si substrate.

Parameters	Co	Ni	Si	SiO_2
E_f (10^6 psi)	30 [12]	30 [12]		
α (10^{-6} $^oC^{-1}$)	12 [12]	13 [12]	2.6 [13]	0.5 [13]
a_o (Å)	3.544 [14]	3.524 [14]		
a_{900^oC} (Å)	3.524	3.507		
γ_F	0.32 [15]	0.31 [15]		
ΔT (^oC)	875	875		

For films of Si in Co solid solution, the perpendicular lattice constant of Co decreases much faster than that of the corresponding bulk solid solution [5], while in Ni the rate of the perpendicular lattice constant decreases at almost the same rate as that of the bulk [6]. For films of Ni solid solution, the total decrease in the perpendicular lattice constant is closely representable as an addition of the decrease due to thermal stress in the annealed elemental Ni film and of the decrease observed for the incorporation of Si in the bulk. Physically, such a situation would arise if the film of the solid solution is unstressed at the annealing temperature, if the elastic moduli are independent of Si content, and if the mismatch in thermal contraction upon cooling between film and substrate is responsible for the buildup of thermal stress. This model does not explain the Co data. The reasons are unclear, although it could be argued that the model still applies, but the elastic moduli change with the Si content. The result for 2.5 at.% Si in Co in Fig. 10.2 seems to break out of the general trend of the results. We have repeated the experiment with that sample, and we have obtained the same result. We do not understand these results; further investigations are needed here.

From the width of the X-ray diffraction peak we have also calculated the grain size of the film. For the calculation we have used the Scherrer's formula [18],

$$t = \frac{0.9\ \lambda}{B \cos \theta_B}\ , \qquad (3)$$

where λ is Cu-Kα wavelength used for X-ray diffraction, B is the half-width maximum of the peak, and θ_B is the diffraction angle. For Co-Si system, the grain diameter was in the range of 40-50 nm. For Ni-Si system it was in the range of 50-60 nm.

10.2c Morphological instability of the film

It has been previously reported [19] that Co and Ni films on SiO_2 substrates ball up into islands upon vacuum annealing at 800° C. We have reported similar facts in a previous chapter, where we reported that Co film of about 37 nm balled up at 875° C vacuum annealing and the similar film with 7 nm or with 11 at.% Si did not ball up even at 1050° C thermal annealing. In our present experiment, we have Co-Si and Ni-Si films of thickness 230 nm on SiO_2 with 0 to 11 at.% Si. We have annealed them at temperatures ranging from 400° C to 900° C and we examined the surface morphology of the film by optical and scanning electron microscopy (SEM).

Some of the SEM pictures are shown in Fig. 10.3. In Fig. 10.3a, we see the Co agglomerations and even pits exposing the SiO_2 substrate as the elemental Co sample is annealed at 900° C. In the film with 2.5 at.% Si no pits form during the same heat treatment. The substrate surface remains totally covered, although the film becomes rough. With 10 at.% Si, there is less surface undulation than for the previous two samples. At lower temperature annealings, the surface of the Co film is very smooth. A typical example of a smooth film surface is shown in Fig. 10.3e, where we have annealed Co film at 500° C. Figs. 10.3d and 3e are the SEM pictures of pure Ni and $Ni_{97.7}Si_{2.3}$ films on SiO_2 substrate annealed at 900° C. The film surface of the Ni-Si samples are much smoother and more uniform than the corresponding Co-Si samples for similar heat treatment. The results show that a small amount of Si stabilizes the morphology of Co or Ni films at high temperature annealing. Also, Ni film (with and without Si) is morphologically more stable than Co film at 900° C annealing.

Fig. 10.3. SEM micrographs of SiO_2/Co/Si and SiO_2/Ni/Si samples vacuum annealed at 900° C.

a) Pits are visible in the pure Co film, exposing SiO_2 substrate.

b) A $Co_{97.5}Si_{2.5}$ film has no pits.

c) The surface morphology of $Co_{89}Si_{11}$ is more stable than that of pure Co or $Co_{97.5}Si_{2.5}$ films.

d) Even though some pits are visible in the pure Ni film, they are less frequent than in the pure Co film.

e) No pits are seen in a $Ni_{97.7}Si_{2.3}$ film (see also (b)).

f) Typical surface morphology of films as-deposited or vacuum annealed at 400 to 700° C.

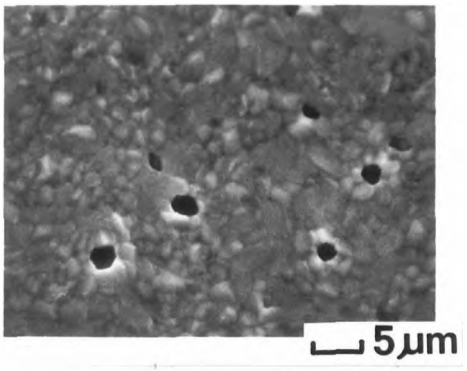

a

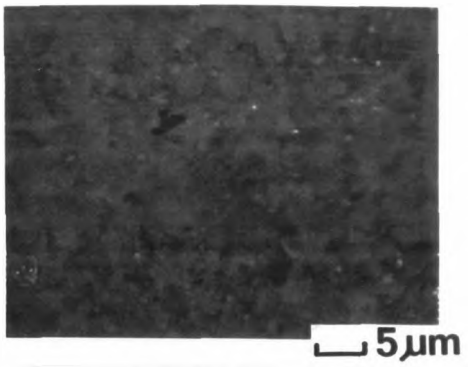

d

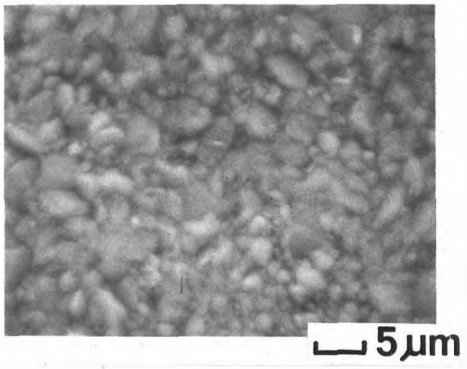

b

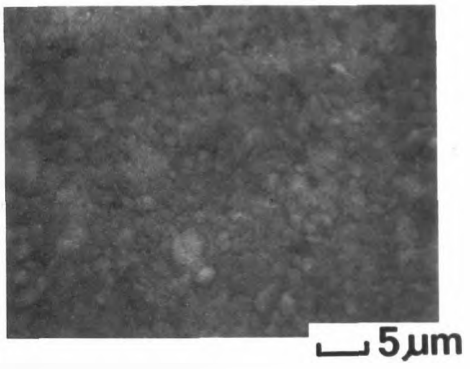

e

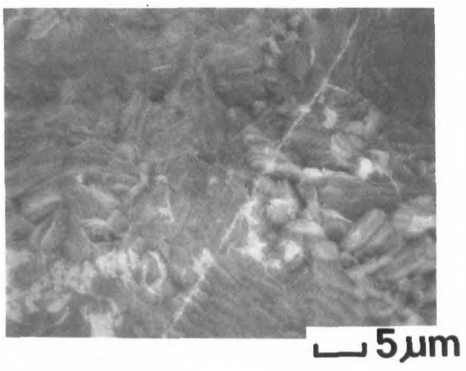

c

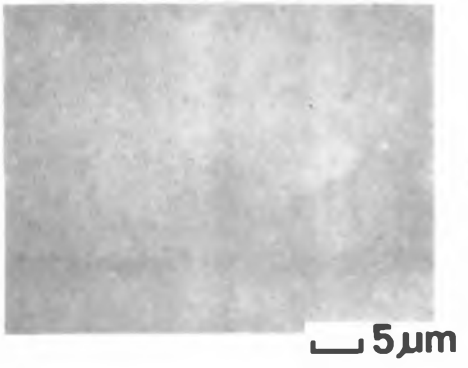

f

Unlike previous results [1, 2], our elemental Co and Ni films did not ball up into islands at 900° C thermal annealing. We believe that the enhanced thickness of our Co and Ni films contributes to this stability. To check, we evaporated pure Co and Ni samples of 100, 150, 250 nm thickness on SiO_2 substrates and annealed them in vacuum at 850, 900, and 950° C for 1 hour. Examination under an optical microscope at 500x showed that the thicker the film, the higher the temperature at which the film balls up. For example, 100nm of Co film completely balled up to 950° C annealing, however, for 250 nm of Co film, we did not observe any balling up at that temperature.

On the other hand, a Ni film of the same thickness of 100 nm was relatively stable at 950° C annealing. We observed only few isolated pits in the film, otherwise the film surface was uniform. For thicker Ni films, we did not observe any pits or agglomeration at 950° C. Thus, the annealing temperature at which a film balls up into islands depends on the film thickness. For a given thickness of the film and annealing temperature, pure Ni films are morphologically more stable on SiO_2 than pure Co films.

10.2d Resistivity of the film as a function of Si in the film and annealing temperatures

After annealing the Co-Si and Ni-Si samples at various temperatures for 1 hour, we have measured the film resistivity at room temperature as described before.

The results are plotted in Fig. 10.4 for Co-Si and in Fig. 10.5 for Ni-Si. For the pure Co sample, the resistivity decreases from 9.5 μΩcm to 5.8 μΩcm when the as-deposited Co sample is annealed at 400° C. As the annealing temperature increases, the resistivity rises again, reaching 8.2 μΩcm at 900° C annealing. Similarly, the resistivity of the pure Ni sample decreases from 9.3 μΩcm for the as-deposited sample to minimum of 7.5 μΩcm for 500° C annealing, and then increases reaching 10.4

μΩcm at 900° C annealing. This type of phenomenon is commonly observed [20, 21]. As deposited, the film contains a large amount of structural imperfection, especially vacancies, that contribute significantly to the resistivity. As the film is heated, these structural imperfections start to anneal out and the resistivity decreases. However, as the annealing temperature is raised further, the film may even agglomerate, and is subjected to increasing thermal stress upon cooling. Such distortions of the film contribute to the rise of the film resistivity.

The minimum resistivities we measured for the pure Co and Ni samples were 5.8 and 7.5 μΩcm, respectively. These values are very close to the pure bulk values, which are 5.25 μΩcm for Co and 6.84 μΩcm for Ni [15]. Our Co samples have a grain size of about 40-50 nm, and the Ni samples have a grain size of about 50-60 nm. The mean free path of the charge carriers in Co is about 10 nm and 20 nm for Ni [18], both of which are significantly smaller than the grain size. Also, our samples are about 230 nm thick, which is much larger than the grain sizes. The closeness in the resistivities of the bulk metals and our thin films is therefore as should be expected.

For Co film with 2 at.% Si, we observe from Fig. 10.4 that the samples annealed at 400, 500, and 600° C have distinctively lower resistivities than the samples annealed at higher temperatures. As was shown previously, at 700° C and above, the Si distributes uniformly into the Co. Thus, the jump in the film resistivity between 600 and 700° C annealing coincides with the dissolution of Si into Co, indicating that the high resistivity in the film is due to the dissolution of Si in the Co film. The cases for Co samples with 6 at.% and 11 at.% Si are quite similar. From the results shown, the samples annealed at 400, 500, and 600° C, all consist of a layer of Co_2Si on the remaining Co. However, at 700° C, Co_2Si starts to disintegrate, and at 800 and 900° C, Si dissolves in the Co. The sudden rise in the resistivity of the samples with 6 and 11 at.% Si is thus again associated with the formation of a solid solution of Si and Co.

In Ni films with 2.3 at.% Si, there is a small jump in the increase of resistivity from 500 to 600° C annealing. As was shown previously, Si diffuses faster and at lower temperatures in Ni than in Co. Correspondingly the increase of resistivity for Ni is more gradual than for Co as the Si more gradually diffuses in Ni for each annealing temperature. The pattern is similar for Ni film with 6 and 11 at.%. From the results, at 400 and 500° C a layer of Ni_5Si_2 forms on Ni; at 600° C, Ni_5Si_2 starts to decompose, and at 700° C and above, the Si dissolves in the Ni. These multiple chemical changes that occur for Ni lead to a more gradual increase in the resistivity of Ni films with Si than is the case for Co as the annealing temperature increases. This is so because the amount of unreacted and well-conducting Ni gradually decreases on account of the growing silicides of lesser conductivity (Ni_5Si_2 has 149 μΩcm, Ni_3Si has 93 μΩcm, and Co_2Si has 66 μΩcm). In the range of solid solubility, that is, for samples annealed at 800 and 900 ° C, the resistivity rises with the Si solute concentration. The resistivity increase is much more pronounced for Co than for Ni (see Figs. 10.4 and 10.5); specifically in Co, the resistivity rises by 4.5 μΩcm per at.% Si, but only by 2.8 μΩcm per at.% Si in Ni. The decrease in lattice parameter induced by Si dissolution is also more pronounced for Co than for Ni (see Fig. 10.2). These two facts correlate, suggesting a cause and effect relationship. For Ni, resistivity data of bulk material as a function of Si concentration at room temperature exist [23], and are also plotted in Fig. 10.5 (dashed line). The bulk data agrees quite well with the thin film data. Also, for Ni the change in the bulk lattice constant as a function of Si concentration equals that seen for the perpendicular lattice constant in Fig. 10.2. That indicates that for Ni, thin films and bulk are alike, both in terms of resistivity and lattice parameter. In particular, the perpendicular lattice parameter change, caused by adding Si, observed in Fig. 10.2 then should be viewed as a volume effect, i.e., it should be interpreted as being valid for all three axes. That conclusion was already drawn. The situation is not as transparent for Co. For Co, the resistivity of the film is more sensitive to the

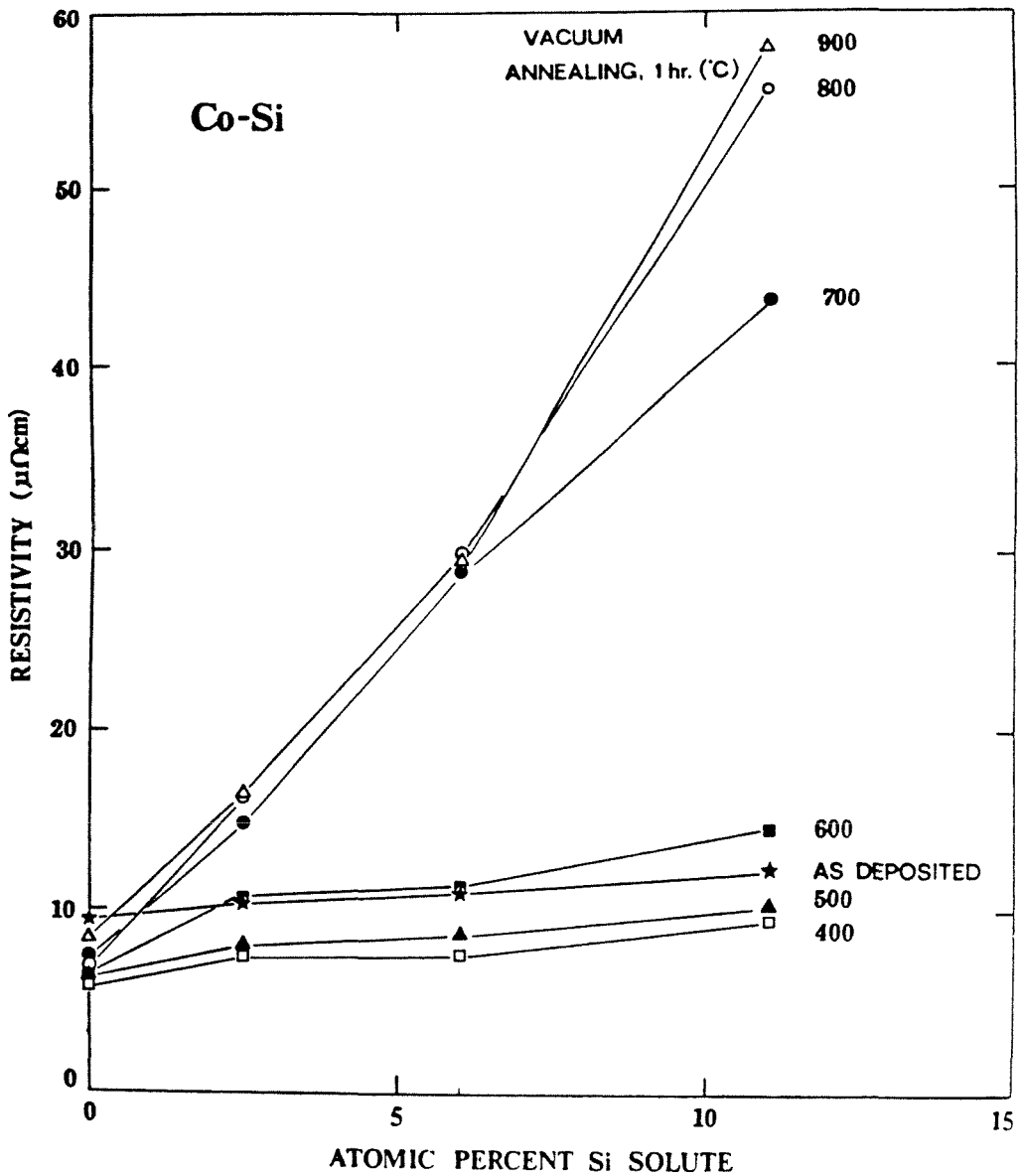

Fig. 10.4. Room temperature resistivity of Co-rich films as a function of Si concentration and the annealing temperatures of the film. All annealing were carried out in vacuum for 1 hour.

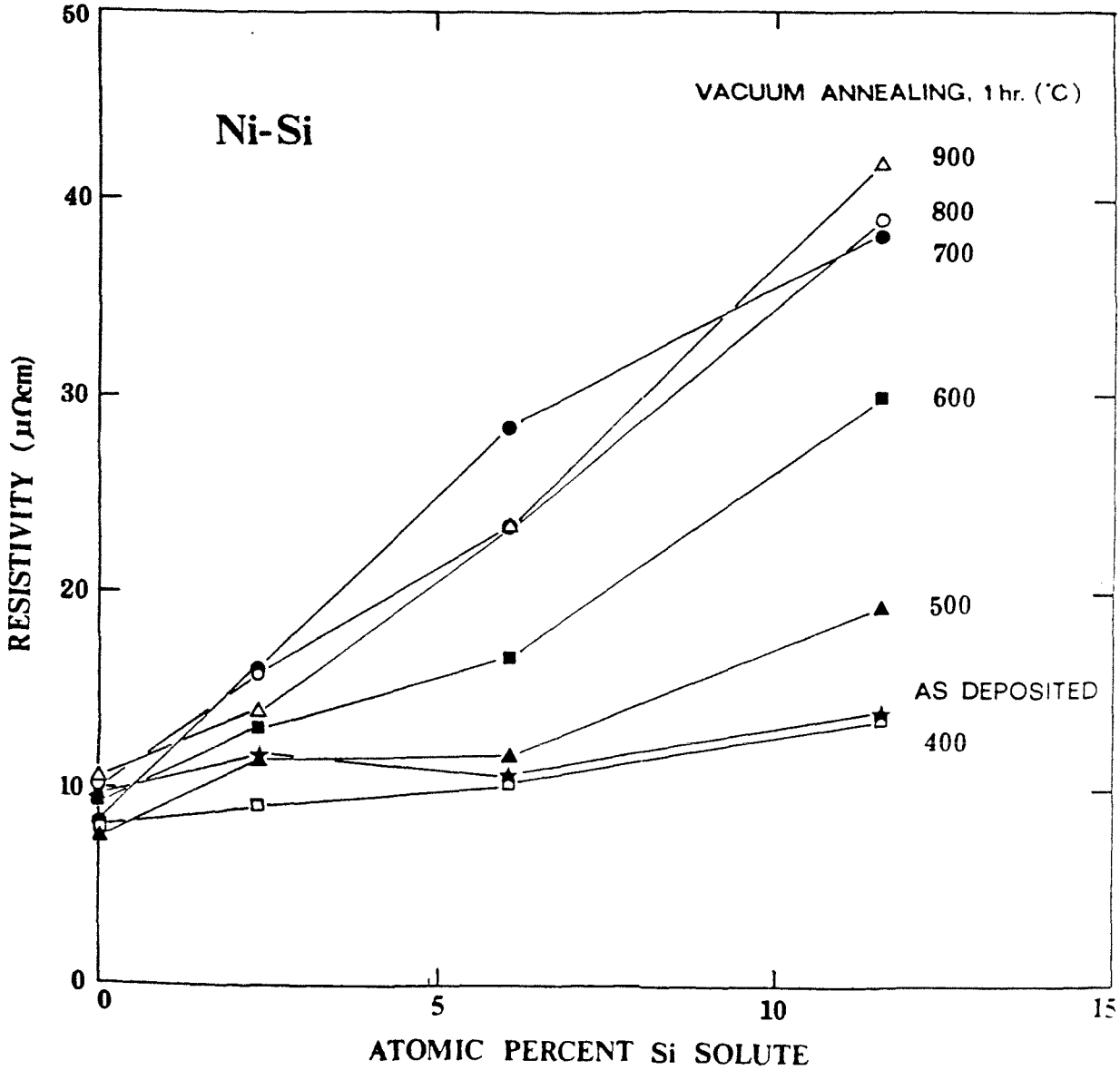

Fig. 10.5. Room temperature resistivity of Ni-rich films as a function of Si concentration and the annealing temperatures of the film. All annealings were carried out in vacuum for 1 hour. Dashed line represents resistivity data of bulk.

concentration of dissolved Si than for Ni. The same is true for the perpendicular lattice parameter. If the same relationship between resistivity change and lattice parameter change applied to both Ni and Co, that result would be expected. However, the change in lattice volume parameter of the bulk and in perpendicular lattice parameter of the film do not track for Co (see Fig. 10.2). Also, we have no data on how the bulk resistivity of fcc Co changes with Si content. Additional experimental facts are needed to explain these combined facts. We do know, though, that the difference in the sensitivity of the bulk and film lattice parameters to the Si concentration shown in Fig. 10.2 cannot be explained by assuming that the pure Co film is so well bonded to the substrate at 900° C that it undergoes elastic contraction in thickness when Si dissolves into the Co. That effect only increases the sensitivity of Si concentration by a factor of 1.6 above that of the bulk, while the film is about three times more sensitive than the bulk.

10.2e Summary

1. At 400, 500, and 600° C annealing, the phases Ni_5Si_2, Ni_3Si and Co_2Si are observed on excess metal for the samples with 6 to 22 at.% Si.
2. At 800 and 900° C, $CoSi_2$ and Ni_3Si disintegrate rapidly and Si dissolves in Co and Ni.
3. All as-deposited as well as the annealed Co films (up to 900° C) of all compositions exhibited the metastable fcc phase at room temperature. We also observed the fcc phase for Ni samples.
4. The lattice parameter perpendicular to the plane of the film of as-deposited and annealed Co and Ni thin films are smaller than those of bulk samples. Intrinsic stress created during deposition, and thermal stress induced upon cooling after high temperature annealing are the likely cause for such distortion of the lattice.

5. The perpendicular lattice constant of both Co and Ni decreases as the amount of Si in solid solution increases in the film.

6. Neither pure Co nor pure Ni films ball up when annealed at 900° C. Ni films are morphologically more stable than Co films when annealed at high temperatures. As little as 2.5 at. % Si produces a more uniform and regular surface than found on the pure metal film after annealing at high temperatures.

7. For both Co and Ni films, the resistivity increases as the amount of Si in solid solution increases. The rise is very sharp; about 2 and 3.6 at.% suffices to double the film resistivity of Co and Ni respectively. The rise in resistivity is caused both by impurity scattering and by strain-induced lattice distortion.

10.3 References

1. M. Bartur, and M-A. Nicolet, Appl. Phys. Lett., 44 (1984) 263.

2. S.-J. Kim, T.C. Banwell, R.Shima, and M-A. Nicolet, SPIE, 530 (1985) 152.

3. M. Hansen and K. Anderko, Constitution of Binary Alloys, (McGraw-Hill, New York) pp.503 & 1059.

4. C. Canali, G. Majni, G. Ottaviani, and G. Celotti, J. Appl. Phys., 50 (1979) 255.

5. H.L. Luo, and P. Duwes, Can. J. Phys., 41 (1962) 758.

6. T. Honna, and C.M. Wayman, J. Appl. Phys., 36 (1965) 2791.

7. L.S. Palatnik, A.G. Ravlik, and A.N. Stetserko, Fiz. Metal. Metalloved., 18 (1964) 632.

8. W. Klement, Jr., Can. J. Phys., 40 (1962) 1397.

9. H.S. Story, and R.W. Hoffman, Proc. Phys. Soc. London, B66 (1957) 950.

10. R.L. Chopra, Thin Film Phenomena, (McGraw-Hill, New York, 1969) p.284.

11. ibd, p. 270, 272.

12. Metals Handbook, Vol. 1, Eith Edition, Ed. T. Lyman (American Society for Metals, Metals Park, Ohio,1961) p. 48.

13. S.M. Sze, Physics of Semiconductor Devices, Second Edition, (John Wiley & Sons, New York, 1981) p. 851.

14. W.B. Pearson, A Handbook of Lattice Spacings and Structures of Metals and Alloys, Vol. 4 (Pergamon Press, Oxford, 1964) pp. 124 & 127.

15. Metals Handbook, Vol. 2, Ninth Edition, Ed. W.H. Cubberly (American Society for Metals, Metals Park, Ohio, 1978) pp. 726 & 777.

16. B.D. Cullity, Elements of X-ray Diffraction, Second Edition, (Addioson-Wesley, London, 1978) p. 375.

17. Smithells Metals Reference Book, Sixth Edition, Ed. E.A. Brandes (Butteworths, London, 1976) p.4-26.

18. Ref. 16, p. 102.

19. R. Pretorius, J.M. Harris, and M-A. Nicolet, Sol. St. Electr., 21 (1978) 667.

20. Ref. 10, p. 386.

21. S. Flugge, Encyclopedia of Physics, Vol. 19 (Springer-Verlag, Berlin,1956) p.197.

22. M-A. Nicolet, and S.S. Lau, in VLSI Electronics: Microstructure Science, Vol. 6, Eds. N.G. Einsprunch and G.B. Larrabee, (Academic Press, New York, 1983) p. 416.

23. C.A. Domenicali, F.A. Otter, J.Appl. Phys., 26 (1955) 337.

Chapter 11

OXIDATION OF Au-ALUMINIDES

11.1 Au bonds on Al metallization and its problems

Al is commonly used for metallization in VLSI for various reasons, among which are; a) Al has a very low resistivity of approximately 2.7 μΩ-cm at room temperature; b) Al adheres well to Si and SiO_2; and c) Al easily forms ohmic and Schottky contacts with Si. To transmit the signals of the chip to the outside world, leads are necessary. For that purpose Al alloy or Au wires are often used. When these wires are bonded to the Al metallization, difficulties arise. Al alloy wires become thin or brittle near the bond area which tends to result in breakage there. The Au wire, in other hand, is much more malleable than the Al wire and forms a good bond with the Al metallization. But Au easily forms intermetallics with Al that adversely affect on the bond strength and the electrical properties of the bond. We discuss here the problems of Au bonds to Al metallization.

The joule heating and the electromigration during the normal IC operation promote the chemical reactions between Au and Al. Even at room temperature, Au_5Al_2 phase is observed to form [1] in the Au-Al bond. At temperatures as low as 150° C, other phases of AuAl compounds have been reported to form [2].

As these intermetallics form, the bond strength weakens because voids form along the Au-rich intermetallic phases [3, 4]. These voids are believed to arise because Au and Al atoms interdiffuse at different rates. As Al diffuses more rapidly into Au than Au into Al, vacancies condense in voids which weaken the bond [3, 5]. This phenomenon is commonly known as the purple plague, since the breaking of the Au-Al bond is accompanied by the appearance of a purple color in the bonding area, which is

the color of $AuAl_2$ phase. Gases from the package material that surrounds the chip also enhance the degradation of the bond [6, 7]. Cl, Br, O_2 and H_2O have been observed to outgass from the package material [8, 9, 10] and pose serious problems of corrosion and chemical reaction on Au-Al bonds and Al metallization [9, 10].

Detailed studies and a good understanding of these problems are needed in order to alleviate them and develop a reliable Au-Al bond system for IC's. In this chapter we present the details of an investigation on the effects of dry O_2 and of water on films of Al and films of all Al-Au compounds ($AuAl_2$, AuAl, Au_2Al, Au_5Al_2, and Au_4Al) on SiO_2 substrates.

11.2 Experiments on the oxidation of various Au-aluminides under diverse conditions

The films were prepared on thick (~1 μm) SiO_2 layers grown on <111> Si wafers by thermal oxidation. These inert substrates were cleaned organically before loading into an electron gun evaporation system. The Au and Al layers were evaporated sequentially in one pumpdown at a pressure less than $2x10^{-7}$ Torr. The Au was always deposited before the Al to minimize the possible formation of an interfacial oxide layer that might hinder diffusion.

The thicknesses of all the samples were kept near 200 nm. The atomic ratios of Au to Al of our six sample types were 0:1; 1:2; 1:1; 2:1; 5:2, and 4:1 within +/- 10 %. It has been reported [1] that all these stable Au-Al phases can be obtained by depositing the exact stoichiometric quantities of Au and Al and annealing them at 500° C for prolonged periods of time. We have followed the same recipe by annealing the samples in a quartz tube vacuum furnace at a pressure of about $5x10^{-7}$ Torr at 500° C for 10 hours. The phases and atomic compositions of the samples were determined by X-ray Read camera and 2 MeV $4He^+$ Rutherford backscattering spectrometry (RBS). The

annealed samples showed the expected compound phases. These annealed samples were then oxidized in 1) dry O_2 at 500° C for up to 24 hours, 2) air at room temperature, and 3) deionized water at 40, 50, 70, and 100° C for up to 45 hours. The usual RBS method could not detect the very small amount of oxide that we wanted to measure. The amount of surface oxide and thin hydrates was measured by the elastic resonance scattering method using the 3.05 MeV O^{16} (α, α) ^{16}O reaction. This measurement yields the total number of oxygen atoms in the surface layer, based on a reference standard [11]. Equivalent thicknesses of oxides were calculated assuming a stochiometric bulk composition of Al_2O_3 (2.34×10^{22} molecular units of Al_2O_3/cm^3). Thicknesses of hydrate films that are greater than ~200 Å were measured using RBS. The surface and the cross sectional morphology of the samples were examined using a cross-sectional transmission electron microscope (X-TEM), scanning electron (SEM) and optical microscopy (OP).

11.2a Oxidation in air at room temperature

All the 6 sample types grow a native Al_2O_3 film of thicknesses ranging from 20 to 60 Å after deposition, depending on the amount of time that the samples were exposed to air. The different composition of the samples has no effect on the final thickness of Al_2O_3 that grew after few months of air exposure. It has been reported [12, 13] that Al_2O_3 initially grows very fast on Al at room temperature; however, after about 30 Å of growth, no further significant growth is observed. Such a layer has been called a barrier oxide and is known to be amorphous. The halt of the growth after the almost instantaneous growth is attributed to a very slow diffusion of either Al or oxygen atoms through the thin oxide layer. We show in Fig. 11.1 typical resonance RBS spectra for the oxide that grew on the Al film and also on the most Au-rich film

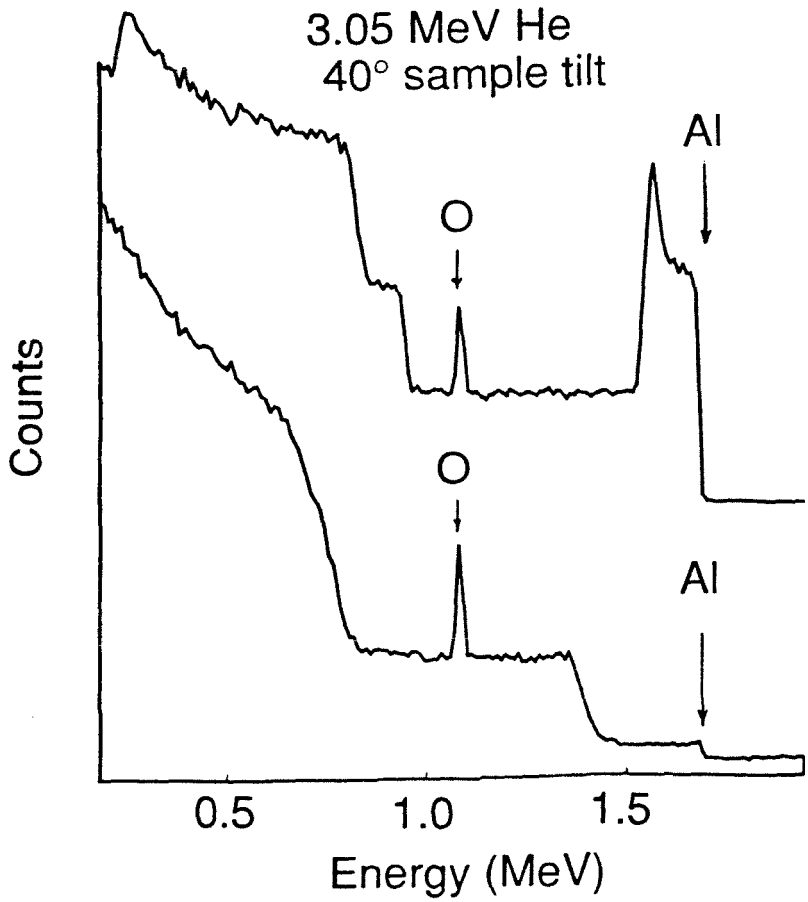

Fig. 11.1. 3.05 MeV He^{++} resonance scattering spectra showing the O content in native oxide layers that grew on Al (top Fig.) and Au_4Al (bottom Fig.) films after one month of exposure to air. The amount of oxygen is similar in both cases.

(Au_4Al phase) after 1 month of air exposure. The thickness of Al_2O_3 on Al is about 60 Å and that on Au_4Al is about 50 Å. The experimental uncertainty is +/- 30 %. From the thermodynamics calculations, the free energy of formation of Al_2O_3 on all the samples at room temperature have strong negative free energy, thus the growth of Al_2O_3 film is strongly favored on all the samples.

11..2b Oxidation in water at 100, 70, and 50° C.

When the samples were dipped into 100° C water, they all grew aluminum hydrate of the composition $Al_2O_3 \cdot H_2O$, as checked by RBS and X-ray diffraction methods. It has been also reported [14] that in water at 80~100° C, Al oxidizes into α-boehmite, $Al_2O_3 \cdot H_2O$, and at temperatures below 80° C Al oxidizes into β-bayerite, $Al_2O_3 \cdot 3H_2O$. In agreement with ref. 14, we found that $Al_2O_3 \cdot 3H_2O$ grew on all six sample types when they were dipped in 70 and 50° C water. The results are shown in Figs. 11.2 a,b, and c.

For the 100 and 70° C water oxidation, the oxides grow very quickly in the first ~10 minutes. After that, the oxide thicknesses saturate to almost constant values that are specific to each sample type. This saturation is not due to the depletion of Al in the film since there is still Al left in each sample after the hydrate stops growing. In Fig. 11.2a we indicate on the right ordinate the thickness of Al that is needed to form a certain thickness of $Al_2O_3 \cdot H_2O$ which is represented on the left ordinate. Inside the parentheses next to each final thickness of $Al_2O_3 \cdot H_2O$ for each sample types, we give the original equivalent thickness of Al available in each sample before the oxidation. By comparing these two Al thicknesses, we see that Al is still available for further oxidation in all cases. Among the possible explanations why Al hydrate stops growing, two of the most likely reasons are as follows: a) the barrier oxide, Al_2O_3,

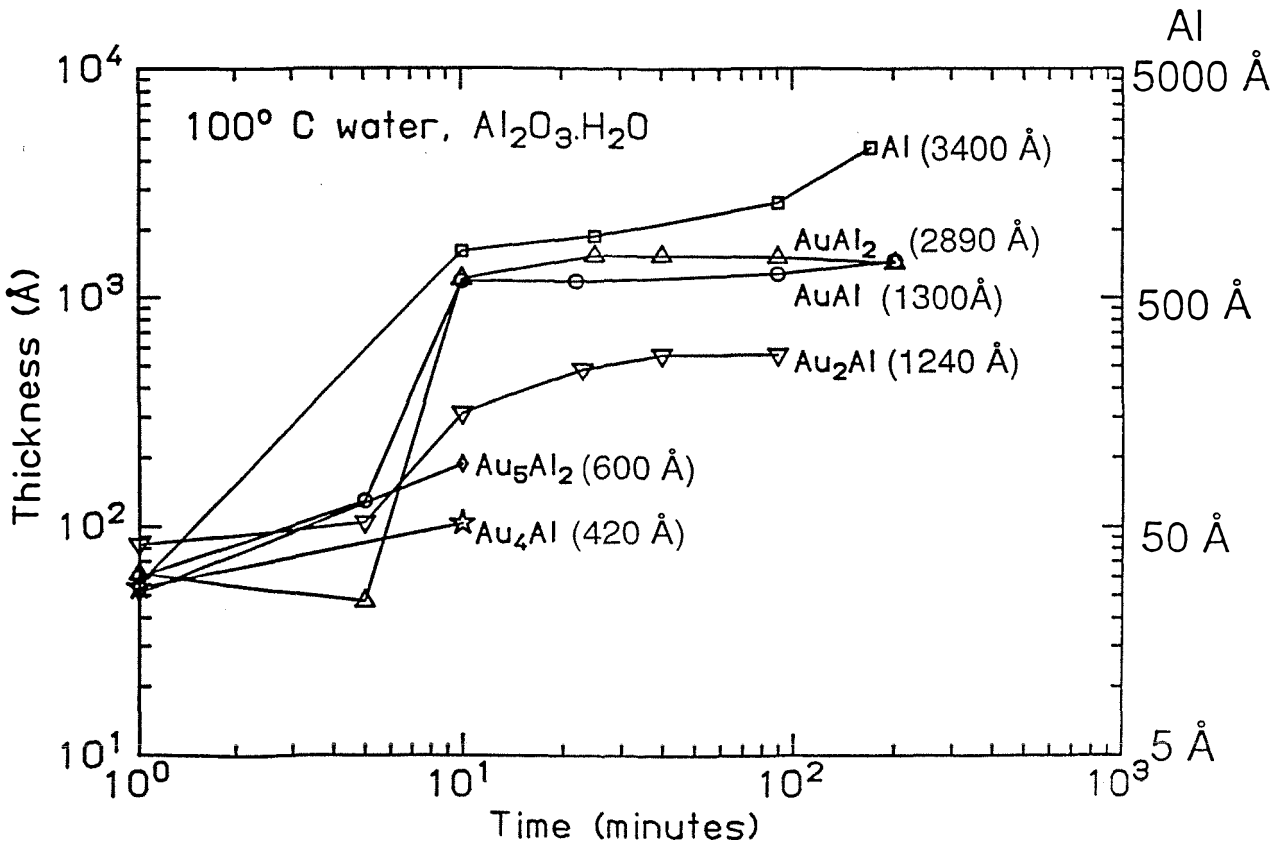

Fig. 11.2a. Thicknesses of $Al_2O_3 \cdot H_2O$ that grew on various Au-Al compounds in 100° C water versus oxidation time. The right hand scale gives the thickness of a pure Al film that contains the same amount of Al as the oxide on the left hand scale. The Al thickness in parenthesis relates similarly to the initial amount of Al contained in each sample type. Thicknesses at time 0 minute are that of native Al_2O_3 that was present on various Au-Al compounds prior to the water oxidation.

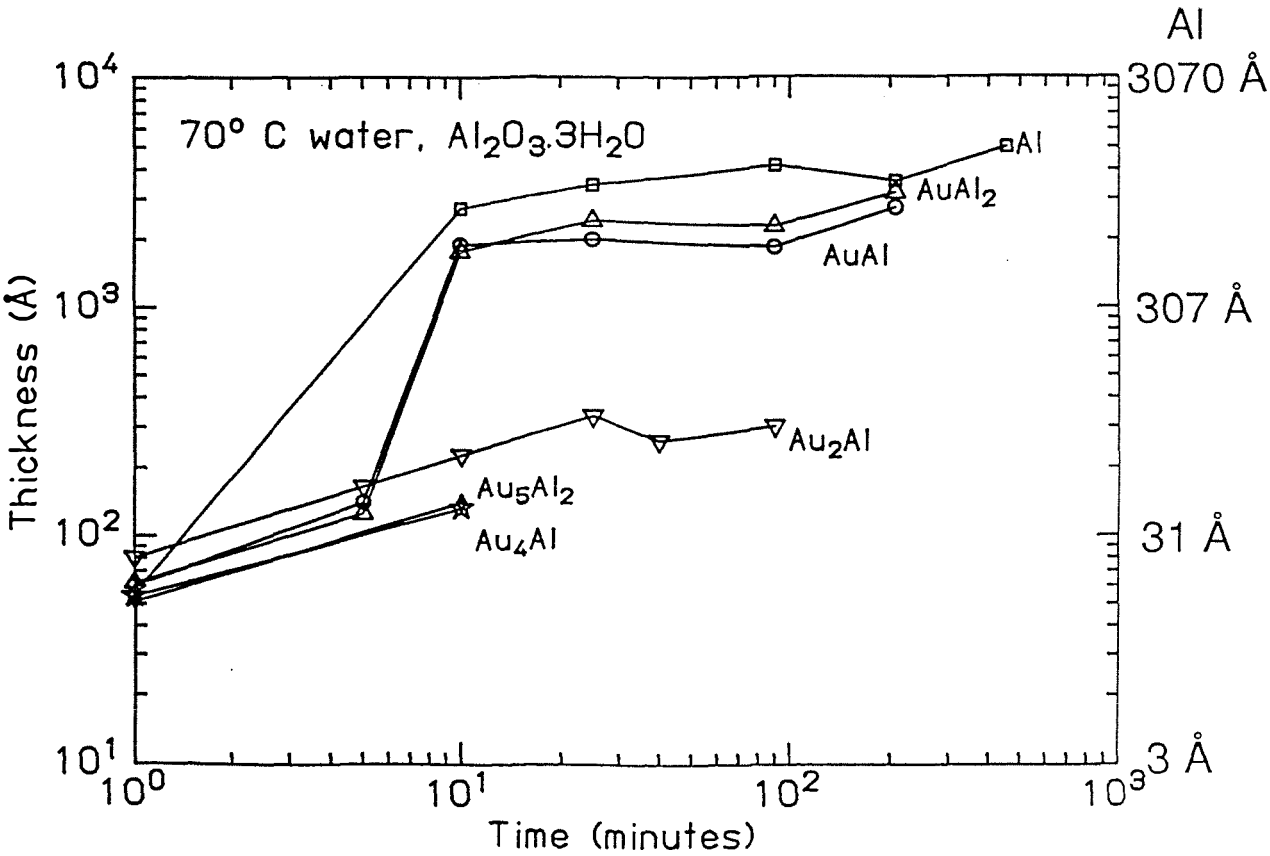

Fig. 11.2b. Thicknesses of $Al_2O_3 \cdot 3H_2O$ that grew on various Au-Al compounds in 70° C water versus oxidation time. The right hand scale gives the thickness of a pure Al film that contains the same amount of Al as the oxide on the left hand scale. Thicknesses at time 0 minute are that of native Al_2O_3 that was present on various Au-Al compounds prior to the water oxidation.

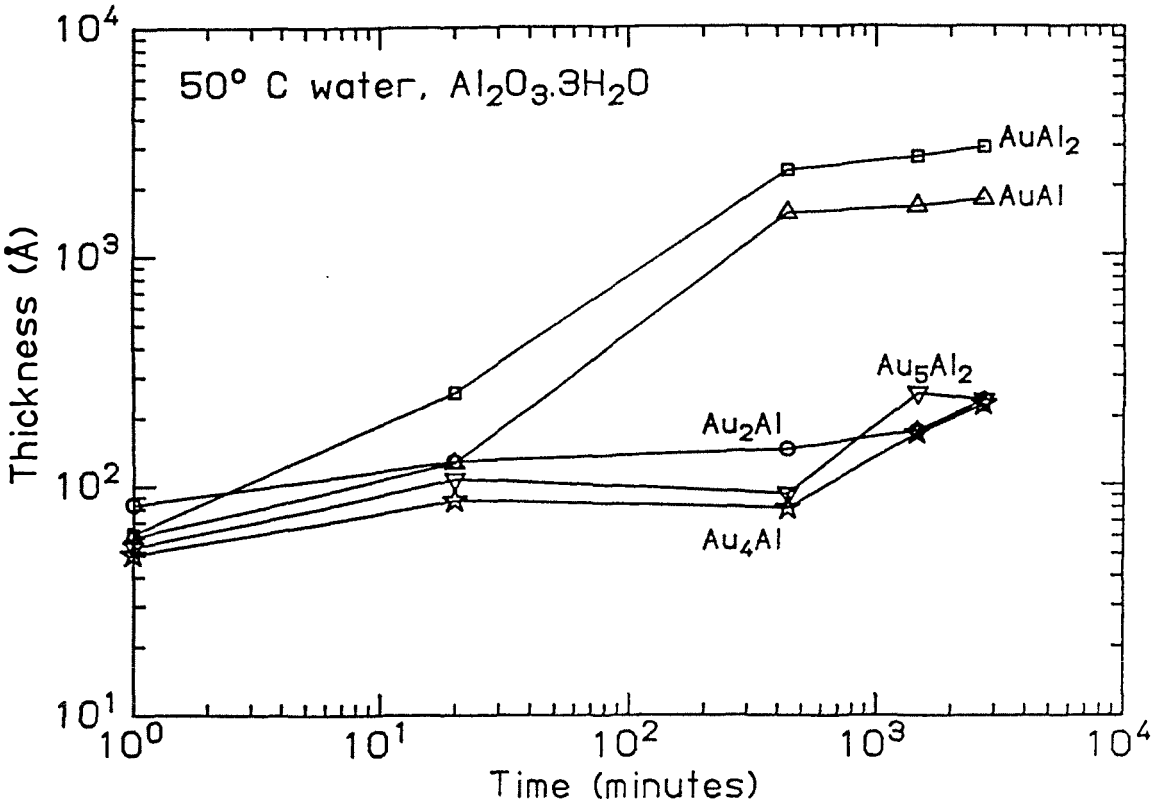

Fig. 11.2c. Thicknesses of $Al_2O_3 \cdot 3H_2O$ that have been grown on various Au-Al compounds in 50° C water versus oxidation time. Thicknesses at time 0 minute are that of native Al_2O_3 that was present on various Au-Al compounds prior to the water oxidation.

could be simultaneously growing with hydrate and after a certain barrier oxide thickness is reached, hinders the Al diffusion through oxide for further hydrate growth; and b) Au-Al compound became so Au-rich after a certain oxidation period that further withdrawal of Al from Au-Al alloy is thermodynamically and kinetically difficult. To further support these possibilities we should investigate the cross-sectional structure of the films after oxidation or investigate thermodynamics and kinetics of hydrate formation. We have done some of such a study and the results are discussed in the later paragraphs.

We notice from Figs. 11.2a and b that the aluminum hydrate layers that grow on a given sample type for a given duration are thicker for 70° C than 100° C water oxidation. However, when we compare the amount of Al incorporated in the hydrates grown on a given sample for a given period of time for 100 and 70° C water, we observe that almost the same amount of Al has been consumed. The difference is due to the different amounts of H_2O incorporated in hydrates grown at 70° C (3 H_2O molecules for 1 molecule of Al_2O_3) and 100° C (1 H_2O molecules for 1 molecule of Al_2O_3).

For 50° C water oxidation, the Al hydrate thickness is much thinner than the Al hydrate grown at 70° C and the growth rate is sluggish. We have also oxidized the samples at 40° C, but no detectable growth of Al hydrate was observed for all sample types.

We also notice in Figs. 11.2 a, b, and c that the thicknesses of Al hydrates that have grown for a given period of water oxidation time are thicker for the Au-Al compounds with larger Al content ratio. Such a phenomenon could be explained from the thermodynamics point of view. We have calculated the heats of formation, ΔH, for the water oxidation at temperatures between 278 to 373 K and similar calculations were conducted also for dry and wet O_2 conditions cases, which will be discussed in the next section.

Some of the likely reactions that we have studied are:

$$a_1Au_xAl_y+a_2H_2O\ (l)\Leftrightarrow a_3Al_2O_3{\cdot}H_2O+a_4Au+a_5H_2, \quad (1)$$

$$b_1Au_xAl_y+b_2H_2O\ (l)\Leftrightarrow b_3Al_2O_3{\cdot}3H_2O+b_4Au+b_5H_2, \quad (2)$$

$$c_1Au_xAl_y+c_2H_2O\ (g)\Leftrightarrow c_3Al_2O_3+c_4Au+c_5H_2, \quad (3)$$

$$d_1Au_xAl_y+d_2H_2O\ (g)\Leftrightarrow d_3Al_2O_3+d_4Au_2O_3+d_5H_2, \quad (4)$$

$$e_1Au_xAl_y+e_2O_2\ (g)\Leftrightarrow e_3Al_2O_3+e_4Au, \quad (5)$$

$$f_1Au_xAl_y+f_2O_2\ (g)\Leftrightarrow f_3Al_2O_3+f_4Au_2O_3, \quad (6)$$

where x and y run over all the stable Au-Al compounds [11], i.e., (x, y) = { (1, 0), (4, 1), (5, 2), (2, 1), (1, 1), (1, 2), (0, 1) }, and a_i, b_i, c_i, d_i, e_i, and f_i are the constant coefficients used to balance the reactant and product species in each of the above equations. Equations 1 and 2 stand for oxidation in water as (l) next to H_2O stands for liquid, equations 3 and 4 describe wet oxidation as (g) stands for steam, and equations 5 and 6 represent dry oxidation. The thermodynamic parameters necessary for the calculations were obtained from various references [16, 17].

We show an example of one of the above calculations by representing some of the results graphically in Fig. 11.3. The figure represents the results for the 100° C water oxidation of equation 1. In that figure, the x-axis represents the sample types in terms of the initial Al content atomic percentage (i.e.,= 100y/(x+y) with x, y from eqs. (1) to (6)), the y-axis represents the duration of water oxidation, and z-axis represents the thickness of $Al_2O_3.H_2O$ that is formed on each samples. The heat of formation for the reaction, ΔH, is shown on the right upper corner of the figure for each reaction with varying (x, y) parameters in equation 1.

The figure shows that the amount of Al hydrate that has grown after a prolonged oxidation is proportional to the magnitude of the heat of reaction. The more

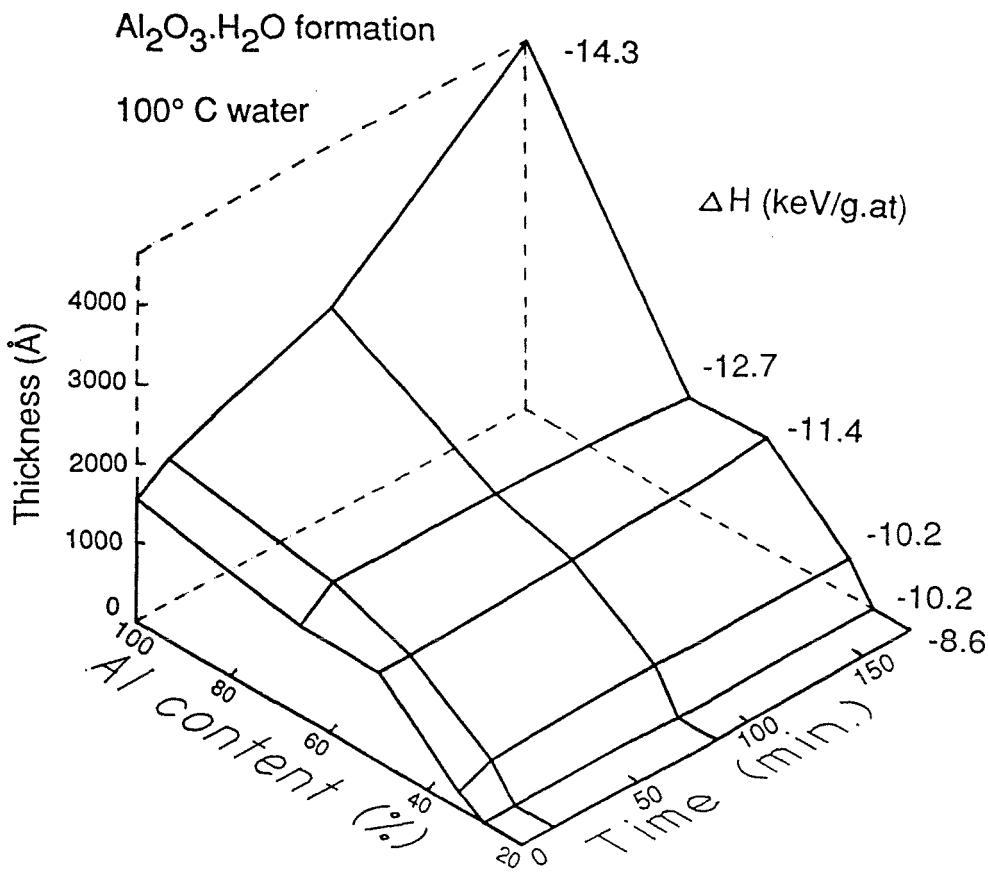

Fig. 11.3. 3-dimensional plot representing $Al_2O_3 \cdot H_2O$ formation on 6 Au-Al compounds in 100° C water for various amounts of oxidation time. The enthalpy of the sum of formation of $Al_2O_3 \cdot H_2O$, Au, and H_2 from each of these compounds have been calculated and are indicated on the upper right corner of the Fig..

negative the heat of reaction is, the thicker the Al hydrates grows. Similar trends are also observed for the reaction equations 2 through 6. Thus, the present experimental results can be explained partly by a thermodynamic argument. For a complete explanation the diffusion data for these reactions must be known. Too little is known about them to attempt such a discussion.

As the Au-Al films are oxidized, the Al content in the film decreases and the films become Au-rich. We have observed that phenomenon in the RBS, X-TEM, and X-ray diffraction data. In Figs. 11.4 a, b, and c, we show the RBS spectra for an AuAl sample that has been oxidized in water at 100, 70, and 50° C respectively for various durations of oxidation time as represented in the depth axis of the figure. In all these figures Al and O signals' widths widen as the oxidation time increases, and the Au signal becomes narrows and heightens at the same time. We also observe that the Au signal shifts backward as the oxidation time increases. All these observations indicate that the Al atoms which are depleted from AuAl compound are converted to form Al hydrates on the surface. Similar occurrences in RBS spectra have been noted for all other samples at all water temperatures.

One distinctive feature in the RBS spectra from all the others is noted in the spectrum of an AuAl sample that has been oxidized in 100° C water, which is shown in Fig. 11.4a. In that figure we observe two Au signal peaks after 10 minutes of oxidation. From the calculation, the first peak from the front of the spectrum represents the Au signal from the compound of composition ~2Au:Al and the second peak is the Au signal from the compound of composition ~Au:Al. It seems that there has been phase segregation in that sample, where the layer which is close to the outer surface is converted to an Au-rich phase. To verify such an observation, we have taken X-TEM pictures of the AuAl sample oxidized at 100° C water, and also that of the same sample that has been oxidized at 70° C water for comparison. The pictures are shown in Figs.

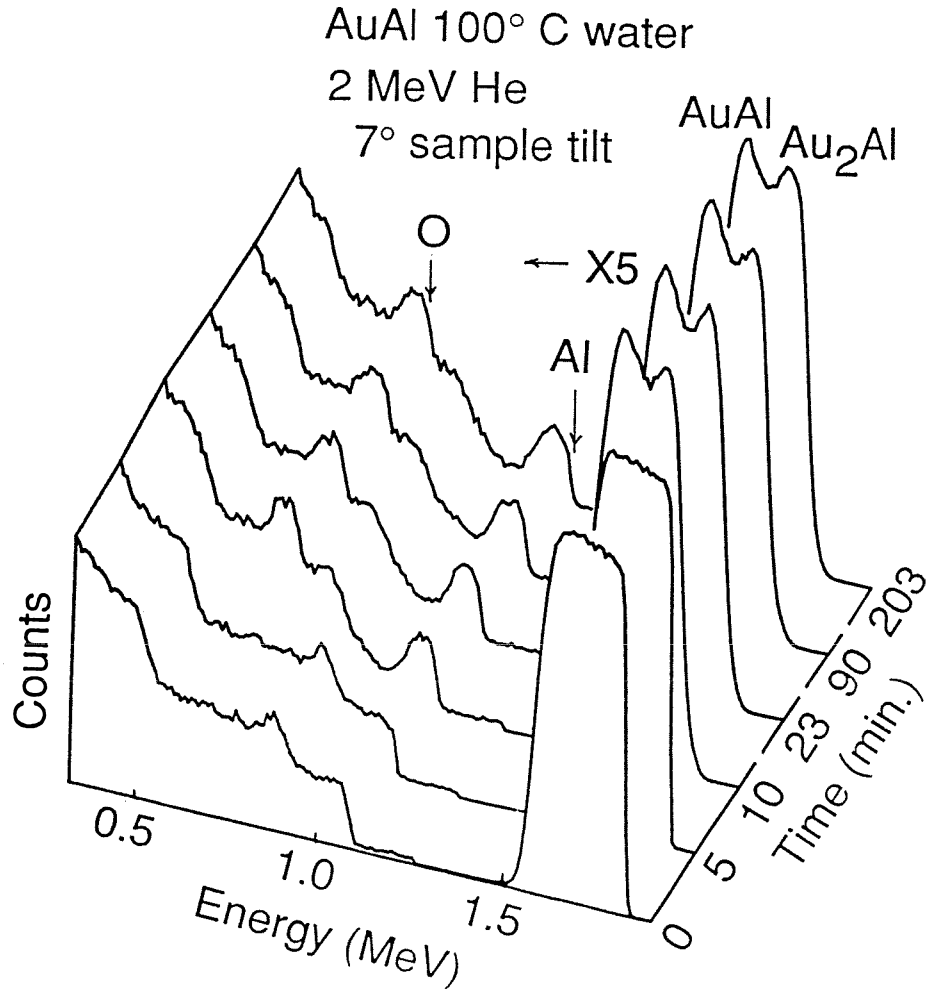
AuAl 100° C water
2 MeV He
7° sample tilt
AuAl
Au2Al
O
X5
Al
Counts
0.5
1.0
1.5
Energy (MeV)
0
5
10
23
90
203
Time (min.)

(a)

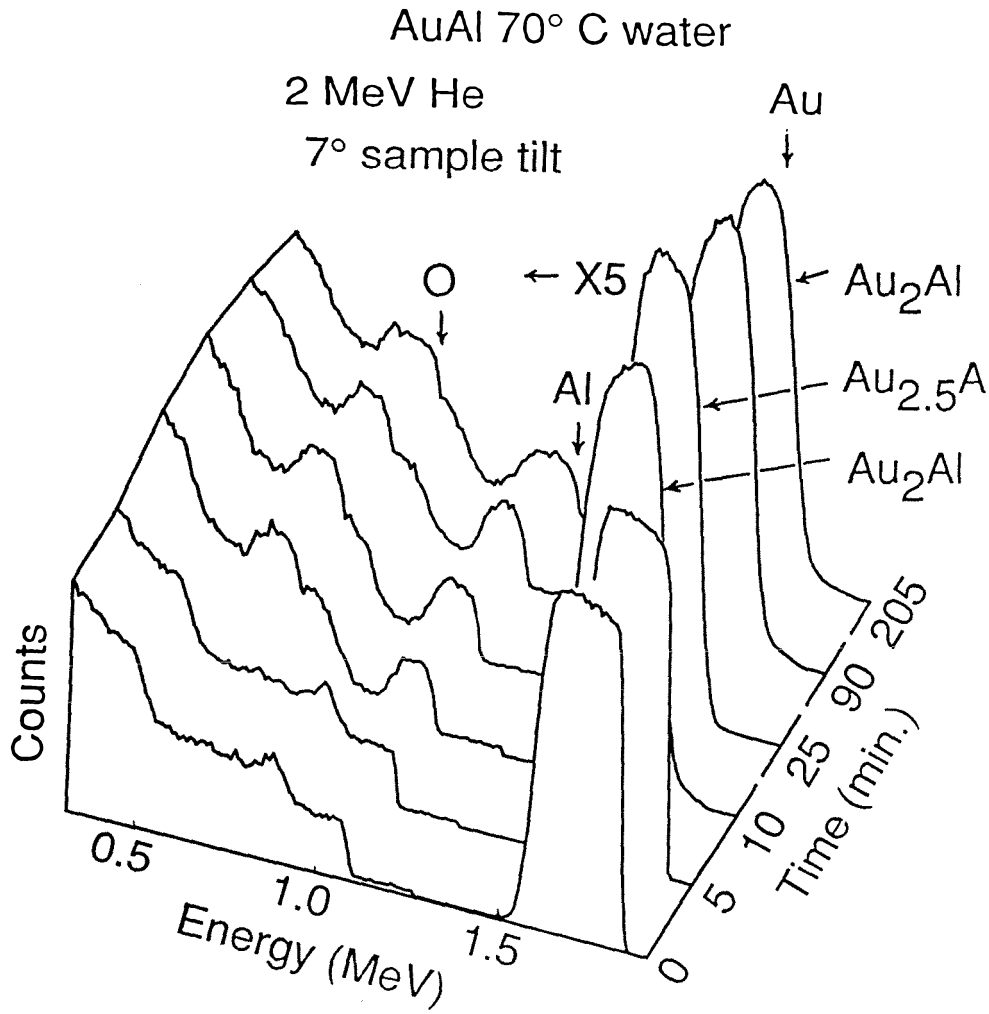
AuAl 70° C water
2 MeV He
7° sample tilt
Au
O
← X5
Au2Al
Al
Au2.5Al
Au2Al
Counts
0.5
1.0
1.5
Energy (MeV)
0
5
10
25
90
205
Time (min.)

(b)

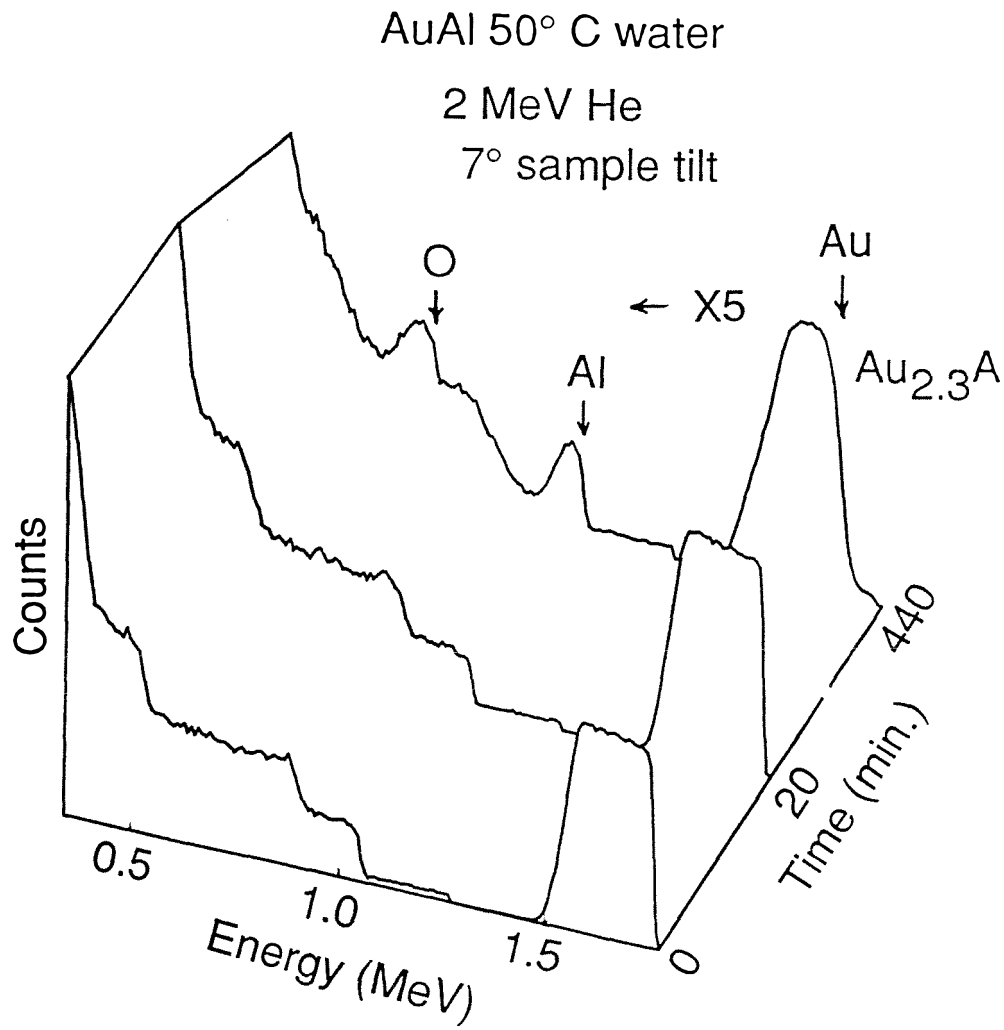

(c)

Fig. 11.4. Backscattering spectra representing; a) AuAl oxidized in 100° C water, b) AuAl oxidized in 70° C water, and c) AuAl oxidized in 50° C water.

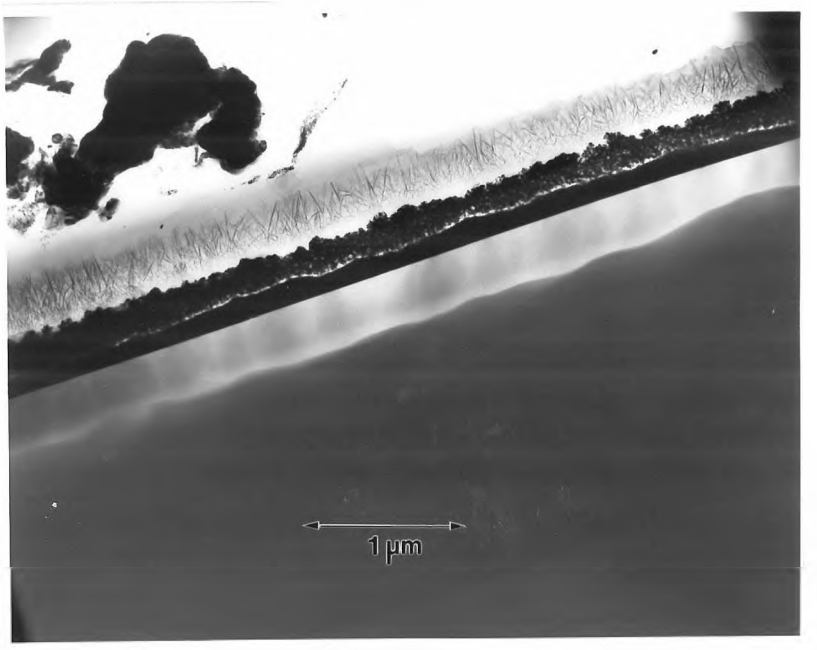

(a)

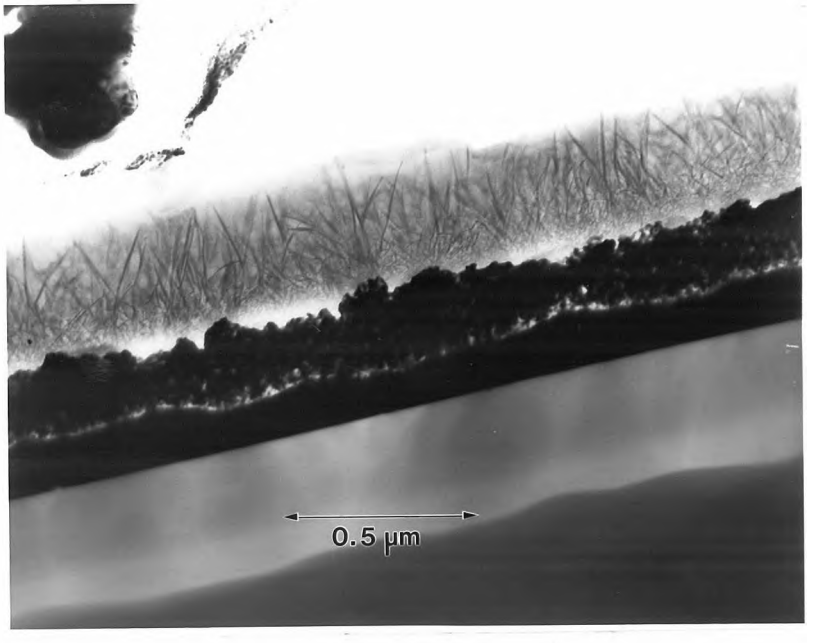

(b)

(c)

Figs. 11.5a,b,c. Cross-sectional TEM of AuAl film oxidized in 100° C water for 23 minutes. In Figs. 11.5a and b, an interface with voids can be seen between two Au-Al intermetallics as a result of Al oxidation. From the magnification of Figs. 11.5a, a fibrous growth of $Al_2O_3 \cdot H_2O$ on top of Au-Aluminides is seen in Fig. 11.5b. Further magnification of Fig. 11.5b reveals the porous structure of Au-rich Au-Al compound that is formed next to the growing $Al_2O_3 \cdot H_2O$ layer.

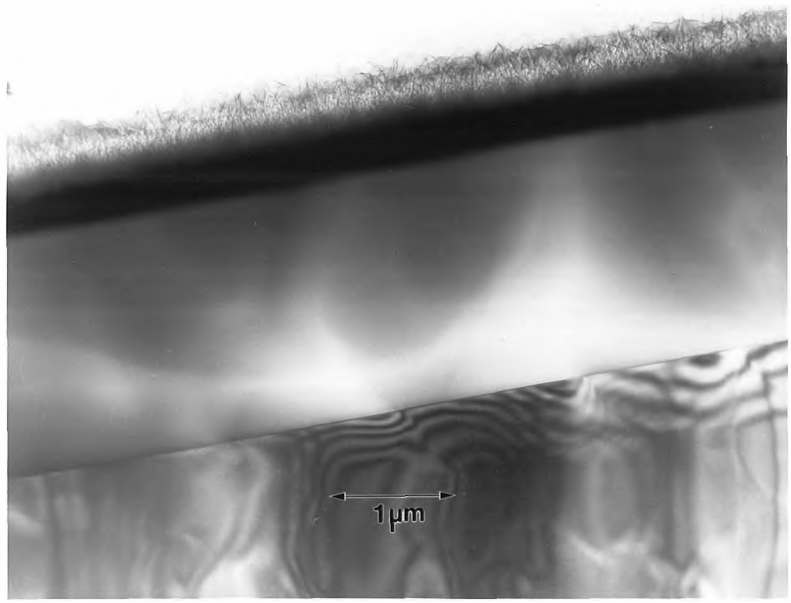

(d)

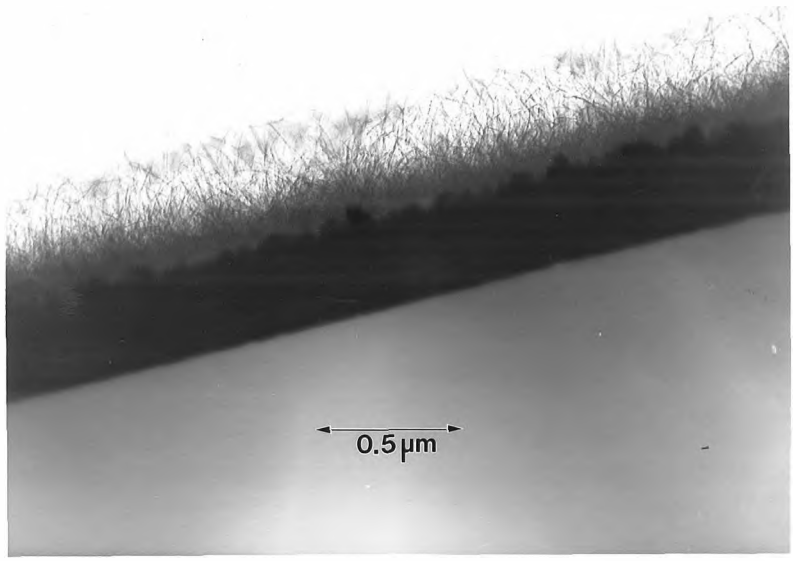

(e)

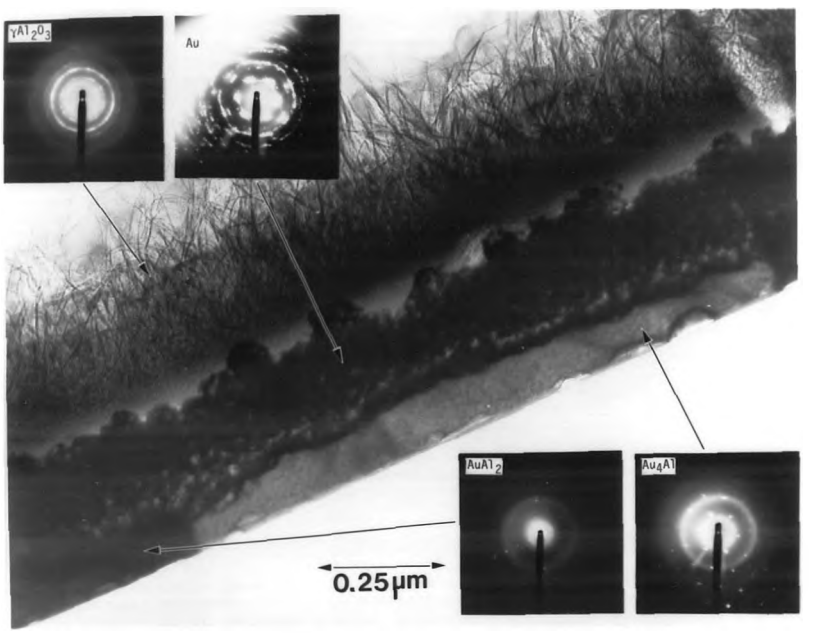

(f)

Figs. 11.5d,e,f. Cross-sectional TEM of AuAl film oxidized in 70° C water for 23 minutes. In Figs. 11.5d and e, the interface with voids that has been observed when the film is oxidized in 100° C water is absent. The morphology of the Al hydrate grown on the film as illustrated in these micrographs looks different from that of 100° C water oxidation. The lower portion of the hydrate is not fibrous, rather it is smooth and uniform compared to the Al hydrate from Figs. 11.5a and b. Fig. 11.5f shows a magnified view of Fig. 11.5e with some selected area diffractions. Many different kinds of intermetallics are co-present in the film.

11.5a,b,c,d,e, and f. From Figs. 11.5a and b we see a sharp interface inside of the Au-Al compound. The two layers seem to have different textures and there seems to be a conglomeration of voids in the interface thus almost forming a crack between the two layers.

The formation of such an interface is also observed when Au is thermally reacted with Al. During thermal reaction, all the phases simultaneously grow [3]. As the compounds are formed, voids formation also takes place along the boundaries of different phases. Such formation is believed to be due to the different kinetics between Au and Al atoms during compound formation as described in section 11.1. These voids eventually form an almost continuous line which is the cause of the crack in the Au-Al bond in the integrated circuit metallization. These high concentrations of voids form at temperatures near 400° C [3] during thermal treatment. However, we observe such voids in the Au-Al compound when it is oxidized in water at only 100° C. Thus, it seems that the rapid Al diffusion rate, which is known to cause the pile up of vacancies or voids during the formation of Au-Al phases, could have been enhanced by the water oxidation. In Figs. 11.5d and e, where they show the pictures of the AuAl samples that were oxidized at 70° C water, we do not observe such sharp interface.

In Fig. 11.5f, selected area diffraction pictures were taken for various cross-sectional regions of the film. We see that various Au-Al phases are co-formed during oxidation. The Au-rich phases are near the oxide interface and on the bottom of the film. Thus, the removal of Al to form Al hydrate would become kinetically difficult as the top layer of the compound becomes Au-rich phase. This kinetic barrier could have been the cause for the saturation of Al hydrates growth that we have observed in this experiment.

From the Figs. 11.5e and f, we observe that the texture of the hydrate is not uniform. The outer layer looks fibrous and the inner layer, which is next to the Au-Al compound, is thin and smooth. It has been noted before [15] that when Al is oxidized

in water, the oxidized layer has two types of layers; the outer layer which is microporous and thick, built upon a columnar structure; and the inner layer which is thin, dense and dielectrically compact. These descriptions fit the features that we have observed in our sample. Thus, the inner layer would correspond to thin barrier oxide and the outer layer would be the Al hydrate.

The changes of Au-Al phases due to oxidation were also studied with X-ray diffraction analysis. We have taken few of the samples for X-ray diffraction analysis and the results are shown in Table 11.1. The phases identified in each sample would not be the only phases that are present in the sample, but they are the phases that can be identified with this particular analysis technique. In general, many different types of Au-Al phases were simultaneously present in the samples. The water oxidation caused not only the growth of Al hydrate, but also it caused the formation of various phases in the Au-Al compound. The X-TEM picture from Fig. 11.5f shows that Au, Au_4Al, and $AuAl_2$ phases are present in the Au-Al compound layer and the X-ray diffraction analysis of the same sample reveals the presence of Au, Au_4Al, and Au_2Al, thus both analysis' results closely agree with each other. The AuAl sample type that showed the sharp interface after 100° C water oxidation shows to consist of Au, Au_4Al, and Au_2Al. It has been reported that voids are formed along the interfaces of such Au-rich phases [3, 4], and the present results confirm that. The expected compositions were also calculated from the RBS spectra and the results closely agree with the observed phases from X-ray diffraction analysis. All these evidences further support the interpretation of the experimental results that were described in the previous paragraphs.

Table 11.1. Au-Al phases as identified from X-ray diffraction technique and the compositions expected from the backscattering analysis for compounds: a) $AuAl_2$, b) AuAl, and c) Au_2 Al.

a) $AuAl_2$

Water temperature	70° C		
Oxidation time (min.)	0	25	202
Phases identified from X-ray analysis	$AuAl_2$	$AuAl_2$ Au	$AuAl_2$ Au_5Al_2, Au
Expected composition from backscattering analysis	$AuAl_2$	$AuAl_{1.7}$	$AuAl_{1.45}$
Water temperature	100° C		
Oxidation time (min.)	0	202	
Phases identified from X-ray analysis	$AuAl_2$	Au_4Al Au_5Al_2, Au	
Expected composition from backscattering analysis	$AuAl_2$	$AuAl_{1.62}$	

b) AuAl

Water temperature	70° C		
Oxidation time (min.)	0	10	202
Phases identified from X-ray analysis	AuAl	Au_4Al, Au Au_2Al	Au
Expected composition from backscattering analysis	AuAl	$AuAl_{1.56}$	$AuAl_{.356}$
Water temperature	100° C		
Oxidation time (min.)	0	10	202
Phases identified from X-ray analysis	AuAl	Au_4Al Au_2Al, Au	Au_2Al Au
Expected composition from backscattering analysis	AuAl	$AuAl_{.56}$	$AuAl_{.44}$

c) Au_2Al

Water temperature	70° C		
Oxidation time (min.)	0	23	
Phases identified from X-ray analysis	Au_2Al	Au Au_2Al	
Expected composition from backscattering analysis	Au_2Al	$AuAl_{.4}$	
Water temperature	100° C		
Oxidation time (min.)	0	10	40
Phases identified from X-ray analysis	Au_2Al	Au_5Al_2 Au_2Al	Au_2Al, Au_5Al_2 Au_4Al
Expected composition from backscattering analysis	Au_2Al	$AuAl_{.34}$	$AuAl_{.31}$

11..2c. Oxidation in dry O_2 condition at 500° C

Only Al and $AuAl_2$ samples were oxidized, since they are the most likely ones to oxidize among all the Au-Al phases from the thermodynamics calculations that we performed for the equations 5 and 6. The temperature chosen for the oxidationwas 500° C. We wanted the oxide to grow at a temperature where it forms with high kinetic rate but below the lowest eutectic temperature in Au-Al phases, which is 525° C. The results are shown in Fig. 11.6. Initially, the oxides grow quickly in both samples; however, further growth after a 1 hour oxidation period is very slow. Especially, the growth is very slow for $AuAl_2$. These observations agree well with the previous results [12] where it was observed that the initial oxide growth was rapid, but the growth slowed down in the later stage of oxidation. It is believed that [12] the rapid initial growth results in the formation of a thin amorphous barrier oxide and the slow growth rate results in the formation of a porous crystalline oxide over the barrier oxide.

11..2d Summary

1. On all the Au-Al compounds that were exposed to air at room temperature, a layer of Al_2O_3 film with a thickness of less than 60 Å grows. The thickness of Al_2O_3 that grows on these samples was independent of Au-Al composition of the sample.
2. Al hydrates grow on all the Au-Al compound types when the samples are dipped in 50, 70, and 100° C water. Au-Al compounds that were water oxidized at 50 and 70° C form $Al_2O_3 \cdot 3H_2O$ and those oxidized at 100° C form $Al_2O_3 \cdot H_2O$.
3. The different amounts of Al hydrate growth for different types of Au-Al phases can partly be explained with the thermodynamic argument. The growth of Al hydrates saturates to certain thickness after prolonged water oxidation.

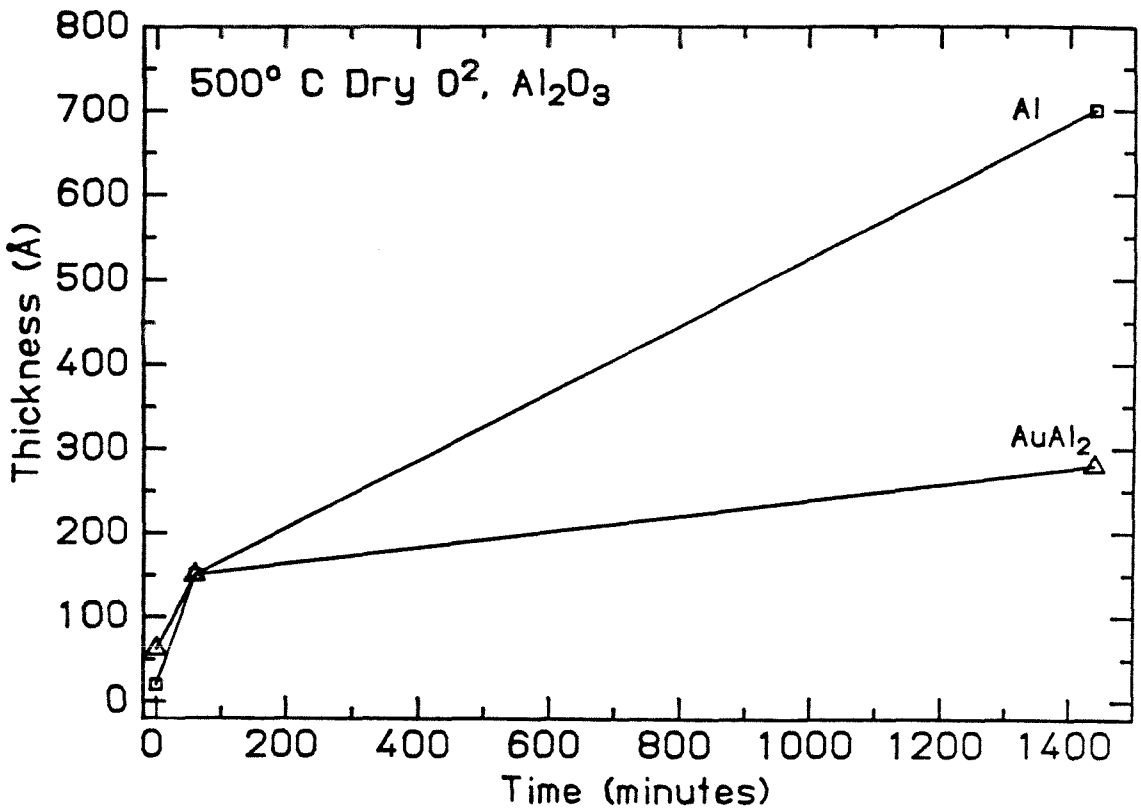

Fig. 11.6. Growth of Al_2O_3 on $AuAl_2$ and Al films under dry O_2 flow condition at 500° C.

4. As the Al hydrates grow during water oxidation, many Au-Al phases are formed simultaneously in the film.

5. Interfaces are formed between different layers of intermetallics when AuAl is oxidized in 100° C.

6. At 500° C dry oxidation, a few hundreds of Å's of Al_2O_3 grow on Al and $AuAl_2$ samples.

11.3 References

[1] G. Majni, C. Nobili, G. Ottaviani, M. Costato, and E. Galli, J. Appl. Phys., 52 (1981) 4047.

[2] S.U. Campisano, G. Foti, E. Rimini, S.S. Lau, and J.W. Mayer, Phil. Mag., 31 (1975) 903.

[3] E. Philofsky, Solid St. Electron., 13 (1970) 1391.

[4] G.V. Clatterbaugh, J.A. Weiner, and H.J. Charles, Jr., IEEE 0569-5503 (1984) 21.

[5] J.M. Vandenberg and R.A. Hamm, J. Vac. Sci. Technol., 19 (1981) 84.

[6] VLSI Technology, Ed. S.M. Sze, (McGraw-Hill, New York, 1983) p. 380.

[7] D.Y. Shih and P.J. Ficalora, IEEE/Proc. IRPS CH1619-6 (1981) 253.

[8] H.K. Charles, Jr., B.M. Romenesko, G.D. Wagner, R.C. Benson, and O.M. Uy, IEEE/Proc. IRPS (1982) 136.

[9] R.J. Gale, IEEE/Proc. IRPS CH1990-1 (1984) 37.

[10] Semiconductor International, 18 (1987).

[11] X.-A. Zhao, T.C. Banwell, and M-A. Nicolet, SPIE 623 (1986) 255.

[12] P.E. Blackburn and E.A. Gulbransen, J. Elechem. Soc., 107 (1960) 944.

[13] W.W. Smeltzer, J. Elechem. Soc., 103 (1956) 209.

[14] J.M. Bryan, J.S.C.I., 69 (1950) 169.

[15] M. Hansen and K. Anderko, Constitution of Binary Alloys, (McGraw-Hill, New York) p.68.

[16] I. Barin and O. Knacke, Thermodynamical Properties of Inorganic Substances, (Spinger-Verlag, Berlin, 1973 and 1977).

[17] R. Ferro, R. Capelli, and Rinaldo Marazza, Rend. Sc. Fis. Mat. e Nat. 41 (1966) 85.

Chapter 12

FINAL REMARKS OF PART II; OXIDATION OF SILICIDES AND Au-ALUMINIDES

12.1 Conclusions and future investigations on the oxidation of silicides

Each chapter in part II is self-contained with a summary at the end. All are related to oxidation phenomena. The present chapter gives overall conclusions. Further useful investigations are discussed.

Interest in the study of oxidation of silicides on SiO_2 was motivated by the need to find new ways to create low resistivity interconnections for VLSI circuits. Our goal was to determine whether the process of oxidizing a silicide layer offered such an alternative. The two main issues we have addressed are physical stability and electrical resistivity of the film after oxidation. We find that during the oxidation process the metal-rich film is morphologically unstable on SiO_2, which is due to the surface tension. To be useful as a low-resistivity interconnection line, the residual atomic concentration of Si in the metallic film after oxidation must be below 10 at.%, which is quite a stringent condition for this oxidation condition. The conclusion we arrive at is that the oxidation of silicides is not as simple a way to produce low-resistivity interconnection lines as appeared initially. The problem is to extract as much Si as possible from the metal-rich film without activating the morphological stability of the film at the same time.

In future investigations, one should look for improved ways to implement the oxidation. For example, the morphological stability of the film might improve if the atomic rearrangements during oxidation are reduced, for instance by starting with an already metal-rich silicide. The metal oxides could possibly form together with the

SiO_2 under such circumstances, depending on the thermodynamic conditions. If the co-growth of metal oxides is unavoidable, then the properties and the effects of such oxides on the morphology and dielectric properties of the protective coating will need to be investigated as well.

The morphological instability could also be improved conceptually by reducing the surface tension of the metal on SiO_2. For instance, the surface of the SiO_2 substrate could be modified to reduce the surface diffusion of the metal atoms, or atomic components could be added to the silicide prior to oxidation that would enhance the wetting of metal to SiO_2. Ti or Cr, for example, are known to wet SiO_2 very well.

It would be also worthwhile also to look into other silicides which might achieve the goal. The refractory metals, especially, have less surface tension on SiO_2 than Co and Ni, and almost all metal silicides oxidize by forming SiO_2 layers. Rapid thermal annealing may offer yet another approach worth a try, because the processes of alteration of the atomic compositions and the morphology of the film probably have different activation energies.

12.2 Conclusions and future investigations on the oxidation of Au-Aluminides

The failure of the Au-Al bond is a serious problem in the integrated circuit. As the operating temperature of devices rises, the Au-Al junction temperature also increases. The rise of temperature, accompanied by the outgassing of encapsulating plastics that surround the integrated circuit, enhances the formation of intermetallics in the Au-Al bond.

We found that water greatly enhances the chemical reactions in a Au-Al layer: thick Al hydrates grow on the film, many Au-Al intermetallics are formed, and the voids appear in the compound. All of these effects are detrimental to the electrical and

physical state of the bond. All these problems need to be corrected, and especially the formation of voids.

The formation of voids is a common phenomenon. Void swelling is observed in the material that covers the nuclear reactor wall. It is caused by the pile up of point defects that are created by the irradiative environment. There are very many investigations of this particular problem which is, in fact, a part of the field of "radiation-enhanced diffusion", which we also consider in chapters 6 and 7 of this thesis. One remedy for void swelling induced by irradiation is the addition of very small (<< 1 at. %) amounts of a solute atom. The solute atoms interact with the irradiation-induced defects and reduce the swelling. One could similarly add certain types of solutes to the Au-Al compound in the hope of eliminating the pile up of vacancies in the Au-Al bond, thus eliminating the weakening of bonds caused by high temperature and oxidation. The formation of voids could also be avoided by preventing the formation of Au-Al intermetallics. A diffusion barrier inserted in the Au-Al bond might be one way to accomplish this. Yet another possibility is to prevent the oxidation of Al. The most obvious way is to eliminate the source of the oxidants or, in other words, to use a packaging material that outgasses very little. One could also coat the Au-Al bond with a suitable protective layer.

List of publications and presentations

I. Ion-Solid Interactions.

1. S.-J. Kim, M-A. Nicolet, R.S. Averback, and P. Baldo, *Low-Temperature Ion Beam Mixing of Pt and Si Markers in Ge.* Appl. Phys. Lett. 46 (1985) 154.

2. S.-J. Kim, B.M. Paine, M-A. Nicolet, R.S. Averback, and D. Peak, *Ion Beam Mixing at Low Temperatures Studied with Marker Atoms Using 300-1000 keV Kr ions.* Presented and published in the proc. of second workshop of Ion Beam Mixing and Surface Layer Alloying, 1985.

3. S.-J. Kim, B.M. Paine, M-A. Nicolet, and R.S. Averback, *Ion Beam Mixing of Marker Atoms in Mo and Ru and Heat of Mixing.* Presented and published in the proc. of MRS Fall meeting, Vol. 54 (1985) 237.

4. S.-J. Kim, R.S. Averback, and M-A. Nicolet, *Ion Mixing and Thermochemical Properties of Markers in Cu.* Appl. Phys. A41 (1986) 171.

5. S.-J. Kim, R.S. Averback, and M-A. Nicolet, *Low Temperature Ion Mixing and Thermochemical Properties of Markers in Cu.* Presented at 19 th AVS meeting, 1986.

6. S.-J. Kim, R.S. Averback, and M-A. Nicolet, *Influence of Thermochemical Properties on Ion Mixing of Markers in Cu and B-Zr at 77 K with Kr.* Presented and published in the proc. of IBMM '86, Catania, Italy, Nucl. Instr. & Meth. B19/20 (1987) 662.

7. S.-J. Kim, M-A. Nicolet, R.S. Averback, and D. Peak, *Low-Temperature Ion Beam Mixing in Metals.* Phys. Rev. B 138 (1988) 38.

8. S.-J. Kim, M-A. Nicolet, and R.S. Averback, *Temperature Dependence on Ion Mixing of Markers in Zr.* Presented and published in the proc. of MRS Fall meeting, Vol. 74 (1987) 437.

9. S.-J. Kim, D.N. Jamieson, R.S. Averback, and M-A. Nicolet, *The Influence of Dose Rate and Temperature on The Formation of $CrSi_2$ by Ion Mixing*. Presented and published in the proc. of MRS Spring meeting, Vol. 93 (1987) 233.

10. R.S. Averback, S.-J. Kim, and T. Diaz de la Rubia, *The Role of Energetic Displacement Cascades in Ion Beam Modification of Materials*. Presented and published in the proc. of MRS Fall meeting, Vol. 74 (1987) 399.

11. E. Ma, S.-J. Kim, R.S. Averback, and M-A. Nicolet, *Ion Mixing and Thermochemical Properties of Markers in Ag*. Presented in the MRS Spring meeting, Anaheim 1987. Published in J. Appl. Phys. 63 (1988) 2449.

II. Oxidation and Thin Film Reactions.

1. S.-J. Kim, T.C. Banwell, and M-A. Nicolet, *Irradiation Effects on Oxidation of $CoSi_2$ Interconnects on SiO_2 Substrates*. Presented at IBMM '84 meeting, Ithaca.

2. S.-J. Kim, T.C. Banwell, R. Shima, and M-A. Nicolet, *Experimental Investigation on The Oxidation of Cobalt Silicide ($CoSi_2$)*. Presented and published in the proc. of SPIE '85 meeting, Vol. 530 (1985) 152.

3. S.-J. Kim, Y.-T. Cheng, and M-A. Nicolet, *Effect of Added Si on the Resistivity of Co and Ni Films*. Presented and published in the proc. of SPIE '86 meeting, Vol. 623 (1986) 261.

4. S.-J. Kim and M-A. Nicolet, *Oxidation of Au-Al Alloys in Water*. Presented at ICMC '87. To be published.

5. S.-J. Kim and M-A. Nicolet, *Transition Metal Silicides for Microelectronics*. To be presented and published in the proc. of ASM International World Materials Congress, Chicago 1988.